Widefield Computational Biophotonic Imaging for Spatiotemporal Cardiovascular Hemodynamic Monitoring

by

Robert Amelard

A thesis
presented to the University of Waterloo
in fulfillment of the
thesis requirement for the degree of
Doctor of Philosophy
in
Systems Design Engineering

Waterloo, Ontario, Canada, 2017

Examining Committee Membership

The following served on the Examining Committee for this thesis. The decision of the Examining Committee is by majority vote.

External Examiner	Dr. Bernard Choi Associate Professor, Biomedical Engineering University of California, Irvine
Supervisor	Dr. Alexander Wong Associate Professor, Systems Design Engineering University of Waterloo
Supervisor	Dr. David Clausi Professor, Systems Design Engineering University of Waterloo
Internal Member	Dr. Maud Gorbet Associate Professor, Systems Design Engineering University of Waterloo
Internal Member	Dr. John Zelek Associate Professor, Systems Design Engineering University of Waterloo
Internal-external Member	Dr. Richard Hughson Professor, Kinesiology University of Waterloo

This thesis consists of material all of which I authored or co-authored: see Statement of Contributions included in the thesis. This is a true copy of the thesis, including any required final revisions, as accepted by my examiners.

I understand that my thesis may be made electronically available to the public.

Statement of Contributions

Content from 4 papers are used in this thesis. I was a co-author with major contributions on the design, development, evaluation and writing of the papers' material.

R. Amelard, D. A. Clausi, A. Wong, "A spectral-spatial fusion model for robust blood pulse waveform extraction in photoplethysmographic imaging," *Biomedical Optics Express*, vol. 7, no. 12, pp. 4874–4885, 2016.
This paper is incorporated in Chapter 4 of this thesis.

R. Amelard, D. A. Clausi, A. Wong, "Spatial probabilistic pulsatility model for enhancing photoplethysmographic imaging systems," *Journal of Biomedical Optics*, vol. 21, no. 11, pp. 116010-1-116010-7, 2016.
This paper is incorporated in Chapter 5 of this thesis.

R. Amelard, R. L. Hughson, D. K. Greaves, K. J. Pfisterer, J. Leung, D. A. Clausi, A. Wong, "Non-contact hemodynamic imaging reveals the jugular venous pulse waveform," *Scientific Reports*, vol. 6, pp. 40150, 2017.
This paper is incorporated in Chapter 5 of this thesis.

R. Amelard, R. L. Hughson, D. A. Clausi, A. Wong,"Non-contact arrhythmia assessment in natural settings: a step toward preventive cardiac care," *Proc. SPIE 10042, Diagnostic and Therapeutic Applications of Light in Cardiology*, San Francisco, Jan 2017.
This paper is incorporated in Chapter 5 of this thesis.

Abstract

Cardiovascular disease is the leading cause of mortality, resulting in 17.3 million deaths per year globally. Although cardiovascular disease accounts for approximately 30% of deaths in the United States, many deleterious events can be mitigated or prevented if detected and treated early. Indeed, early intervention and healthier behaviour adoption can reduce the relative risk of first heart attacks by up to 80% compared to those who do not adopt new healthy behaviours. Cardiovascular monitoring is a vital component of disease detection, mitigation, and treatment. The cardiovascular system is an incredibly dynamic system that constantly adapts to internal and external stimuli. Monitoring cardiovascular function and response is vital for disease detection and monitoring.

Biophotonic technologies provide unique solutions for cardiovascular assessment and monitoring in naturalistic and clinical settings. These technologies leverage the properties of light as it enters and interacts with the tissue, providing safe and rapid sensing that can be performed in many different environments. Light entering into human tissue undergoes a complex series of absorption and scattering events according to both the illumination and tissue properties. The field of quantitative biomedical optics seeks to quantify physiological processes by analysing the remitted light characteristics relative to the controlled illumination source.

Drawing inspiration from contact-based biophotonic sensing technologies such as pulse oximetry and near infrared spectroscopy, we explored the feasibility of widefield hemodynamic assessment using computational biophotonic imaging. Specifically, we investigated the hypothesis that computational biophotonic imaging can assess spatial and temporal properties of pulsatile blood flow across large tissue regions.

This thesis presents the design, development, and evaluation of a novel photoplethysmographic imaging system for assessing spatial and temporal hemodynamics in major pulsatile vasculature through the sensing and processing of subtle light intensity fluctuations arising from local changes in blood volume. This system co-integrates methods from biomedical optics, electronic control, and biomedical image and signal processing to enable non-contact widefield hemodynamic assessment over large tissue regions. A biophotonic optical model was developed to quantitatively assess transient blood volume changes in a manner that does not require *a priori* information about the tissue's absorption and scattering characteristics. A novel automatic blood pulse waveform extraction method was developed to encourage passive monitoring. This spectral-spatial pixel fusion method uses physiological hemodynamic priors to guide a probabilistic framework for learning pixel weights across the scene. Pixels are combined according to their signal weight, resulting in a single waveform.

Widefield hemodynamic imaging was assessed in three biomedical applications using the aforementioned developed system. First, spatial vascular distribution was investigated across a sample with highly varying demographics for assessing common pulsatile vascular pathways. Second, non-contact biophotonic assessment of the jugular venous pulse waveform was assessed, demonstrating clinically important information about cardiac contractility function in a manner which is currently assessed through invasive catheterization. Lastly, non-contact biophotonic assessment of cardiac arrhythmia was demonstrated, leveraging the system's ability to extract strong hemodynamic signals for assessing subtle fluctuations in the waveform. This research demonstrates that this novel approach for computational biophotonic hemodynamic imaging offers new cardiovascular monitoring and assessment techniques, which can enable new scientific discoveries and clinical detection related to cardiovascular function.

Acknowledgements

We shall not cease from exploration,
And the end of all our exploring
Will be to arrive where we started
And know the place for the first time.
–*T. S. Eliot*

It takes great mentors to navigate and support a new exploration. Thank you, Alex Wong and David Clausi, for your support for my visions, and for constructing a small empire to help build and disseminate my work. You've given me tall shoulders on which to stand, and a full toolbox to carry with me.

Building a biophotonic imaging system requires application knowledge from a handful of different fields. I'm grateful to have intelligent friends and colleagues who invested time and energy to share knowledge about electronics (Christian Scharfenberger, Gopal Valsan, Jay Shah, Adam Neale) and optics (David Priest, Farnoud Kazemzadeh, John Delaney, Cleber Ferraresi). Your help has influenced the design and development of the system presented here. Thank you.

The system is built on layers of intricately co-integrated subsystems that were developed with the help of exceptionally bright individuals, specifically hardware (Jason Leung), illumination (Mackenzie Wilson, Jordan Geurten, YanYan Tran) and imaging (Mikaela MacMahon, Mujtaba Tirmizi) subsystems. Thank you.

Building a new imaging system often meant having more ideas than time. Bill Lin and Shubh Jagani's work was instrumental in assessing new processing methods and applications for expanding the system's capabilities. I've enjoyed illuminating discussions with Tom Hunter, Gerard Shoemaker, Geoff Fournie, Connie Harris, Ron Herzog, and Doug Bean about clinically impactful applications. Thank you.

As a systems design engineering researcher, several cross-disciplinary members were pivotal in helping me understand the "system" that I was studying. Thank you Richard Hughson for training me in the world of cardiovascular physiology, which became a supporting pillar for the vision of my research efforts. Thank you Danielle Greaves for our many discussions and hours spent prodding people with ultrasound probes and sketching their vessels with Sharpies. Thank you Tom Beltrame, Laura Fitzgibbon, Ikdip Brar, and Rodrigo Villar for helping me with early stage cardiovascular assessment protocols and discussions. I appreciate the time and knowledge you invested in me, and enjoyed working together. Thank you.

As I started addressing the primary challenges, I started realization the profound impact biomedical optics and biophotonics could have on my work. A number of individuals in this wonderful community helped shape my understanding for light-tissue interaction and photon migration in human tissue. Thank you Vasan Venugopalan for supporting my curiosity in computational biophotonics. I have enjoyed our invigorating discussions about fundamental radiative transport. Thank you David Cuccia for excitedly discussing matters from light transport to commercial applications of biophotonic imaging technologies. Your work has been an inspiration for my own. Thank you Bruce Tromberg for your tremendous support in pursuing exciting collaborations together. Thank you as well to the Short Course on Computational Biophotonics speakers and attendees for providing an organized curriculum of computational biophotonics.

A large portion of the data collection could not have been performed without the support from members at the Schlegel-UW Research Institute for Aging. Thank you to all of the RIA team members for a creating a supportive and enthusiastic research environment. Thank you Josie d'Avernas, Gert Hartmann, Susan Brown, and Ron Schlegel for your support and providing me the opportunity to present my work to tour groups and visitors. Thank you also to Kate Ducak and Kaitlin Garbutt for helping with my data collection. Mike Sharratt, in addition to all of this, your unbridled excitement and hearty support for my work has inspired my big picture outlook, and has helped me reach further than I could without you. You are missed greatly.

I am fortunate to have strong mentors. Thank you George Labahn for your strong perpetual support since my earliest peaked interest in research. Thank you Ben Wagner for supporting my training in biomedical imaging and guiding me with an application-focussed vision. Thank you Cassie Smith for helping me stay balanced and grounded. Thank you to those of you that were listed above and also deserve recognition as supportive mentors.

"*If you want to know someone, get to know their friends.*" I am fortunate to be positively influenced by supportive friends, many of whom have been acknowledged in other parts here. To those that I haven't yet acknowledged, thank you Ben Selby, Armin Hasanbegovic, Cory Shankman, Eric Pisani, Nithin Kadayil, Audrey Chung, Brendan Chwyl, Glen Nyhus, Mark Schwarz, Dave Petro and Lloyd Hipel for sharing your enthusiasm and support for my work. Thank you Victor Cheung, Matt Parker, Sarah Amelard, Xander and Theo Prevatt, and Jonathan Janzen for dedicating some of your time to support my research, as well as your enthusiasm. Thank you Rini and Ritesh Bhargava for nourishing my mind and tongue. The members of the Vision and Image Processing Research Group have built an optimal mixture of intelligence, collaboration, and playfulness, yielding an exceptionally invigorating and cerebral environment. Thank you all for our conversations and interactions over the last several years.

I have been fortunate to have a supportive and lively team of committee members (Dr. Maud Gorbet, Dr. Richard Hughson, Dr. John Zelek, Dr. Bernard Choi). Thank you for your time to review my thesis and your support and insightful feedback throughout my research.

To my mom, dad and brother, thank you for wanting me to do nothing more than follow my dreams and encouraging me to travel down an unbeaten path, with spurts of fun, excitement and distractions sprinkled throughout. Thank you Ann, Steve, Lacy, Cindy, Mark and Cody for sharing your excitement about my research, and for helping me to view challenges in different lights. Thank you to my wonderful grandparents who have offered me perspectives on life by sharing parts of your adventures over different eras.

This vision was met with crucial funding support by The Natural Sciences and Engineering Research Council of Canada, AGE-WELL NCE Inc., SPIE, Mitacs, and the Canada Research Chairs program. Thank you also to the participants in my studies, without whom my work would still be very theoretical in nature.

Lastly, Kaylen, you've helped me discover new parts to my map that appeared blank. You've helped me shed light on new territories and explore a whole spectrum of new opportunities. It has been an exciting adventure with more exploration yet to be had!

To Kaylen

Table of Contents

List of Tables

List of Figures

Chapter 1

Introduction

1.1 Problem Statement

Cardiovascular disease is the leading cause of mortality, resulting in 17.3 million deaths per year globally, and approximately 30% of all deaths in the United States [1]. Cardiovascular monitoring is essential to assessing and maintaining or enhancing quality of life through proactive and acute care. Many cardiovascular diseases can be largely mitigated through early intervention. For example, a large scale case-control study concluded that adopting healthier behaviours could lead to up to 80% lower relative risk of myocardial infarction [2]. A fundamental problem is that cardiovascular disease onset may go undetected for extended lengths of time, rendering early intervention difficult. In North America's primarily acute healthcare model, diagnosis and treatment are often investigated as a result of self-identified physical symptoms such as shortness of breath or lack of energy [3, 4]. However, at this point the disease had been manifesting prior to the expression of a physical symptom. It is therefore critically important to develop and use cardiovascular monitoring technologies for early detection of cardiovascular changes to help manage patient prognosis.

There are a number of existing technologies used clinically for assessing cardiovascular status. Electrocardiography (ECG) assesses the heart's electrical function by adhering electrodes to the skin surface and detecting subtle electrical changes from cardiac depolarization and repolarization. Though it provides critical information for assessing cardiac electrical function, is not suitable for assessing vascular hemodynamics. Many subsurface cardiovascular imaging systems rely on a combination of ionizing radiation (computed tomographic angiography, x-ray angiography), contrast agent injection through vascular catheterization (computed tomographic angiography, x-ray angiography, magnetic reso-

nance angiography), or time-consuming and expensive tests (magnetic resonance angiography, computed tomographic angiography), making it difficult for proactive or repeated monitoring. Ultrasound imaging systems are unique systems capable of assessing vascular flow within an axial two-dimensional field of view, but are commonly prescribed for specific large arterial or venous assessment, and cannot easily assess large tissue hemodynamics and perfusion, which is an important marker for tissue health [5]. There is therefore a need for bedside cardiovascular monitoring technologies that are able to provide widefield cardiovascular assessment without the use of ionizing radiation or contrast agents.

Photoplethysmography (PPG) is a non-invasive biophotonic device that has been used clinically since at least the 1930s for monitoring cardiovascular activity [6, 7, 8]. These devices have been used to assess cardiovascular factors such as blood oxygen saturation, heart rate, autonomic function, and peripheral vascular disease [7]. In a typical setup, contact PPG devices are fastened to the skin at peripheral sites, most commonly the finger, ear lobe, or toe [7]. Standard devices are comprised of either a single or multiple light-emitting diodes (LED) and a photodetector, and monitor cardiovascular activity by evaluating the change in light intensity due to fluctuations in blood volume. However, contact PPG devices are unable to provide systemic cardiovascular function due to their single-point detection design.

In light of this fundamental limitation, non-contact photoplethysmographic imaging (PPGI) systems have been proposed. PPGI systems are non-contact biophotonic cardiovascular monitoring systems that may provide touchless, non-invasive cardiovascular monitoring. Although existing designs differ, they are primarily comprised of the same primary components as contact PPG: a light source (LED) and a light detector (camera). Such systems rely either on active [9,10,11,12,13,14] or ambient tissue illumination [15,16,17,18,19]. Both active and ambient PPGI systems are sensitive to temporal changes in uncontrolled ambient illumination. The severity of this effect on the system's ability to extract the subtle blood pulse signal is apparent with studies employing data collection in dark room settings [9, 11, 12, 14]. Normalizing ambient illumination changes using software has been proposed [19]; however, this technique relies on a spectral estimation of the ambient illumination, which may fail in difficult lighting conditions.

Long-distance (supermeter) monitoring is unrealistic with contact PPG devices, since they are either attached via a cable to a monitor, must store the data on the device, or must transmit the data wirelessly, resulting in the need for a specialized network infrastructure. Still, one device can only monitor one anatomical location. In contrast, PPGI systems may acquire long-distance widefield measurements of large tissue regions that fit within the camera's field of view. However, long-distance monitoring becomes challenging with existing systems. Many existing PPGI systems operate in reflectance mode, where the

camera and illumination are positioned on the same side of the tissue under investigation. In addition to the weakened reflectance signal by the highly scattering nature of skin [20,21], reflectance PPGI systems using divergent light sources are sensitive to a strong illumination intensity decrease. These factors render long-distance monitoring a challenging problem.

1.2 Challenges and Objectives

PPGI systems present a set of unique challenges due to their non-contact nature, thus decoupling the monitoring system from the individual. Furthermore, the diffuse nature of light-tissue interaction necessitates informed system design decisions for evaluating vascular hemodynamics (this will be discussed more in Chapter 2). Specific challenges are discussed below.

- The first challenge relates to the design and development of a computational biophotonic imaging system for assessing pulsatile blood flow. Such a system must co-integrate the fields of biomedical optics with biomedical image and signal processing into a self-contained system capable of widefield tissue imaging.
- Although heart rate extraction from videos has been demonstrated, little effort has investigated whether widefield biophotonic imaging is able to localize both spatial and temporal characteristics of pulsatile blood flow for cardiovascular function assessment in different tissue regions. A primary challenge is therefore to study whether the spatial and temporal characteristics of major arterial and venous blood flow can be localized using a biophotonic imaging system.
- Clinically-relevant biomedical applications of biophotonic imaging systems have been largely unexplored. These are critically important for evaluating the system's clinical and preclinical viability. As a first step, experimental systematic PPGI evaluation must show clinically relevant information in a non-contact widefield manner.

Non-contact widefield hemodynamic imaging may have large biomedical implications for cardiovascular assessment and monitoring. The utility of such a system requires spatiotemporal cardiovascular monitoring beyond high-level physiological descriptors (e.g., heart rate). To this end, the following primary objectives are addressed throughout this thesis:

- The primary objective is to propose a new PPGI system capable of assessing spatiotemporal pulsatile blood flow. A successful system is one that can be used to enable new ways of assessing blood flow over large tissue regions.
- The second objective is the development of a biomedical image processing algorithm for automatically extracting a hemodynamic signal from a set of frames acquired using the aforementioned imaging system.
- The third objective is to study biomedically relevant applications for widefield tissue perfusion assessment which cannot be performed using existing contact-based probes. In particular, the use of such a non-contact imaging system was evaluated for assessing spatial blood flow distributions, the jugular venous pulse waveform to elucidate cardiac function, and non-contact assessment of irregular cardiac function.

1.3 Contributions

The primary contributions of this thesis are as follows:

- *A novel photoplethysmographic imaging (PPGI) system, coded hemodynamic imaging (CHI) that is capable of assessing spatial and temporal vascular pulsatility characteristics over large tissue regions.* This system co-integrates optical, electrical, hardware and software subsystems to assess vascular pulsatility. Deep penetrating near infrared light probes the tissue vasculature. A computational biophotonic model and signal processing pipeline extract local hemodynamic information resulting from dynamic tissue optical property changes.
- *A novel spectral-spatial pixel fusion method for automatically extracting a blood pulse waveform signal from a set of hemodynamic frames.* The waveform extraction method is posed as a Bayesian least squares optimization problem for assessing an optimal set of pixel weights based on physiologically motivated signal characteristics. Pixels are then weighted according to their computed pulsatility probability metric, resulting in an aggregate blood pulse waveform. The resulting framework is theoretically invariant to anatomical location and spectral composition.
- *Spatial probabilistic pulsatility analysis framework for assessing common pulsatile pathways in target demographics.* Experimental evaluation using a 24 participant sample of varying demographics resulted in a pulsatility distribution map for the head and neck, providing insight for enhancing future PPGI systems.

- *Non-contact biophotonic assessment of the jugular venous pulse waveform (JVP) using CHI.* Non-invasive methods for assessing JVP are clinically relevant for detecting right atrial cardiac dysfunction, since JVP analysis is currently performed by invasive right atrium catheterization. This study showed that biophotonic technologies are able to assess the JVP using deep penetrating near infrared light.

- *Non-contact biophotonic assessment of cardiac arrhythmia using CHI.* Cardiac arrhythmias (cardiac electrical abnormalities) commonly go undetected for a period of time, though early detection and intervention can drastically improve the individual's prognosis. This study demonstrated that non-intrusive PPGI assessment can be used to detect a cardiac arrhythmia in a naturalistic setting.

1.4 Thesis Structure

The remainder of the thesis is organized as follows. Chapter 2 provides requisite background material for motivating and understanding the research direction and contribution. Chapter 3 discusses the proposed biophotonic system, coded hemodynamic imaging (CHI), for assessing spatiotemporal hemodynamics. Chapter 4 provides a physiologically motivated mathematical framework for automatically extracting a blood pulse waveform from a series of frames acquired using CHI. Chapter 5 presents biomedical application studies, including aggregate spatial pulsatility analysis, biophotonic jugular venous pulse waveform assessed, and non-contact arrhythmia detection. Chapter 6 concludes the thesis with a summary of contributions and proposes future work.

Chapter 2

Background

This chapter provides requisite background material for motivating this thesis' contributions. In particular, requisite physiology, tissue optics, and motivating vascular assessment theory are presented. Chapter 2.1 provides a brief explanation of the physiology of pulsatile blood flow. Chapter 2.2 provides relevant tissue optics phenomena related to optical vascular assessment. Chapter 2.3 provides a description of photoplethysmography, the optical detection of pulsatile arterial flow in contact-based sensors. Chapter 2.4 provides an overview on the state of photoplethysmographic imaging, including a brief history of the nascent imaging modality and the general state of research.

2.1 Pulsatile Blood Flow: A Physiology Primer

To understand the nature of the blood pulse waveform (see Figure 2.1), we must first analyse the cardiac cycle before blood is ejected into the arterial tree. Blood enters the heart from the vena cava into the right atrium in a deoxygenated state, since this blood had

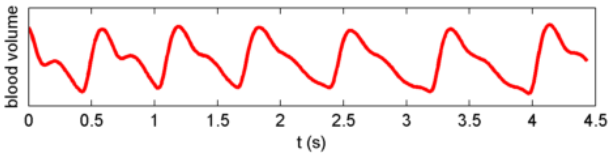

Figure 2.1: Example of an arterial blood pulse waveform. Peaks occur during systole, and valleys occur during diastole.

undergone gas exchange at tissues with oxygen demand. During the first heart contraction, the blood is ejected from the right atrium into the right ventricle, and then toward the lungs through the pulmonary vein. Inspired oxygen undergoes diffuse transfer to the blood (hemoglobin) through the thin capillary walls as it slowly passes across the alveoli in the lungs. This oxygenated blood (>95% oxygen saturation normally) returns to the left atrium, and the next heart contraction transfers blood from the left atrium into the left ventricle, and vigorously ejects a volume of blood ("stroke volume") through the aorta. The blood is dispersed throughout the body via the arterial tree, largely maintaining its oxygenated state due primarily to the thick arterial walls and wide lumen. Starting at the aorta, arteries bifurcate, splitting in a fork-like fashion, to deliver oxygenated blood throughout the body. At each bifurcation, the cross sectional area of the artery is reduced. Vessels at peripheral sites generally have small diameters relative to the major arteries (e.g., carotid artery, brachial artery, femoral artery). Arterioles are small arteries that still exhibit pulsatility. That is, the elastic walls of the arterioles expand to accommodate the increase in intramural pressure. Capillaries are thin-walled vessels that can allow a single red blood cell to flow through, allowing oxygen perfusion and waste removal, and primarily do not exhibit pulsatility. Venules connect capillaries to the vein network, delivering the deoxygenated blood back to the heart through the venous system.

Since arteries and arterioles exhibit pulsatile motion, these vessels will expand to accommodate the incoming blood from the vigorous heart contraction. As they expand and fill with oxygenated blood, the relative blood volume of the tissue increases. The peak point is termed "systole", relating to the maximum intramural pressure. Once the pressure wave travels through, the arterial walls relax, and the blood volume decreases. This is termed "diastole", relating to the time at which intramural pressure is at a minimum. The second smaller peak in a single pulse, the "dicrotic wave" (see Figure 2.1), forms from reflected waves at peripheral sites and transient pressure fluctuations from aortic valve closure in major arteries near the heart. It has been shown that this wave changes with age [22], and is an indicator of arterial stiffness and hypertension [23]. This becomes an important factor for designing a system that is robust to age, and may act as a diagnostic tool for arterial health.

The functional differences of oxygenated and deoxygenated blood are relevant to spectral composition. The primary oxygen carrying molecules in blood are the heme groups found in red blood cells. Each cell contains hundreds of thousands of molecules called hemoglobin, and each hemoglobin molecule is able to bind up to four oxygen molecules. Thus, the oxygenated state of blood refers to the average oxygenated state of the hemoglobin molecules present in a volume of blood. These are often referred to as oxyhemoglobin and deoxyhemoglobin. It is these two states of hemoglobin that determine the perceived colour

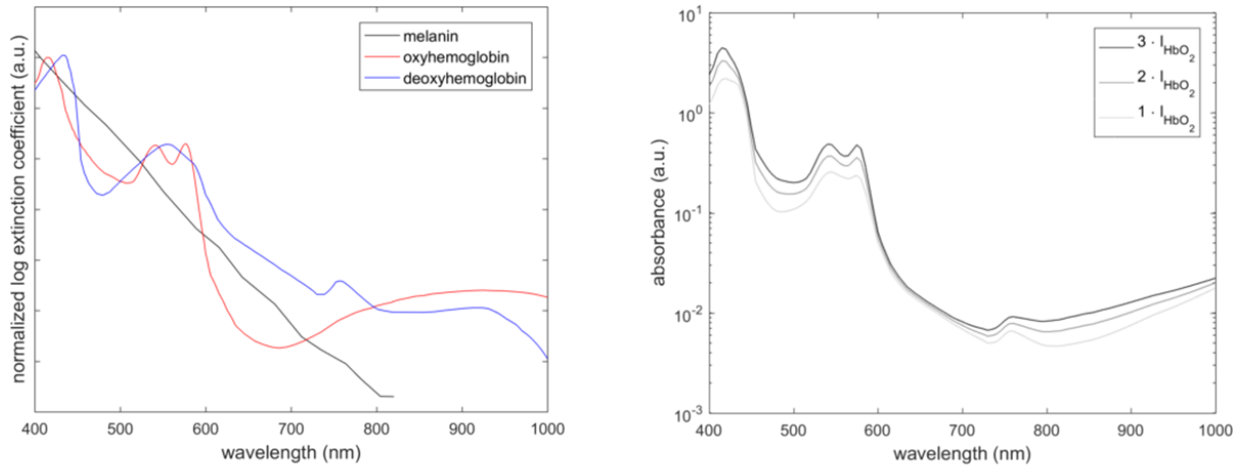

(a) Primary skin chromophores

(b) Effect of increased oxyhemoglobin

Figure 2.2: Spectral absorption properties of the three primary skin chromophores using published extinction coefficients [24, 25]. (a) Normalized log extinction coefficient curves for melanin, oxyhemoglobin, and deoxyhemoglobin. (b) Effect of increased oxyhemoglobin on absorption. This shows that local increases in oxyhemoglobin resulting from a blood pulse waveform will increase the absorption at certain wavelengths. This must be balanced with photon penetration depth, which is not incorporated in this simplified model.

of blood according to their absorption spectra (see Figure 2.2). That is, they are the primary light absorbing medium in blood. For example, both appear red due to the relatively high blue ($\approx$ 475 nm) and green ($\approx$ 510 nm) absorption, but deoxyhemoglobin appears darker than oxyhemoglobin due to its higher absorption in the red spectrum ($\approx$ 650 nm).

2.2 Tissue Optics

Light transport in tissue is largely governed by two inherent properties: absorption and scattering [26]. Absorption is functionally a reduction in light intensity at certain wavelengths due to constituent chromophores. Scattering is the change in light direction due to the tissues components' gradients and discontinuities in optical refractive index. Both of these characteristics are functions of wavelength (see, for example, Figure 2.2 for the spectral extinction coefficients of dominant tissue chromophores). Since the tissue type under consideration is skin, the discussion presented here will be constrained to tissue optics within skin.

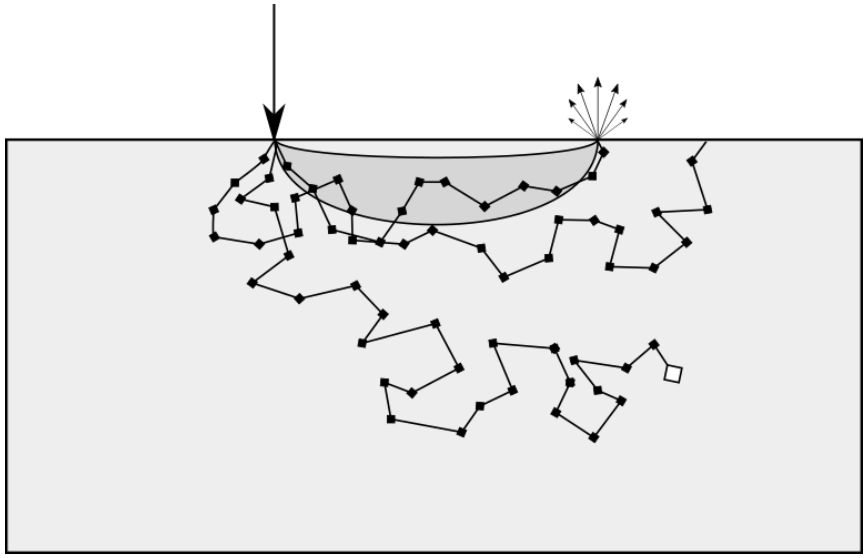

Figure 2.3: Simplified graphical depiction of photon migration in tissue. Three example photon paths are shown here. Light entering into the tissue (large arrow) undergoes a series of scattering and absorption events, before either getting emitted at the surface (closed diamonds) or absorbed (open diamond). Photon attenuation is largely influenced by scattering-induced path length. In a configuration where a source and detector are separated by a certain distance, the mean photon path from a source to a detector through tissue generally follows a shape often referred to as a "photon banana" [26] (gray curve). The goal in hemodynamic imaging is to detect diffusely scattered and reflected photons that have undergone hemoglobin-induced absorption events.

2.2.1 Light Transport in Skin

When a tissue is illuminated, the photons undergo a series of absorption and scattering events according to the tissue's properties. When a photon encounters a scattering particle, its path is redirected. Eventually, some photons migrate back to the surface after a series of scattering and perhaps absorption events. These photons are emitted and detected by biophotonic technologies. Light transport through tissue is a complex process, often modeled as a series of random walks. Due to the predominantly forward scattering nature of tissue, tissue photon migration by a point source illuminant to a point detector is often described as having a "photon banana" shape [26]. Specifically, the light field in tissue based on single-point illuminant and point-based sensing exhibits an arc-like shape. The shape of the light field (and thus depth of penetration) depends on several factors, such

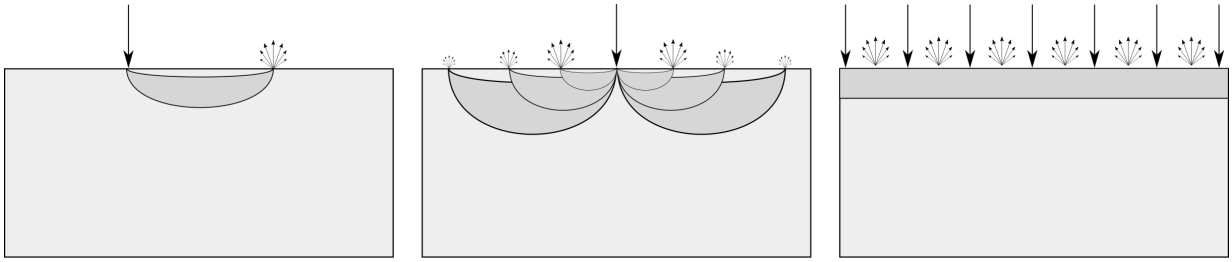

Figure 2.4: Photon migration in tissue and sensing for different source and detector configurations. The dark gray area represents the continuous wave sensitivity region.

as illumination wavelength, source-detector separation, and tissue composition. Figure 2.3 provides a graphical depiction of this photon migration process. The goal in hemodynamic imaging is to detect remitted photons that have undergone hemoglobin-induced spectral absorption, and quantify the relative changes across a tissue region.

In an imaging setup, a point source illuminant is insufficient for monitoring large tissue regions. Instead, broad source illuminants (e.g., LEDs) are used to illuminate the tissue region of interest. The remitted light therefore is a result of a collection of photon banana paths. Figure 2.4 shows a simplified view of the mean paths traveled by detected photons in tissue based on different sensing configurations. A point source illuminant would provide insufficient remitted light across the whole tissue for widefield imaging (Figure 2.4b). In a widefield illumination configuration, an infinite number of source-detector pairings result in high-resolution tissue imaging capabilities (Figure 2.4c).

An important quantity for describing tissue optics is the *absorption coefficient*. The absorption coefficient, μ_a [mm^{-1}], describes the probability of photon absorption per unit length [26]. This value is governed by the tissue's light absorbing chromophores and other absorbing media:

$$\mu_a = \sum_i \ln(10)\varepsilon_i c_i \tag{2.1}$$

where ε_i and c_i are the molar extinction coefficient and concentration for the light absorbing component i (e.g., oxyhemoglobin, deoxyhemoglobin, melanin, water, lipid, etc.). It is important to note that absorption is a spectral characteristic. That is, molar extinction coefficient is highly dependent on wavelength (see Figure 2.2). However, for notational convenience, we will adopt μ_a to refer to $\mu_a(\lambda)$. One can also consider the absorption

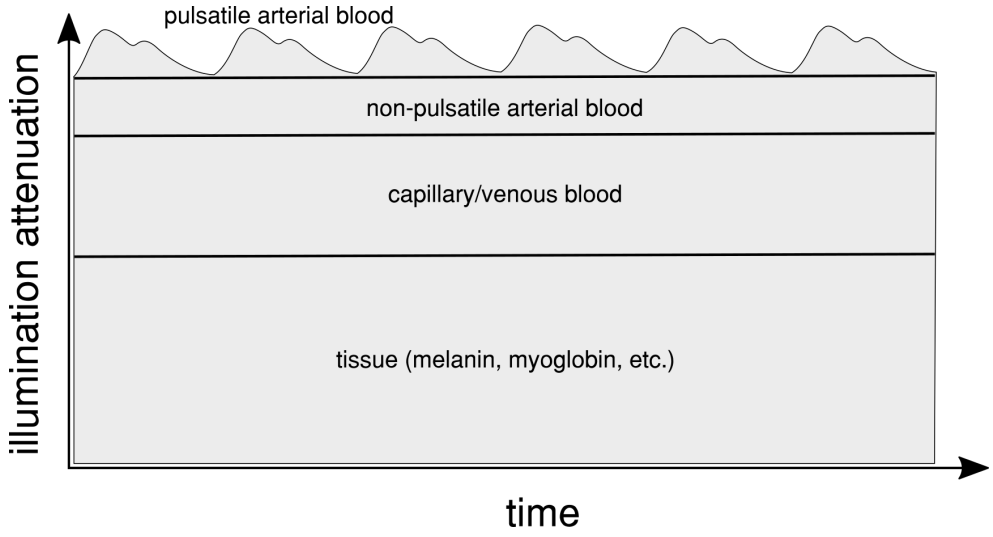

Figure 2.5: Simplified temporal illumination attenuation model in tissues containing pulsatile arteries. The majority of the light attenuation is due to static tissue absorbers such as melanin, capillary beds, and venous blood. The primary contributors to the temporal dynamics are the hemodynamic arterial pulsations. These signals are subtle, and require explicit system design for clean signal extraction.

mean free path of a photon traveling through homogeneous tissue:

$$\text{mfp}_a = \frac{1}{\mu_a} \text{ [mm]} \tag{2.2}$$

This is particularly relevant to hemodynamic imaging. Figure 2.5 shows the different layers of absorption in tissue consisting of a pulsating artery. A common assumption made when considering bulk tissue properties is that absorption is not temporally varying ($\mu_a(t) = \mu_{a0}$). However, though much of the light attenuation is due to the static absorbing media (surrounding tissue, capillary bed, venous blood, non-pulsatile arterial blood), the local changes in blood volume result in absorption fluctuations. In a reflectance geometry, this change in absorption is probably due to both mechanical deformation of the vascular bed as well as a transient increase in photon path length through oxyhemoglobin due to the distended artery [8, 27]. Thus, $\mu_a = \mu_a(t)$, and the increased path length results in a large number of absorption events according to the mean free path.

2.2.2 Skin Chromophores

Skin is a highly diffuse media where its spectral optical properties in the visible-near infrared range is highly nonlinear [28]. Skin tissue models primarily contain up of three absorbing and scattering constituents: melanin, oxyhemoglobin, and deoxyhemoglobin. The combination of these constituents results in a tissue's bulk absorbing and scattering characteristics.

Melanin

Melanin is a primary tissue chromophore in the visible regime, and is responsible for producing perceived skin tone, arising from its highly absorbing nature in the visible regime. The degree of absorption is dependent on melanin concentration, melanosome volume fraction, and epidermal thickness. These properties vary between individuals and also between anatomical locations. Typical melanosome volume fraction ranges from 1–3% for weakly pigmented skin, 11–16% for tanned Caucasian skin, and 18–43% for darkly pigmented skin [29]. Epidermal thickness in the face, which is of particular interest to hemodynamic imaging, varies between 30–63 μm [30]. Melanin exhibits very high absorption in the blue and green spectra, with a non-linear decrease that is approximately inverse-exponential (see Figure 2.2). Epidermal optics hold no hemodynamic value, and thus may be considered as sources of noise for this application. It is therefore desirable to image in the near infrared spectrum, where melanin absorption is relatively low. Additionally, skin exhibits weaker scattering at these higher wavelengths, enabling deeper penetration depth. In particular, experimental data are fit well by an inverse power law [28]:

$$\mu_s' = a\left(\frac{\lambda}{500\ [\text{nm}]}\right)^{-b} \tag{2.3}$$

where, in skin, $b \approx 1.4$ [28].

Hemoglobin

There are two primary forms of light-absorbing hemoglobin: oxyhemoglobin (HbO_2) and deoxyhemoglobin (Hb). As previously discussed, HbO_2 are hemoglobin molecules with up to four bound oxygen molecules. The two molecules produce distinct absorption spectra, as seen in Figure 2.2. Of particular note are the absorption magnitude differences in the red and infrared spectra (600–1000 nm), with a particularly important "isosbestic" point at

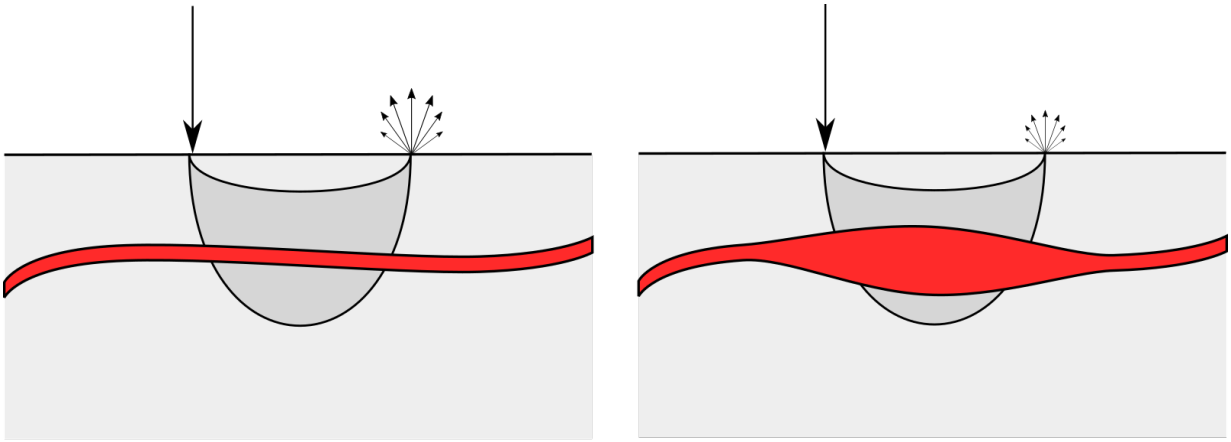

Figure 2.6: Biophotonic effect of a local change in blood volume. (a) During diastole, the blood vessel is relaxed and the photonic absorption due to hemoglobin is at a minimum. (b) During systole, the local increase in blood volume results in a larger path length through the oxyhemoglobin medium, resulting in an overall decrease in remitted photons compared to diastole.

805 nm where the two curves cross over. Below this point (600–805 nm), Hb is the primary absorber, where HbO_2 exhibits a local minimum at 685 nm, and melanin still exhibits relatively strong absorption properties. Above the isosbestic point (805–1000 nm), HbO_2 is the dominant absorber, and melanin's absorbing properties have reduced considerably $\left(\frac{\varepsilon_{mel,820}}{\varepsilon_{mel,615}} = 0.37\right)$ [25]. This range is therefore particularly well-suited for assessing arterial pulsatility.

2.2.3 Tissue Optics Relevant to Hemodynamics

Optical tissue properties in the range of approximately 650–1100 nm is often referred to as the "optical window" for tissue investigation. In this "diffusive" spectral range, scattering dominates absorption by an order of magnitude, where generally $\mu_s'/\mu_a \approx 10^2$ [31]. The combination of increased penetration depth (due to reduced bulk tissue absorption and scattering) and differential absorption curves provide powerful biophotonic investigative properties. Of similar importance, optical sensing in this spectral range is also feasible in practice, with many current CCD and CMOS sensors exhibiting good quantum efficiency into the near infrared regime.

In the context of hemodynamic imaging, two biophotonic characteristics are desired: deep tissue penetration and hemoglobin absorption. Bulk tissue penetration can be optimized based on the spectral selection, as discussed above. Blood pulse waveforms arise from relative changes in observed light intensity due to differential optical absorption resulting from local differential blood volume changes. When considering arterial pulsations, high oxyhemoglobin absorption is desirable to produce an intensity signal that highly correlates to the changes in blood volume.

2.3 Photoplethysmography

Photoplethysmography (PPG) devices are widely used cardiovascular biophotonic devices for assessing the arterial pulse waveform. PPG devices are commonly operated in transmittance geometry on thin anatomical locations (e.g., finger, ear lobe) [7]. Most PPG devices are comprised of one or more LEDs, and a photodiode. LEDs are popular light sources for scientific use due to their narrow spectral bandwidth and low cost. Photodiodes convert incident light into an analog electrical signal. These components are positioned to sit against the anatomy, thus blocking out ambient light.

The blood pulse waveform is fundamentally a signal describing local blood volume changes. The standard way to compute this signal is by using the Beer-Lambert law of light attenuation. The transmitted illumination φ_T is computed as:

$$\varphi_T = \varphi_0 e^{-\mu_a l} \tag{2.4}$$

where φ_0 is the incident illumination and l is the photon path length. In transmittance geometry, where light penetrates the tissue entirely, local arterial distensions expand the surrounding tissue to accommodate the transient blood volume increase, thus effectively increasing the photon path length through oxyhemoglobin [8]. The temporal dynamics can therefore be expressed as:

$$\varphi_T(t) = \varphi_0 e^{-\mu_a l(t)} \tag{2.5}$$

Thus, a change in blood volume results in a change of $l(t)$, whose dynamics are determined by measuring $\varphi_T(t)$. In practice, since the device is a fixed system, the incident illumination strength can be electronically stabilized. Thus, the only required measurement for visualization blood pulses is $\varphi_T(t)$. By powering a constant illumination φ_0 via the LED, the photodiode measures the signal $\varphi_T(t)$. From this measurement, absorbance is computed as:

$$a_{PPG}(t) = -\log \varphi_T(t) \tag{2.6}$$

PPG has several significant drawbacks relevant to both long-term monitoring and monitoring in natural settings. PPG devices are privy to motion artefacts [7]. Since the LED and photodiode are in direct contact with the anatomical surface, slight movements could cause LED reorientation or ambient light leakage, leading to skewed data. There is little contextual information available for movement artefact correction, so it remains a difficult problem. The location of contact of PPG devices is limited to the design of the device. Transmittance devices can only operate where light can transmit through the entire tissue, limiting its scope to areas such as ear lobes, fingertips, and toes [7]. Care must be taken when affixing reflectance PPG devices, as movement, ambient light, and relative positioning to the tissue can cause skewed results. Finally, spring-loaded PPG devices may become uncomfortable over long periods of time, and the pressure could lead to reduced peripheral blood flow.

2.4 Photoplethysmographic Imaging

Photoplethysmographic imaging (PPGI) systems are widefield biophotonic hemodynamic imaging systems that address the aforementioned drawbacks of contact-based sensors, and provide unique advantages over single-point contact sensors. By co-integrating optical design, electronic control, computational biophotonic models, and image and signal processing methods, PPGI systems are able to assess hemodynamic pulsatility across large tissue regions. Modeling pixels as "virtual sensors", each virtual sensor response can be evaluated to determine spatiotemporal pulsatility characteristics.

PPGI is a nascent concept, with one of the first PPGI devices reported in 2002 by Hulsbusch and Blazek [32]. The system consisted of a thermally cooled charge-coupled device (CCD) with high near infrared (NIR) sensitivity positioned 20 cm from the skin, with an LED array (the wavelength was not specified). The novelty was described as being able to evaluate PPG-like signals in wounds, where a contact device would not be feasible. However, the camera was an expensive and bulky one, hinting at device feasibility issues. The next major reported advancement came in 2005 by Wieringa *et al.* [9]. The device consisted of a monochrome complementary metal-oxide-semiconductor (CMOS) camera positioned 72 cm from the skin and 300 LEDs at three different wavelengths in the red and NIR electromagnetic spectra (660 nm, 810 nm, 940 nm). Three independent videos were obtained, one for each wavelength. Results were promising, but hampered by poor camera SNR at longer wavelengths and motion artefacts due to independently acquired videos.

In 2007, Humphreys *et al.* expanded on this design [10]. Illumination and acquisition were performed automatically via software triggers at a distance of 30 cm from the skin.

The imaging device was able to capture distinct PPG-like signals, however the LED array required high power to overcome the low camera sensitivity in the NIR spectrum (7.9% and 15% at 760 nm and 850 nm respectively).

Though the number of papers published in PPGI literature has been growing, there have been three primary gaps in the literature: (1) lack of spatiotemporal pulsatility analysis; (2) lack of physiologically-motivated hemodynamic image processing extraction methods; (3) lack of biomedical applications. These challenges are discussed further in the subsequent sections, and are the primary motivating challenges for this thesis.

2.4.1 Spatiotemporal Pulsatility Analysis

A primary advantage of PPGI systems over contact-based sensors is widefield tissue monitoring. Modeling each pixel as a "virtual sensor", a 1 megapixel camera can effectively capture signals from 1 million virtual sensors across a tissue region, enabling new insights into cardiovascular health and spatial perfusion. For example, pulse transit time between central and distal arterial locations can provide a proxy metric that correlates to systemic blood pressure [33, 34, 35], and perfusion inhomogeneities can provide insight into tissue health and healing [5,36,37]. Widefield imaging analysis can provide preclinical and clinical insight that supports early abnormality detection for proactive and preventive healthcare intervention. However, this type of biomedical analysis has not been extensively explored in PPGI literature. Many studies have focused on extracting aggregate statistics (e.g., heart rate, heart rate variability) or a single blood pulse waveform from the scene [38]. This type of analysis assumes no variance in the pulsatile signals across the tissue region, and therefore may miss crucial perfusion information. Spatial pulsatility assessment has great potential to provide novel physiological insight into tissue perfusion and hemodynamic variability.

Furthermore, many existing studies perform signal analysis in the frequency domain via Fourier decomposition. This type of analysis assumes the hemodynamic signal is a periodic one, when in fact this is not the case. Although assuming the blood pulse waveform is a periodic signal at the heart rate frequency is a good first order approximation of a normal blood pulse waveform, this type of analysis is insensitive to heart rate variability and various cardiac diseases. For example, cardiac arrhythmias such as premature atrial and ventricular contractions, atrial fibrillation, and heart block result in temporal variances in the hemodynamic signal [39], which would be improperly modeled in a frequency decomposition framework. Though cardiac disease detection is an important application of PPGI systems, its ability to detect disease states has not been thoroughly investigated.

2.4.2 Hemodynamic Signal Extraction

An active area of research seeks to develop methods for automatically extracting a hemodynamic signal from a set of frames for automatic cardiac abnormality detection (e.g., cardiac arrhythmia). The fundamental challenges in this problem arise from the heterogeneous mixture of pixels in a scene, of which only a subset may undergo hemodynamic pulsatility. For example, a frame may include background pixels (e.g., furniture, equipment, etc.) and non-pulsatile anatomical regions (e.g., weakly vascularized areas, hair, etc.). The problem then becomes a spatial distribution problem, where a spatial distribution must be estimated for assessing only relevant pixels.

The first reported methods performed bulk spatial averaging to assess heart rate [15, 16, 17, 18, 19, 40]. These methods implicitly assume that the strength of pulsatility exhibited by the relevant pixels will dominate the other "noisy" pixels. For example, the region of interest identified by facial tracking algorithms can be used to identify the head and subsequently bulk averaged [16, 40], which has been effective for evaluating heart rate during exercise-induced motion [14]. However, this bulk averaging is suboptimal since irrelevant pixels introduce spurious components into the final signal. To address this, other methods have proposed extracting average pixel intensity across specific (relative) spatial regions [41, 42, 43]. In these methods, homogeneous tissue regions were selected, avoiding areas such as the eyes and nose. These are often found relative to the region of interest identified by a facial tracking algorithm, which limit its applicability beyond facial assessment.

Another set of methods have focused on selecting or weighting pixel values based on their perceived signal strength [43, 44, 45, 46, 47]. These methods compute signal strength weights for each pixel signal based on a formulated goodness metric, which are used in a weighted-sum fashion to extract the blood pulse waveform. These methods have shown significant improvement over naive averaging approaches, however these methods rely on fundamental assumptions about illumination spectral composition, estimated heart rate, and anatomical location. There is therefore a need for signal fusion methods that are void of assumptions about illumination, heart rate, and anatomical location for use in various PPGI systems. In fact, there have been very few studies that have analyzed anatomical areas other than the face and hands. This may be due to ease of data collection, as many data sets are captured in normal environments. However, a broader spatial field of view may provide additional cardiovascular insights, such as pulse transit characteristics.

2.4.3 Ambient Monitoring

Many studies employ the use of ambient illumination (e.g., sunlight, office lighting, etc.) as the illumination source. This setup has unique problems as the lighting conditions are completely uncontrolled. For example, if the scene is illuminated with daylight, changes in cloud cover and sun exposure will affect the reflectance signal [17]. Movement also becomes a problem since it cannot be assumed that the light source is coming from directly behind the camera, leading to lighting variations within the scene. In a natural setting, there may also be other individuals that occlude light sources in their walking path.

Though a number of studies have demonstrated non-contact heart rate estimation using ambient light [15,16,17,18,19,43,48], it is unclear whether these methods can be extended beyond the study's setup and applied broadly for any ambient light source. For example, there are a vast collection of illumination types which exhibit highly varying spectral emission curves. A light that may appear white to the human eye may in fact be composed of only a few dominant wavelengths. Thus, certain ambient illuminants may be insufficient for penetrating the vasculature.

Ambient illumination PPGI studies have generally made use of the RGB camera channels for pulsatility detection in three ways. Some studies have modeled each colour channel as having different light-tissue interaction properties [19, 45, 46]. For example, blue light has very shallow penetration in skin, and can therefore be used to model environmental noise (e.g., illumination fluctuation or skin movement) [12]. Other studies have taken a purely signal processing approach, without much biomedical optics motivation. Many methods have used signal decomposition methods, such as independent component analysis (ICA) [16,38,40,41]. These methods were modeled with the assumption that the observed signals (e.g., colour channels) are comprised of a combination of underlying structured signals (e.g., hemodynamic pulsatility, movement, camera noise, etc.). The goal is therefore to extract the structured hemodynamic signal from the noisy pixel signals. However, generally these methods require large sampling times for robust signal extraction, and clinical applications have been lacking.

2.4.4 Summary

This chapter presented the requisite physiology, tissue optics, and literature background for the remainder of the thesis. Methods presented throughout the thesis will be motivated by these primary physiological hemodynamic mechanisms. Building on these background materials, Chapter 3 will present the design of a hemodynamic imaging system for eval-

uating spatial and temporal hemodynamic pulsatility. Data collected using this imaging system will be used throughout the remainder of this thesis.

Chapter 3

Coded Hemodynamic Imaging: A Biophotonic System for Spatiotemporal Hemodynamic Pulsatility Assessment

3.1 Introduction

This chapter presents a novel photoplethysmographic imaging system, coded hemodynamic imaging (CHI), for spatiotemporal hemodynamic pulsatile blood flow assessment. This biophotonic system was designed to use tissue-penetrating optics for assessing hemodynamic pulsatility across a large tissue region. A primary challenge of non-contact widefield monitoring systems is ambient illumination corruption. Optical models are developed assuming specific light-tissue interaction properties, which is infeasible for uncontrolled ambient illumination (hence "coded" imaging).

This chapter is organized as follows. Chapter 3.2 presents an optical model for extracting spatiotemporal hemodynamic signals. Chapter 3.3 discusses the selected illumination spectrum based on theoretical tissue optical properties. Chapter 3.4 presents an image and signal processing framework for extracting clean pulsatile waveforms from noisy measurement conditions. Chapter 3.5 presents signal assessment metric used throughout this thesis. Chapter 3.6 presents the design and development of the physical instrumentation for collecting hemodynamic imaging data using the theoretical model to guide the design.

3.2 Optical Model

We used a modified temporal Beer-Lambert light attenuation model to characterize light-tissue interaction dynamics. This model is suitable for meso/macroscopic, real-time detection and analysis. The presented model does not require assumptions about detailed tissue optical properties, and thus is theoretically robust to different tissue compositions.

Fundamentally, the Beer-Lambert model relates light output based on the attenuation of light input by the medium's light-absorbing capacity. Light undergoes absorption events according to the chromophores' molar extinction coefficients, concentration, and photon path length. This model follows an inverse exponential decay [26]:

$$\varphi(\lambda) = \varphi_0 e^{-\mu_a(\lambda) l} \tag{3.1}$$

where $\varphi(\lambda)$ is the radiated illumination at wavelength λ from the tissue surface, φ_0 is the incident illumination on the tissue surface, ε $[\text{mm}]^{-1}(\text{mol/L})^{-1}]$ is the tabulated molar extinction coefficient, c [mol/L] is the chromophore concentration, and l [cm] is the photon path length through the chromophore concentration. The absorption coefficient, $\mu_a = \ln 10 \varepsilon c$, is often used to differentiate the effects of chromophore absorption and photon migration. Henceforth, the wavelength term λ will be omitted for notational convenience, but will be specifically addressed later.

This model is insufficient for highly scattering media such as skin [28], since it attributes light attenuation solely to absorption. Thus, a constant loss factor G is often added to model loss due to scatter [26, 49]:

$$\varphi = \varphi_0 e^{-\varepsilon c l} = \varphi_0 e^{-(\mu_a l + G)} \tag{3.2}$$

This is a unitless measure that describes the ratio of illumination output to input. When imaging human tissue, this general model must be adapted to the constituent chromophores (a molecule's atomic group that is responsible for spectral absorption). The major chromophores in the visible-near infrared region are oxyhemoglobin, deoxyhemoglobin, and melanin [28]. Thus, photon attenuation results from the combination of the individual chromophores:

$$\varphi = \varphi_0 \exp\Big(-\big(\underbrace{\mu_{a,HbO_2} l_{HbO_2}}_{\text{oxyhemoglobin}} + \underbrace{\mu_{a,Hb} l_{Hb}}_{\text{deoxyhemoglobin}} + \underbrace{\mu_{a,mel} l_{mel}}_{\text{melanin}} + \underbrace{G}_{\text{scatter loss}}\big)\Big) \tag{3.3}$$

Conceptually, the blood pulse waveform signal is a temporal signal describing the temporal fluctuations resulting from transit local changes in blood volume. We are therefore primarily concerned with the temporal relationship of light intensity:

$$\varphi(t) = \varphi_0 \exp\Big(-\big(\mu_{a,HbO_2} l_{HbO_2}(t) + \mu_{a,Hb} l_{Hb} + \mu_{a,mel} l_{mel}\big) + G\big)\Big) \tag{3.4}$$

Notice that the only component in this model that changes with time is the photon path length through oxyhemoglobin. When the blood volume ejected from cardiac contraction arrives at a certain localized region, the tissue expands from arterial expansion, resulting increased path length of oxygenated hemoglobin [8]. The contributions of deoxyhemoglobin from the veins and tissue, melanin, and scatter loss are temporally invariant, and are therefore independent of time. This is illustrated in Figure 2.5. When considering temporal hemodynamics, these factors cancel out to yield an oxyhemoglobin-dominated signal:

$$\frac{\varphi(t)}{\varphi(t+\Delta t)} = \frac{\exp\big(-(\mu_{a,HbO_2} l_{HbO_2}(t) + \mu_{a,Hb} l_{Hb} + \mu_{a,mel} l_{mel} + G)}{\exp\big(-(\mu_{a,HbO_2} l_{HbO_2}(t+\Delta t) + \mu_{a,Hb} l_{Hb} + \mu_{a,mel} l_{mel} + G)} \tag{3.5}$$

$$\frac{\varphi(t)}{\varphi(t+\Delta t)} = \exp\big(-(\mu_{a,HbO_2} l_{HbO_2}(t) + \mu_{a,Hb} l_{Hb} + \mu_{a,mel} l_{mel} + G) \tag{3.6}$$

$$+ (\mu_{a,HbO_2} l_{HbO_2}(t+\Delta t) + \mu_{a,Hb} l_{Hb} + \mu_{a,mel} l_{mel} + G)\big) \tag{3.7}$$

$$\frac{\varphi(t)}{\varphi(t+\Delta t)} = \exp\big(-\mu_{a,HbO_2}(l_{HbO_2}(t) - l_{HbO_2}(t+\Delta t))\big) \tag{3.8}$$

The blood pulse waveform signal is in fact the temporal changes in absorbance, which can be computed from this relationship to quantify the blood pulse waveform signal:

$$a(t) = -\log\left(\frac{\varphi(t)}{\varphi_0}\right) \tag{3.9}$$

Thus, during imaging, by measuring the radiant output $\varphi(t)$, the blood pulse waveform can be extracted by computing the absorbance, which has been shown to model the change in path length through oxyhemoglobin. Local hemodynamics can be quantified and analysed from this blood pulse waveform. As we'll see later, this method will be used on a region-by-region basis, effectively quantifying a spatial distribution of blood pulse waveforms $a(x, y, t)$.

3.3 Illumination Selection

Illumination spectrum selection plays an important role in photon migration and thus imaging signal. For the purpose of this thesis, the discussion will be constrained to wavelengths to which silicon-based sensors are sensitive (typically 400–1000 nm). In the context of hemodynamic imaging, the optimal light-tissue interaction processes would be invariant to epidermis, would be strongly absorbed by oxyhemoglobin, and would exhibit deep penetration depth.

Epidermis contains a primary skin chromophore, melanin, which is responsible for perceived skin tone. It is highly absorbing in the blue spectrum, and has a dramatic non-linear decrease in absorbing strength with larger wavelengths. For example, melanin's extinction coefficient exhibits an 89% reduction at 820 nm compared to 407 nm [25]. Figure 2.2 shows the extinction coefficient of the primary chromophores found in skin, including melanin. Note how melanin's absorption properties decrease with larger wavelengths. Therefore, red and infrared wavelengths are preferred for reduced melanin absorption.

Strong hemoglobin absorption is important for extracting a reliable hemodynamic signal. Transient local changes in blood volume arising from vessel expansion are small. In the best case, major arteries often expand on the order of micrometres or low-millimetres. Hemodynamic changes are even further reduced in smaller arteries and arterioles [50]. However, this absorption strength must also be balanced with penetration depth and photon path length. Figure 2.2b demonstrates this trade-off. For example, green light at 550 nm undergoes high hemoglobin absorption, however the order of magnitude is too strong for adequate penetration into deep vasculature. In the case where $\mu_a \approx 0.5$ mm^{-1}, or equivalently a 2 mm mean free path, which is too small for multi-millimetre or centimetre penetration. Thus, near infrared wavelengths beyond the 805 nm isosbestic point (i.e., spectral cross-over) may be preferable, since they exhibit relatively strong oxyhemoglobin absorption with mean free paths in the centimetre range, and deeper penetration depth. This range exhibits desirable scattering-absorption properties, in which the ratio $\mu_s'/\mu_a > 30$ in the range of 800–1000 nm [31], where μ_s' [mm]$^{-1}$ is the reduced scattering coefficient describing the inverse mean free scatter path.

In practice, this spectral selection can be implemented in a number of different ways. Broadband illumination sources (e.g., tungsten-halogen bulb) can be used in conjunction with suitable optical filters for selecting desired spectral ranges. This offers the benefit of selecting different spectra using a single illumination source. However, these methods are generally power inefficient, since a large portion of the broadband source is being filtered out, and broadband incandescent sources lose a large amount of energy to heat. Another solution is the use of lasers. Lasers are coherent light sources that emit photons in a very narrow spectral band. However, depending on the type of laser, they may be cost prohibitive, bulky, and may pose issues with eye safety. Furthermore, the random speckle nature of laser projection may cause problems when extracting subtle blood pulse waveform signals. A solution to these problems is the use of light emitting diodes (LEDs). LEDs are incoherent light sources that emit relatively narrow spectral bandwidth, typically full-width half-max of 10 nm. Recent advances in LED technology have demonstrated improvements in radiant power, stability, and cost efficiency. Optical filters may be used to further narrow the spectral range of the emitted light. Their projection beam can be easily formed using

optical components. Their small size makes them particularly useful for an embedded portable imaging system.

3.4 Signal Processing

3.4.1 Problem Formulation

The signal captured using the given optical model may be affected by various sources of noise. This section presents a signal processing pipeline for extracting a stable pulsatile PPGI signal. First, a denoising step was developed to reduce the noise based on camera and process characteristics. Second, a detrending step is proposed, which removes trends in intensity due to external factors such as movement.

The subsequent signal processing methods are performed at each extracted hemodynamic signal z_l. This signal is the absorbance signal extracted using the optical model presented in Chapter 3.2. This signal can be modeled as a discretization of the temporal light intensity fluctuations:

$$z_l = \sum_{k=-\infty}^{\infty} a_l(t)\delta(t - kT) \tag{3.10}$$

where $a_l(t)$ is the continuous absorbance signal at tissue location l, T is the sampling period, and $\delta(n)$ is the Dirac delta function:

$$\delta(n) = \begin{cases} 1 & \text{if } n = 0, \\ 0 & \text{if } n \neq 0 \end{cases} \tag{3.11}$$

Henceforth, the location descriptor l will be omitted for notational convenience. Thus, z should be interpreted as z_l (i.e., the signal extracted at tissue location l).

In the subsequent sections, signals are analyzed in both the temporal and frequency domains, and thus the frequency domain formulation is presented here. Given an arbitrary signal z, the zero-DC frequency domain representation was computed using the Fourier transform:

$$Z_f = \sum_{n=0}^{N-1} z_n^* \cdot e^{-2\pi i f n/N} \tag{3.12}$$

where $z^*(t) = z(t) - \frac{1}{T}\int_0^T z(t)dt$ is the zero-DC signal. Here, Z_f are the complex-valued Fourier transform frequency coefficients for the temporal signal z^*. In order to compute

spectral properties, the normalized zero-DC spectral power distribution was computed:

$$\Gamma_f(z) = \frac{|Z_f|^2}{\sum_k |Z_k|^2} \in [0, 1] \tag{3.13}$$

This normalized spectral power (i.e., $\sum_f \Gamma_f(z) = 1$) was used to model the relative AC pulsatile amplitude in the unit-less blood pulse waveforms.

3.4.2 Denoising

The subtle blood pulse waveform may be corrupted by measurement noise (e.g., camera sensor noise), of which the magnitude can often dominate the small hemodynamically-induced light fluctuations. However, the true noise-free blood pulse waveform signal is often quasi-periodic, resulting in a small set of dominant frequency components. Figure 3.1 shows illustrative motivation of a typical power spectral density of a clean blood pulse waveform acquired from the finger. The spectral energy is compact, and is primarily composed of two harmonic frequencies. This demonstrates the quasi-periodic nature of the blood pulse waveform, and can be used as prior physiological information for designing a filtering system.

Leveraging this physiological knowledge, a frequency domain filtering method seems particularly well-suited for this application. Specifically, let $\Gamma_f(z)$ be the zero-DC spectral power distribution of signal z at tissue location l from Equation 3.13. This signal is modeled as an additive noise model, consisting of the blood pulse waveform signal and noise:

$$z = z_h + z_n \tag{3.14}$$

where z_h and z_n are the hemodynamic and noise signal, respectively. This noise model is further decomposed into two types of observed noise: measurement noise, and process noise:

$$z = \underbrace{z_h}_{\text{pulse signal}} + \underbrace{(z_m + z_p)}_{\text{noise}} \tag{3.15}$$

where z_m and z_p are the measurement and process noise, respectively. Of course, z_h is unknown, and must be estimated from the measured z signal. For this problem, measurement and process noise models are proposed below.

Measurement Noise Model

As discussed above, hemodynamic waveforms are quasi-periodic signals, consisting of a small set of frequencies which are primarily focussed around second and third harmonics of the fundamental heart rate frequency. Thus, measurement noise was modeled as signal mixtures whose frequency components were outside of the set of physiologically valid signals. A frequency bandpass filtering method can be effectively employed to isolate the blood pulse waveform from the measurement noise. The denoised signal, in frequency domain, was computed as:

$$\Gamma_f^*(z) = \Gamma_f(z)h(f) \tag{3.16}$$

where

$$h(f) = \begin{cases} 1, & \text{if } f > f_0 \text{ and } f < (\kappa+1)f_1 \\ 0, & \text{otherwise} \end{cases} \tag{3.17}$$

where f_0 is the lowest physiologically valid frequency, f_1 is the fundamental frequency representing heart rate, and κ is the fundamental frequency harmonic coefficient. A common choice is $\kappa = 1$, signifying one primary harmonic. f_0 and f_1 are chosen to represent extreme bradycardia (30 bpm) and tachycardia (200 bpm). The processed hemodynamic signal can then be reconstructed through an inverse Fourier transform:

$$\hat{z}_{h+p} = \frac{1}{N}\sum_{f=0}^{N-1} \Gamma_f^*(z) \cdot e^{2\pi i f n/N} \tag{3.18}$$

where $\hat{z}_{h+p} = z - z_m = z_h + z_p$ is the signal still corrupted with process noise z_p.

It should be noted that low frequency signal components may contain physiological information (e.g., respiratory information, blood pressure variations, Mayer waves, etc.). However, in this model, we seek to quantify the fundamental spatiotemporal hemodynamics, and thus treat these systemic contributions as "noise". Future work can seek to quantify these low frequency variations as separate signals rather than noise.

Process Noise Model

Fluctuations in lighting and measurement or process noise should be corrected using the measurement noise model. However, these corrections assume constant incident illumination, which is an invalid assumption during movement. The goal of this detrending step is to remove slow oscillations in the signal, yielding a stable hemodynamic signal. Movements were assumed to be relatively smooth over time (e.g., breathing, swaying). A detrending

algorithm was used on the denoised absorbance signal, in which the model assumes a smoothness prior [51]. In particular, the observed signal is modeled as a composition of a corrupted true signal:

$$z_{h+p} = z_h + z_p \tag{3.19}$$

where z_h is the "true" hemodynamic signal and z_p is a temporal trend. Given that z_{h+p} is measured, z_h can be solved by estimating z_p assuming a linear model, subtracting it from z_{h+p}. Specifically, the trend was modeled using a linear model:

$$z_p = H\theta + e \tag{3.20}$$

where H is the observation matrix, θ is the model parameters, and e is model error. The columns of H are the basis functions that are fit to the data. To avoid basis function bias, H was constructed as a set of Kronecker delta functions which are later regularized using a smoothing prior:

$$H_{ij} = \delta_{t_i,t_j} \tag{3.21}$$

where $\delta_{i,j}$ is the Kronecker delta function:

$$\delta_{i,j} = \begin{cases} 1 & \text{if } i = j, \\ 0 & \text{if } i \neq j \end{cases} \tag{3.22}$$

The optimal θ was found using a regularized least squares formulation with a smoothness prior:

$$\hat{\theta} = \arg\min_{\theta} \left\{ \underbrace{||H\theta - z_{h+p}||^2}_{\text{fit}} + \eta \underbrace{||D(H\theta)||^2}_{\text{smoothness}} \right\} \tag{3.23}$$

where D is a smoothness matrix and η is a regularization weighting parameter. We used the discrete approximation matrix of the second derivative for matrix D to model the signal smoothness. This is solved by taking the derivative with respect to the tuning parameters and setting it to 0:

$$\frac{1}{2}\frac{\partial}{\partial\theta}\left(||H\theta - z_{h+p}||^2 + \eta||D(H\theta)||^2\right) = 0 \tag{3.24}$$

$$(H)^T(H\theta - z_{h+p}) + \eta(DH)^T(D(H\theta)) = 0 \tag{3.25}$$

Factoring and rearranging yields:

$$\hat{\theta} = (H^T H + \eta^2 H^T D^T D H)^{-1} H^T z_{h+p} \tag{3.26}$$

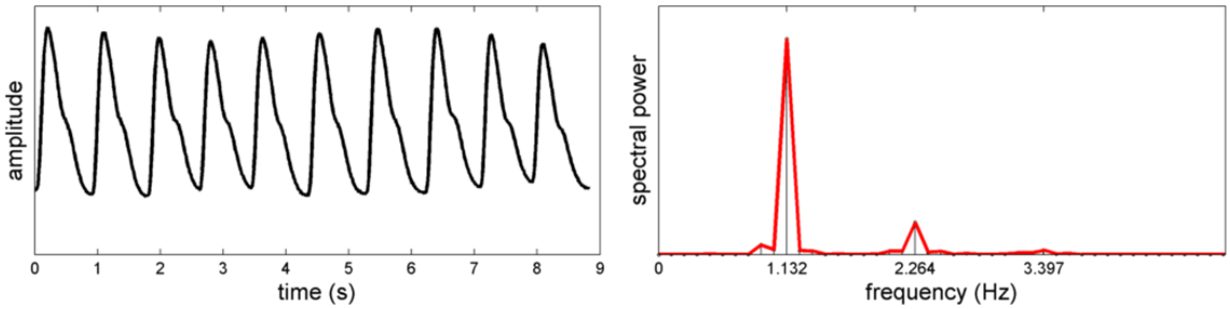

Figure 3.1: Quasi-periodic nature of a typical blood pulse waveform signal measured from the finger. The periodicity and dicrotic characteristics of the waveform result in predominantly harmonic frequencies in the power spectral density.

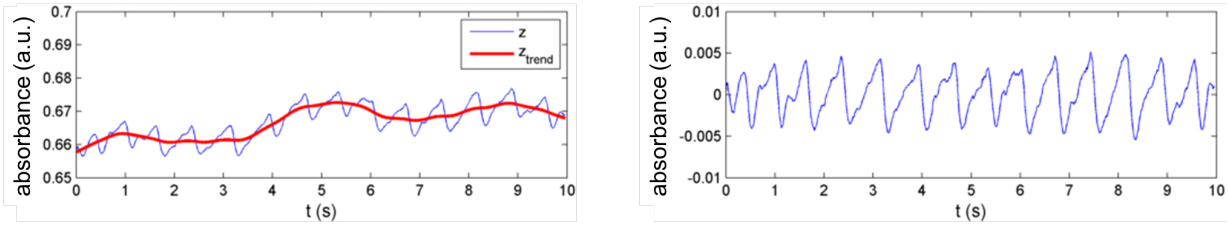

(a) Signal, estimated trend

(b) Signal, detrended

Figure 3.2: Example of the process noise removal process. A nonlinear trend was estimated in the original signal and subsequently removed, resulting in a stable signal.

The trend component of the signal can thus be reconstructed by substituting into Equation 3.20:

$$\hat{z}_p = H\hat{\theta} \tag{3.27}$$

Solving for z_h in Equation 3.19 yields our final hemodynamic signal estimate:

$$z_h = z_{h+p} - \hat{z}_p = (I - (H^T H + \eta^2 H^T D^T D H)^{-1} H^T) z_{h+p} \tag{3.28}$$

Figure 3.2 shows the recovery of a stable signal from a signal corrupted by movement using this detrending method. The trend is invariant to localized absorbance fluctuations from changes in blood volume, which makes up the true signal. It follows the general trend of the curve, and subtracts it from the measured signal, yielding a stable signal.

3.5 Spatial Pulsatility Analysis

Once the waveforms have been extracted, signal fidelity metrics must be used to assess the presence (and strength) of pulsatility at each location. Some locations may not exhibit pulsatility (e.g., hair, non-pulsatile tissue).

3.5.1 Supervised Signal Strength Metrics

Spectral signal-to-noise ratio (SNR) was used to quantify the frequency domain signal strength. The spectral magnitude of a reference signal (e.g., finger PPG) is regarded as the ground-truth frequency compositions. Due to the quasi-periodic nature of the blood pulse waveform, these waveforms often consist of a small set of frequencies with harmonics. Mathematically:

$$\mathrm{SNR}(\hat{z}, z) = 10 \log_{10} \left(\frac{\sum_f (\Gamma_f(z))^2}{\sum_f (\Gamma_f(z) - \Gamma_f(\hat{z}))^2} \right) \tag{3.29}$$

where f represents frequency index.

Pearson's linear correlation coefficient was used to quantify the temporal domain signal strength. Mathematically, given two signals z and $\hat{z}$ (e.g., true and estimated blood pulse waveform signals), the correlation coefficient was computed as:

$$r(\hat{z}, z) = \frac{\sigma_{\hat{z},z}}{\sigma_{\hat{z}} \sigma_z} \in [-1, 1] \tag{3.30}$$

where $\sigma_{\hat{z},z}$ is the covariance:

$$\sigma_{\hat{z},z} = \frac{1}{N-1} \sum_{i=1}^{N} (\hat{z}_i - \bar{\hat{z}})(z_i - \bar{z}) \tag{3.31}$$

and σ_x, σ_y are the standard deviations of the respective signals:

$$\sigma_x = \sqrt{\frac{1}{N-1} \sum_{i=1}^{N} (x_i - \bar{x})^2} \tag{3.32}$$

Note that although this formulation is analogous to the correlation coefficient used in regression, its underlying meaning here is different. Given two signals, r computes the matching strength of the two signals ignoring bias (offset) and dynamic range, which is particularly suitable for unitless absorbance measurements.

In some cases, the extracted and ground-truth signal may exhibit relative timing differences. For example, pulses will arrive at the next (extraction site) sooner than at the finger (ground-truth measurement site). In these situations, the success metric must account for relative temporal differences. The strength was computed using the maximum cross-correlation between the extracted signal $\hat{z}$ and the ground-truth signal z from the finger photoplethysmography cuff:

$$r_x(\hat{z}, z) = \max_{\Delta t} \left\{ \frac{\sigma_{z_t \hat{z}_{t+\Delta t}}}{\sigma_{z_t} \sigma_{\hat{z}_{t+\Delta t}}} \right\} \tag{3.33}$$

where $\sigma_{z_t \hat{z}_{t+\Delta t}}$ is the covariance between the true and (shifted) extracted signal, and $\sigma_{z_t}, \sigma_{\hat{z}_{t+\Delta t}}$ are the standard deviations of the true and (shifted) extracted signal respectively.

3.5.2 Unsupervised Signal Strength Metrics

Ideally, signal strength should be a function of the SNR of the estimated temporal signal, since this provides information about the signal fidelity. However, SNR computation requires knowing the true signal, which is unknown in some environments. A proxy metric for estimating SNR should thus be computed using prior knowledge of blood pulse waveform characteristics.

The primary physiological characteristic that was considered was the spectral distribution of strong hemodynamic signals. As was observed in Chapter 3.4, strong hemodynamic signals are comprised of a small set of frequencies, consisting primarily of the fundamental heart rate frequency and its harmonics. Thus, it can be hypothesized that non-pulsatile or weak signals are comprised of a larger set of frequencies. The signal strength metric should therefore quantify the compactness of the spectral distribution. Spectral entropy is well-suited for this problem. More generally speaking, entropy is a measure of randomness, or unpredictability. Systems that are characterized by large amount of randomness have high entropy. Entropy of a discrete probability distribution p is computed as:

$$H(p) = -\sum_{k=0}^{N-1} p_k \cdot \log p_k \tag{3.34}$$

where p is a probability distribution with N bins. Since this problem considers the set of signal frequencies, the normalized power spectral distribution can be modeled as the

distribution under investigation, giving rise to spectral entropy. Then, given an extracted signal z, normalized spectral entropy (H^*) was computed as:

$$H^*(\hat{z}) = \frac{-\sum_{k=0}^{N-1} \Gamma_k(\hat{z}) \cdot \log \Gamma_k(\hat{z}))}{\log N} \in [0, 1] \tag{3.35}$$

where $\Gamma(\hat{z})$ is the normalized spectral power for signal $\hat{z}$ according to Equation (3.13). Values closer to 0 signify a more compact power spectral distribution, and are thus considered stronger signals. The $\log N$ normalization is derived by considering the theoretical maximum entropy value for a signal of length N, which arises from the uniform spectral distribution of a completely random signal of length N:

$$H_{max}(p) = -\sum_{k=0}^{N-1} \frac{1}{N} \cdot \log\left(\frac{1}{N}\right) \tag{3.36}$$

$$= -\log\left(\frac{1}{N}\right) \tag{3.37}$$

$$= -\log\left(N^{-1}\right) \tag{3.38}$$

$$= \log N \tag{3.39}$$

3.6 Physical System

Based on the theoretical design presented above, a custom imaging system was designed and developed for collecting biophotonic hemodynamic data.

3.6.1 Design Rationale

The system was designed to maximize its portability and ability to evaluate various optical components easily. Figure 3.3 shows the system with all integrated components. It was designed with a solid chassis, incorporating a 1/4"-20 screw mount in the base for tripod mounting. Its modular design was divided into two primary components: the primary housing and the front optical housing unit. The front optical unit allowed up to eight individual illumination 1" optical components which were in the same plane as the camera lens (middle). This co-planar surface enabled parallel illumination projection, and the different illumination ports increased flexibility of illumination angle relative to the anatomy under consideration. The primary housing unit comprised the camera and mounting areas

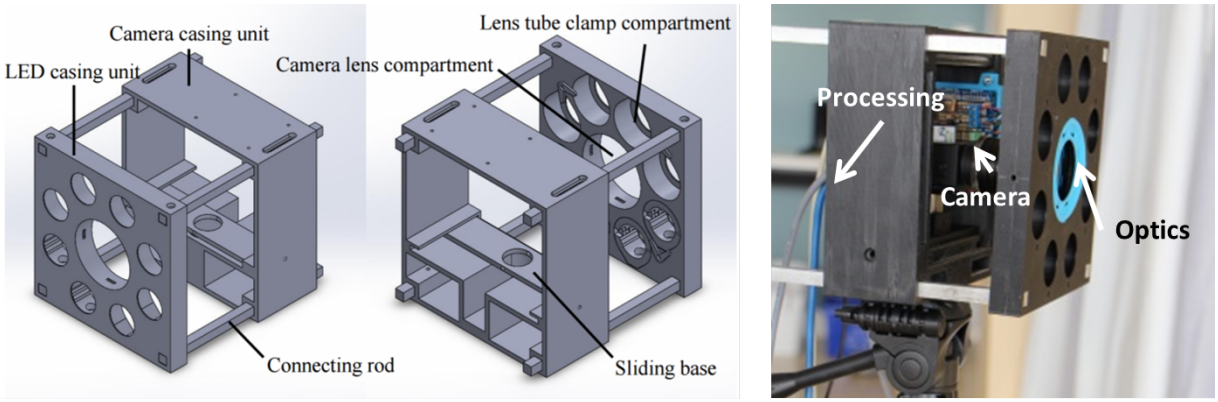

(a) 3D design (b) Physical system

Figure 3.3: 3D design and physical coded hemodynamic imaging system. The system houses the required optical components, electronic circuit boards, camera, and illumination system in a portable unit.

for electronic synchronization circuits. These units were attached using four corner rods, inspired by optical cage systems. The chassis was 3D printed using ABS plastic, which exhibited a good trade-off between durability and weight.

3.6.2 Instrumentation

A monochromatic camera with NIR sensitivity (Point Grey GS3-U3-41C6NIR) was selected to enable NIR illumination and sensing for increased depth of penetration. To capture deep tissue penetration using NIR wavelengths, and to minimize the effects of visible environmental illumination, an 800–1000 nm optical bandpass filter was mounted in front of the camera lens. Two illumination sources could be selected: high-powered light emitting diodes (LEDs) or incandescent broadband light sources, such as a tungsten-halogen light source. A 16 mm lens was used at a distance of 1.5 m, providing 0.5 mm/pix spatial resolution across a 1 m $\times$ 1 m field of view.

A high-powered NIR LED (850 nm center wavelength, 720 mW optical power) was chosen for deep tissue penetration. Figure 3.4 shows the LED relative spectral power curve, demonstrating the peak wavelength of 850 nm and spectral bandwidth of 18 nm. Light at this wavelength is situated on the oxyhemoglobin absorption side of the isosbestic point (see Figure 2.2), which was important since arterial pulsations are the transfer of oxygenated hemoglobin to target tissue beds. The LED radiant output was held stable

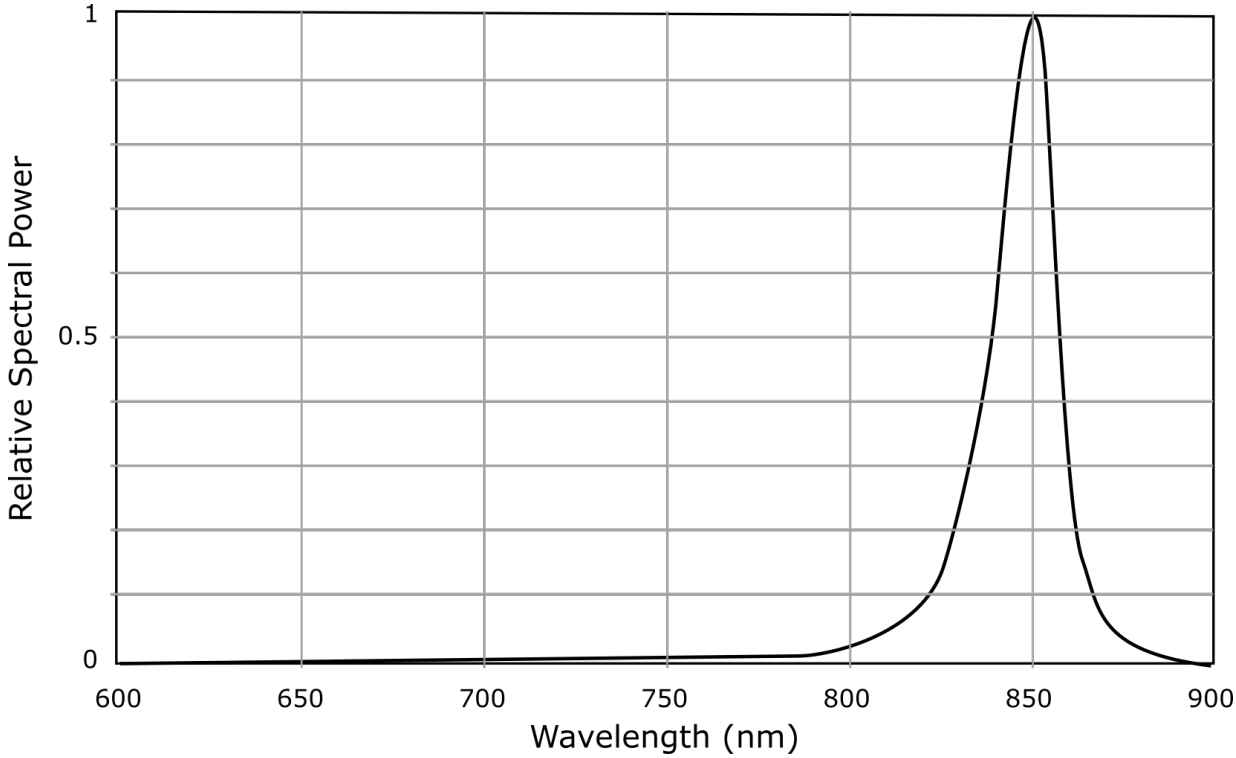

Figure 3.4: Relative spectral power of the high-power LED used in this thesis. The LED exhibited a peak wavelength of 850 nm with a full-width half maximum of 18 nm. From [52].

using a constant current driver (LM3414, Texas Instruments). Figure 3.5 demonstrates a stable LED output over time, yielding a variation of $\sigma = 0.07$ pixel intensity over 8-bit frames. LEDs allowed for relatively narrow spectral emission in a small form factor, whereas tungsten-halogen sources enabled very wide area illumination. In both cases, uniform spatial illumination coding was important for large area tissue monitoring. This "spatial code" was achieved through custom microlens array optics for the LEDs, and a 16" glass fabric diffuser for the tungsten-halogen source. In the scope of this thesis, data were collected at 60 fps with 16 ms exposure time. This frame rate provides sufficient sampling density across physiologically realistic heart rates, including bradycardia and tachycardia. For example, at the 60 fps sampling rate, heart rates of 40 bpm (bradycardia) and 150 bpm (tachycardia) would result in 85 and 18 sampled data points along the pulse respectively. Additionally, a typical 150 ms systolic climb results in 9 sampled data points, which is sufficient for reconstructing the waveform.

During experiments, the ground-truth blood pulse waveform was recorded using a finger

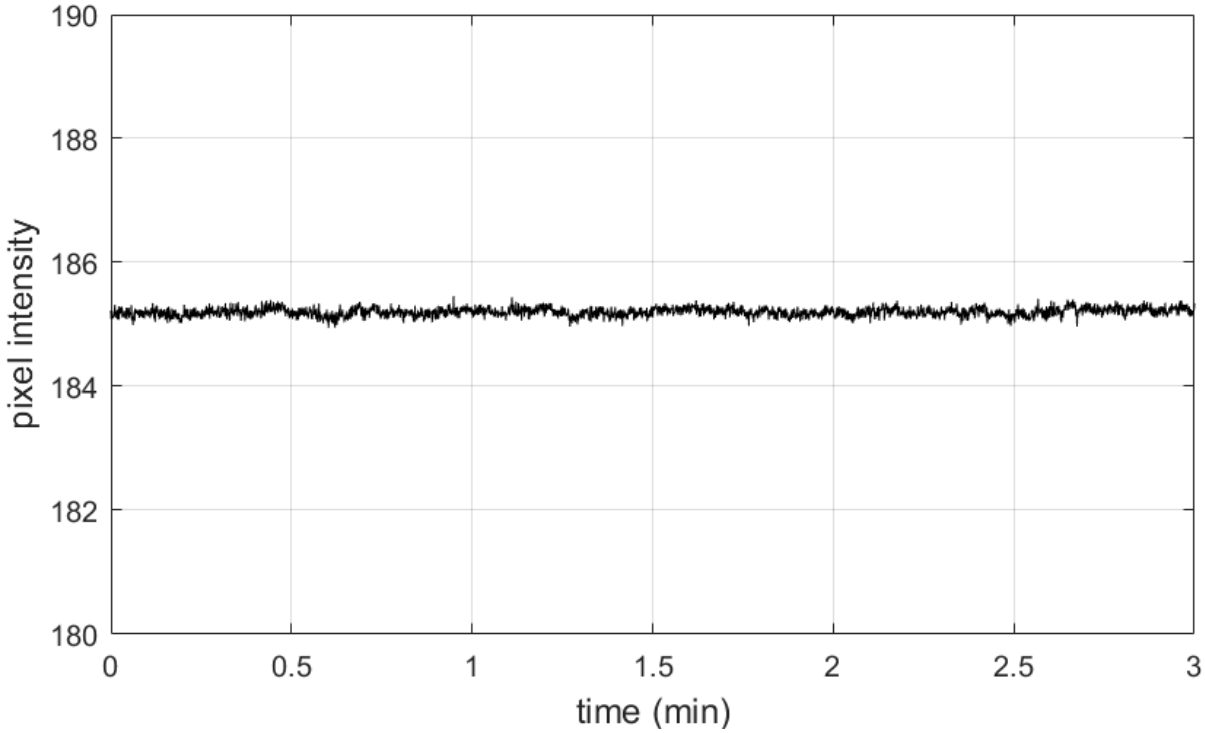

Figure 3.5: Plot demonstrating LED stability over time. Using a constant current driver, the LED radiant output is held stable ($\sigma = 0.07$ pix), thus providing stable incident illumination.

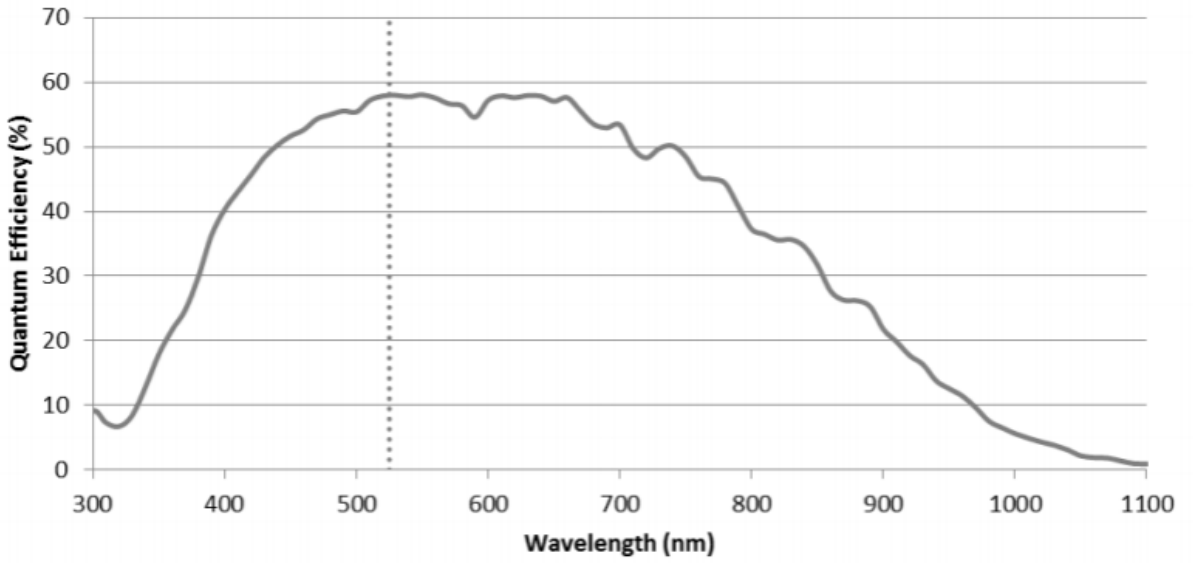

Figure 3.6: Camera quantum efficiency curve, showing strong near-infrared sensitivity, which enables deeper tissue penetration than visible light cameras. From [53].

photoplethysmography sensor. The output of this sensor was transmitted to the computer synchronously with the video data, enabling time-synchronized analysis of observed pulsatility.

3.7 Summary

This chapter presented the theoretical and practical elements for developing a novel wide-field computational biophotonic imaging system for spatiotemporal blood pulsatility analysis. The system design is theoretically grounded in a temporal Beer-Lambert light attenuation optical model for assessing local pulsatility across the camera's field of view. The system operates in the near infrared spectrum, which exhibits deeper tissue penetration than visible wavelengths, and has desirable hemoglobin absorption properties in addition to weak melanin absorption. A biomedical signal processing pipeline removes measurement and process noise, resulting in a stable robust blood pulse waveform signal. Supervised and unsupervised signal strength metrics were formulated, which will be used throughout the thesis for evaluating signal strength. Finally, the instrumentation used in practice was presented, which was used to collect the data presented in Chapter 4 and Chapter 5.

Chapter 4

Automatic Blood Pulse Waveform Extraction

4.1 Introduction

Automatic hemodynamic signal extraction is important for enabling cardiovascular assessment similar to that of photoplethysmography, which is widely used and adopted clinically [7]. The imaging system presented in Chapter 3 produces a set of frames where each pixel acts as a virtual hemodynamic sensor. However, these widefield frames consist of heterogeneous mixture of pixels (e.g., skin, hair, background, clothing, etc.). Locations on the body that contain pulsatile flow are not readily apparent. Identifying pixels representing the skin does not guarantee pulsatile blood flow, as some areas may be minimally vascularized, or may not contain pulsatile vessels. In fact, the pulsatile nature of the blood pulse waveform is not fully understood [27,54]. Thus, automatic signal extraction methods require careful design for obtaining clean signals.

Existing methods for automatic signal extraction broadly rely on a combination of spatial and spectral information. The RGB components in cameras with Bayer filters have been leveraged to identify the blood pulse waveform using independent component analysis [16, 41], Beer-Lambert modeling [19], and skin composition modeling [46]. However, these methods rely on measuring multispectral reflectance values such as RGB, which may not be appropriate in low-light settings such as sleep monitoring. Furthermore, the tissue penetration depth of incident illumination is wavelength- and tissue-dependent [20]. To solve this problem, some methods rely only on a single wavelength (or colour channel) to extract the signal through spatial analysis [13, 14, 43]. Regardless of the spectrum chosen,

existing methods average the pixel intensities over chosen areas, such as the facial bounding box [14, 16, 19], predefined facial areas [41, 55], and facial segmentation [43]. Methods relying on facial tracking may fail due to varying lighting conditions, different face-camera perspectives, or from various facial features. Some studies have recognized the importance of extending PPGI beyond heart rate analysis by analyzing heart rate variability as an indicator for cardiac function [16, 41, 55, 56], however these studies use pre-defined areas based on facial landmarks for extracting the blood pulse waveform, which may not generalize well to new systems or environmental settings (e.g., other anatomies, non-colour imaging systems, etc.). Some studies have focused on automatic region of interest (ROI) selection which identifies skin pixels for analysis for more robust signal extraction [16, 57, 58, 59]. However these methods rely on RGB colour information for computing ICA [16], chromaticity derivatives [57], and chrominance-based skin model [58, 59]. Furthermore, each pixel in the ROI are weighted the same, which may be inconsistent with the underlying physiology. Motivated by the increased performance from automatic region selection, there is a need for pulsatility identification that can be applied in settings where colour information is not available, such as low light settings (e.g., sleep studies).

Here, we present a spectral-spatial fusion method for extracting a blood pulse waveform from a set of frames from an arbitrary scene. Our goal was to extract signals that exhibited both spectral and temporal fidelity, to enable both spectral and temporal analysis. Using physiologically derived *a priori* spectral and spatial information related to blood pulse waveforms, our method learns which regions contain the strongest pulsatility based on their physiological relevance rather than their anatomical location, which enables signal extraction across different body types. Results across a 24-participant study show that the proposed method generated signals that exhibited significantly stronger temporal correlation and spectral entropy compared to existing methods. The framework was presented as a general framework that can be used to augment existing or new PPGI systems for assessing pulsatility in arbitrary anatomical locations.

4.2 Spectral-Spatial Fusion Model

The goal of the spectral-spatial fusion model was to extract a clean temporal blood pulse waveform signal from a scene. By emphasizing temporal fidelity, not only can summary metrics such as heart rate be computed, but important temporal fluctuations such as cardiac arrhythmias can be assessed. The scene is assumed to contain an unknown mixture of relevant regions (i.e., skin areas which exhibit pulsatility), and irrelevant regions (e.g., background, clothing, non-pulsatile skin regions, etc.). Given this mixture of regions (in-

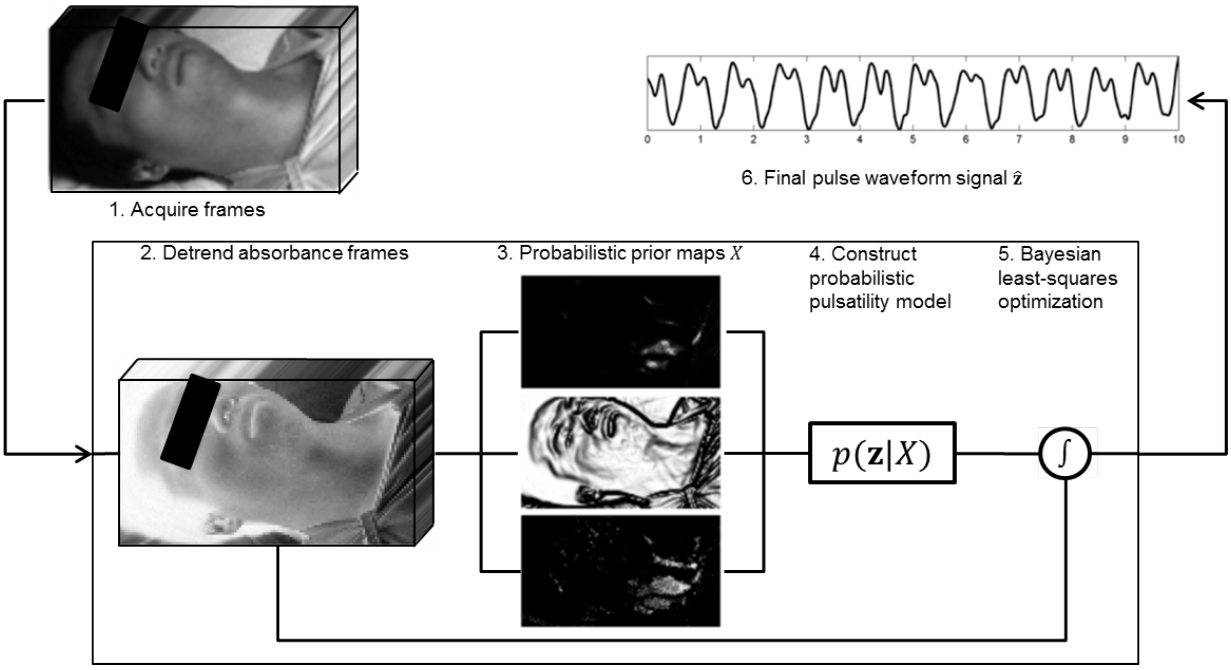

Figure 4.1: Processing pipeline of the proposed spectral-spatial signal extraction method. Acquired frames were converted from reflectance to absorbance and detrended. Spectral-spatial probabilistic prior maps were computed and used to model the posterior distribution representing the pulsatility model. Bayesian least-squares optimization was used to generate the blood pulse waveform signal.

put), the system must discover a temporal PPGI signal (output). Figure 4.1 provides a graphical overview of the system. Details are provided below.

4.2.1 Problem Formulation

Let z be the (unknown) true blood pulse waveform. Let $X = \{x_i \mid 1 \leq i \leq n\}$ be a set of absorbance signals, where:

$$x_i = \sum_{k=-\infty}^{\infty} a_i(t)\delta(t - kT) \tag{4.1}$$

where $a_i(t)$ is the absorption signal extracted from region l, δ is the Dirac delta function from Equation 3.17, and T is the sampling period. Here, following the Beer-Lambert law, absorbance $x_i(t)$ was calculated according to the signal processing framework presented in

Chapter 3.4. Given the set of measurements X, which is a mixture of signals from a scene that are both relevant (e.g., skin) and irrelevant (e.g., background, clothing, hair), the goal is to estimate the "true" blood pulse signal using an intelligently weighted subset of regions that contain pulsatility. This inverse problem can be formulated as a Bayesian problem, where prior physiology knowledge can be injected into the model to educate assumptions about the state (specific priors will be discussed in the following section). Mathematically, it can be solved using the Bayesian least squares formulation [60]:

$$\hat{z} = \arg\min_{\hat{z}} \left\{ E\left[(\hat{z} - z)^T (\hat{z} - z) \mid X \right] \right\} \tag{4.2}$$

$$= \arg\min_{\hat{z}} \int (\hat{z} - z)^T (\hat{z} - z) p(z|X) dz \tag{4.3}$$

where $p(z|X)$ is the posterior distribution of state signal z given the measurements X. The optimal solution is found by setting $\partial / \partial \hat{z} = 0$:

$$\frac{\partial}{\partial \hat{z}} \int (\hat{z} - z)^T (\hat{z} - z) p(z|X) dz = 0 \tag{4.4}$$

Simplifying:

$$2 \int (\hat{z} - z) p(z|X) dz = 0 \tag{4.5}$$

$$\int \hat{z} p(z|X) dz - \int z p(z|X) dz = 0 \tag{4.6}$$

$$\hat{z} = \int z p(z|X) dz \tag{4.7}$$

Thus, to solve this equation, the unknown posterior distribution $p(z|X)$ must be modeled. This distribution represents the probability that a state signal z represents the true blood pulse waveform given the observed temporal signals X. The posterior distribution can be modeled as a novel probabilistic pulsatility model, which we approximated using a discrete weighted histogram of the observed states [61]:

$$\hat{p}(z|X) = \frac{\sum_{i=1}^{|X|} W_i \delta(|z - x_i|)}{Y} \tag{4.8}$$

where Y is a normalization term such that $\sum_k \hat{p}(z_k|X) = 1$. The problem then becomes computing the probabilistic prior W_i for each observed signal x_i to determine how well it represents the true blood pulse waveform. The following subsections propose a solution using a spectral-spatial model motivated by blood pulse waveform characteristics and vascular physiology.

4.2.2 Probabilistic Pulsatility Model

Ideally, $p(z|X)$ should be a function of the SNR of the estimated temporal signal, since this provides information about the signal fidelity. However, SNR requires knowing the true signal, which is unknown at the time of acquisition. A proxy metric for estimating SNR should thus be computed using prior knowledge of blood pulse waveform characteristics. A spectral-spatial model is proposed based on the following two observations, which can be leveraged as prior information in the Bayesian framework presented above:

- **Spectral:** Clean blood pulse waveforms are quasi-periodic, and are primarily composed of a weighted sum of a small set of sinusoidal signals (see Chapter 3.4).
- **Spatial:** Non-homogeneous skin areas exhibit high variability due to anatomical non-uniformity (e.g., boundary, skin fold, hair).

For motivation, refer back to Figure 3.1, which shows a typical power spectral density of a clean blood pulse waveform. The spectral energy is compact, and is primarily composed of two harmonic frequencies. This indicates the quasi-periodic nature of the blood pulse waveform, and provides rationale for the spectral model.

In order to compute spectral properties, the normalized 0-DC spectral power distribution for spatial region i was computed using Equation 3.16, denoted $\Gamma_f^*(z_i)$. The normalized spectral power (i.e., $\int \Gamma_f^*(z_i)df = 1$) was used to model the relative AC pulsatile amplitude in the unit-less blood pulse waveforms.

The quasi-periodic blood pulse waveform is dominated by the fundamental frequency corresponding to the heart rate and the first harmonic (see Fig. 3.1). To quantify this property, the spectral power exhibited by the fundamental frequency and first harmonic was computed:

$$h_i = \int_{f^*-\Delta f}^{f^*+\Delta f} \Gamma_f^*(z_i)df + \int_{2f^*-\Delta f}^{2f^*+\Delta f} \Gamma_f^*(z_i)df \tag{4.9}$$

where $f^* = \arg\max_f \Gamma_i(f)$, and Δf is the spectral window's half-width. We used $\Delta f = 0.2$ Hz. h_i was set to 0 for signals whose fundamental frequency was outside of the physiologically realistic heart rate range. The final "harmonic prior" was computed as:

$$w_i^{\text{harm}} = \exp\left(\frac{-(1-h_i)^2}{\alpha_h}\right) \tag{4.10}$$

where α_h is a tuning parameter. An inverse exponential was used to emphasize small values of $(1-h_i)$ (i.e., strong harmonic contributions).

To quantify noise exhibited by the quasi-periodic waveform, the maximum spectral power response outside of the fundamental heart rate range was found:

$$q_i = \max_f \left\{ \int_{f-\Delta f}^{f+\Delta f} \Gamma_f^*(z_i) df \mid f \not\subset \{f^*, 2f^*\} \right\} \tag{4.11}$$

The final "noise prior" was computed as:

$$w_i^{\text{noise}} = \exp\left(\frac{-q_i^2}{\alpha_q}\right) \tag{4.12}$$

where α_q is a tuning parameter. An inverse exponential model was used to emphasize small values of q_i (i.e., low noise).

Local anatomical variations may corrupt any pulsatile signals exhibited by underlying vessels (e.g., hair, skin fold, shadow ridge), or may not contain a pulsatile components at all (e.g., clothing, naris, eyelid). In order to estimate the anatomical uniformity at a given location, the image gradient was computed. In particular, given an image scene Λ whose individual regions are x_i, the "spatial prior" was computed as:

$$w_i^{\text{spat}} = \exp\left(\frac{-\nabla\Lambda^2}{\alpha_l}\right) \tag{4.13}$$

where $\nabla\Lambda$ is the gradient of image Λ. An inverse exponential model was used to emphasize small values of $\nabla\Lambda$ (i.e., homogenous areas).

The individual priors for region i were combined to form the final region spectral-spatial probabilistic prior:

$$W_i = \min\left\{ \prod_k w_{ik} \mid N_i \right\} \tag{4.14}$$

where $w_i = \{w_i^{\text{harm}}, w_i^{\text{noise}}, w_i^{\text{spat}}\}$, and N_i is the neighborhood around region i. Here, a regional first order statistic constraint was imposed on the priors in order to further enforce spatial cohesion. Substituting this into Eq. (4.8) produces the estimate of the posterior distribution $\hat{p}(z|X)$.

4.3 Experimental Results

4.3.1 Data Collection

Demographic information (age, height, weight, body fat %) was obtained at the beginning of the study. Table 4.1 provides a summary of the sample demographics measured using

Table 4.1: Sample demographics

Demographic	Sample Representation
n (male/female)	24 (13/11)
age (years)	9 – 60 (28.7 ± 12.4)*
mass (kg)	39.0 – 107.0 (72.0 ± 18.8)*
height (cm)	135 – 193 (167.1 ± 13.1)*
body fat (%)	10.5 – 42.3 (21.0 ± 7.9)*
muscle (%)	31.0 – 53.9 (40.4 ± 5.3)*
BMI ($\text{kg}\cdot\text{m}^{-2}$)	16.4 – 35.1 (25.5 ± 5.2)*

*$\mu \pm \sigma$

bioelectrical impedance analysis. Data were collected across 24 participants of varying age (9–60 years, $(\mu \pm \sigma) = 28.7 \pm 12.4$) and body compositions (fat% 21.0 ± 7.9, muscle% 40.4 ± 5.3, BMI 25.5 ± 5.2 $\text{kg}\cdot\text{m}^{-2}$). Participants assumed a supine position throughout the study, eliminating large motion variations. Data were collected using the hemodynamic imaging system presented in Chapter 3 at a distance of 1.5 m. The frames were downsampled such that each pixel represented 3×3 mm (6×6 pix) individual tissue regions. The ground truth PPG waveform was synchronously recorded using a photoplethysmography finger cuff [62].

We compared our method, henceforth called **FusionPPG**, with DistancePPG [43] and "FaceMeanPPG", where the face is tracked and the signal is extracted through framewise spatial averaging. This method is commonly used in similar studies [14,16,41]. Many pulse extraction methods rely on processing individual colour channels [16, 19, 41, 45], and were therefore infeasible for this study (and infeasible in low-light settings, such as sleep studies). For our implementation of FaceMeanPPG, we spatially averaged the area identified by Viola-Jones face tracker [16]. Though DistancePPG was evaluated using a green LED in its original form [43], the methods generalize to any single-channel imaging system, and thus could be used in this NIR monochrome setup. In its original implementation, DistancePPG requires estimating the true heart rate based on an averaging approach similar to FaceMeanPPG [43]. To generate optimal results of the comparison algorithm, DistancePPG was provided with the ground-truth heart rate (rather than their estimation method, which was found to fail in some cases). Since the participants exhibited minimal movement, the frames were inherently temporally co-aligned, and thus tracking was disabled for FaceMeanPPG and DistancePPG.

In order to evaluate and compare signal fidelity between methods, normalized spectral entropy ($H(\hat{z})$, Equation 3.34)) and Pearson's linear correlation coefficient ($r(\hat{z}, y)$, Equa-

tion 3.30) were computed for each extracted signal (see Chapter 3.5). To account for pulse time differences between the neck/head and finger, the maximum forward-sliding cross-correlation value within a short temporal window was used according to Equation 3.33. Using these two signal metrics, two-sample t-test (MATLAB R2016b, Mathworks) was used to test the null hypothesis that the signals extracted from **FusionPPG** and the comparison methods come from samples with equal means.

The heart rate of a blood pulse waveform signal was computed in the temporal domain using an autocorrelation scheme for increased temporal resolution [63]. Specifically, each waveform was resampled at 200 Hz using cubic spline interpolation, and autocorrelation peaks were detected and used to estimate heart rate:

$$\widehat{HR} = 60\frac{F_s}{\Delta t} \tag{4.15}$$

where F_s is the sampling rate, and Δt is the time shift yielding peak autocorrelation response. Hyperparameter optimization was performed to find optimal tuning parameters $\{\alpha_h, \alpha_q, \alpha_l\}$ using a grid search method with the following performance metric:

$$\frac{\sum_{k\in\eta}\hat{Z}_k}{1-\sum_{k\in\eta}\hat{Z}_k} \tag{4.16}$$

where $\hat{Z}_k$ is the k^{th} Fourier coefficient of the estimated signal $\hat{z}$, and η is the set of coefficients pertaining to the fundamental frequency and first harmonic of the $\hat{z}$. An exponential grid search was performed over the space $\alpha \in [10^{-2}, 10]$, which when substituted into the weight term $\exp(-x^2/\alpha)$ effectively changes the width of the inverse exponential, representing the space of hyperparameters from strong weight bias (small width) to weak weight bias (large width). When choosing the optimal hyperparameters, signals exhibiting physiologically unrealistic heart rates were excluded.

One participant's data were removed due to erroneous ground-truth waveform readings. The study was approved by a University of Waterloo Research Ethics committee and performed in accordance with the Declaration of Helsinki.

4.3.2 Data Analysis

Figure 4.2 shows the signals extracted using the proposed fusion method compared to the ground-truth finger waveform. The waveforms exhibited high temporal fidelity, and were highly correlated to the ground-truth waveforms. Some participants exhibited temporally

offset signals relative to the ground-truth PPG since the measured area (head) is closer to the source (heart) than the PPG (finger). Furthermore, vascular resistance may be affected by vasodilatory responses to ambient conditions such as temperature [64], thus affecting the pulse arrival time. The foot of each blood pulse waveform can be observed, signifying the precise time of the start of ventricular contraction. Signal extraction failed on one participant due to high fat content (42.3%, Figure 4.2 row 9 column 2).

FusionPPG outperformed both comparison methods on the sample dataset. Figure 4.3 compares the box plot of the proposed and comparison methods using correlation (higher is better) and normalized spectral entropy (lower is better). FusionPPG attained statistically significantly higher correlation to the ground-truth waveform than FaceMeanPPG ($p < 0.001$) and DistancePPG ($p < 0.001$), signifying signals with higher temporal fidelity. FusionPPG also attained statistically significantly lower normalized spectral entropy than FaceMeanPPG ($p < 0.001$) and DistancePPG ($p < 0.001$), signifying more compact frequency components, consistent with the quasi-periodic nature of a true blood pulse waveform. DistancePPG attained higher correlation and lower entropy than FaceMeanPPG, consistent with previous findings [43].

FusionPPG was able to precisely estimate heart rate from the extracted waveforms. Figure 4.4 shows the correlation and Bland-Altman plots showing FusionPPG's ability to extract precise and accurate heart rate. The predicted heart rates were highly correlated to the ground-truth heart rate ($r^2 = 0.9952$), and were in tight agreement, with low mean error ($\mu = -1.0$ bpm) and low variance ($\sigma = 0.70$ bpm). The data were well represented within two standard deviations from the mean. The outlier was omitted from this analysis due to failed signal extraction.

Figure 4.5 compares the extracted waveforms from four participants using the three methods to the ground-truth waveform. The strongest waveforms (i.e., highest correlation) from DistancePPG, FaceMeanPPG, and FusionPPG were shown. An important characteristic is the foot of the waveform, which signifies the pulse arrival time. This foot was observed in each case, whereas it was not easily discernible in either DistancePPG or FaceMeanPPG due to the effects of averaging, resulting perhaps in a strong fundamental frequency which can predict heart rate, but is affected by spurious irrelevant frequencies that corrupt the waveform shape.

Figure 4.5(d) shows a participant that experienced a cardiac arrhythmia. An irregular cardiac contraction was observed at $t = 6$ s, resulting in a delayed contraction. Such cases cannot be easily observed using standard heart rate analysis in the frequency domain. However, the irregular heartbeat and delayed follow-up contraction was observed in FusionPPG's waveform, whereas it was not readily apparent in FaceMeanPPG or Dis-

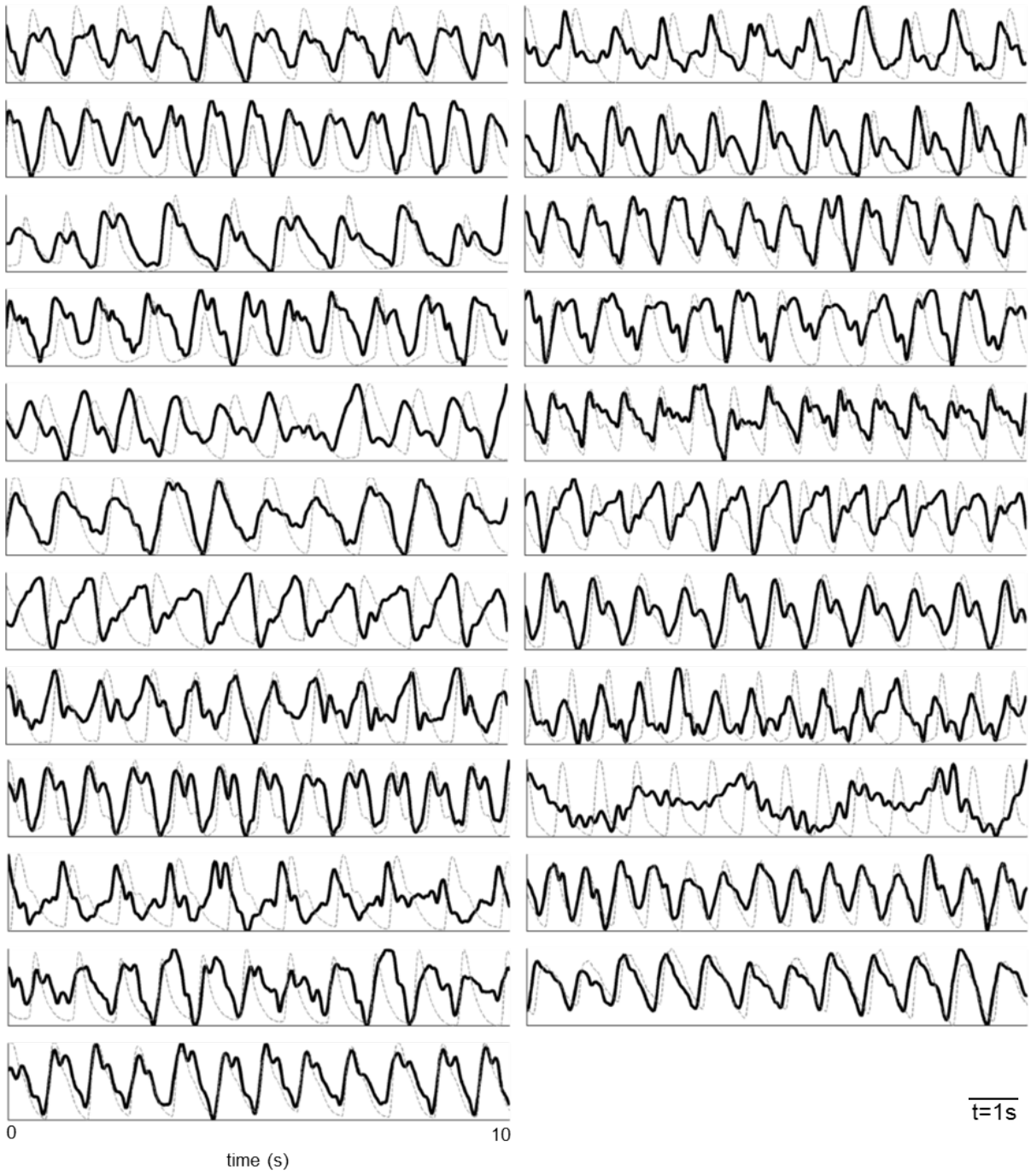

Figure 4.2: Signals extracted from all 23 participants using the proposed FusionPPG method (black), plotted against to the ground-truth FingerPPG waveform (gray, dotted).

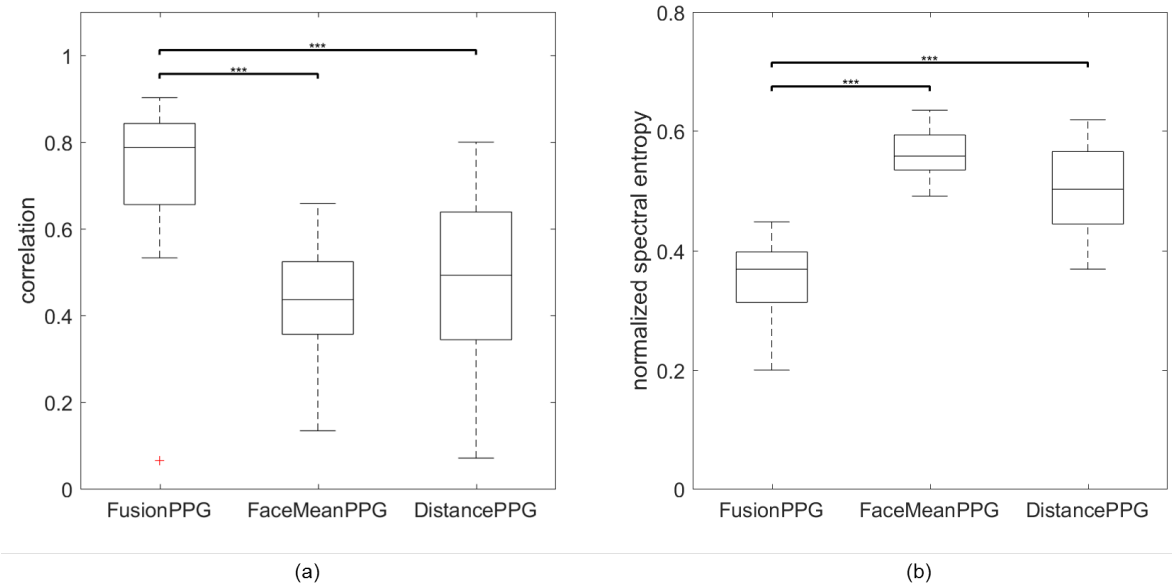

Figure 4.3: Box plot comparison of the correlation (a) and normalized spectral entropy (b) between the signals extracted using the proposed (FusionPPG) and the two comparison (FaceMeanPPG, DistancePPG) methods. FusionPPG exhibited significantly higher correlation and significantly lower spectral entropy (i.e., higher spectral compactness) compared to FaceMeanPPG and DistancePPG. (***statistically significant difference, $p < 0.001$)

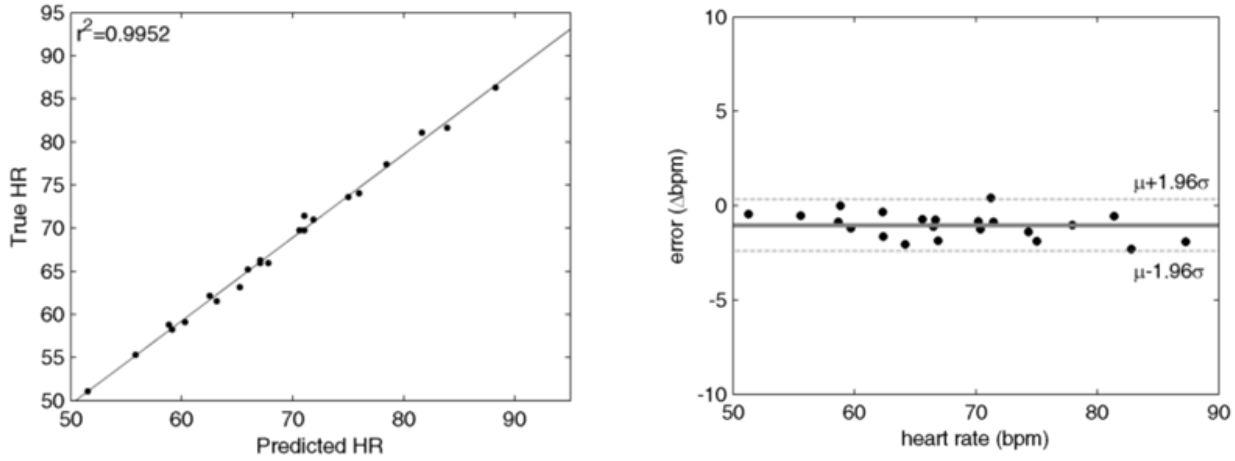

Figure 4.4: Correlation and Bland-Altman plots of the predicted heart rates using the extracted blood pulse waveform signal. The predicted heart rates were highly correlated to the ground-truth heart rate ($r^2 = 0.9952$), and were in tight agreement ($\mu = -1.0$ bpm, $\sigma = 0.70$ bpm). The outlier was omitted due to failed signal extraction.

tancePPG. This demonstrates the important of temporal signal fidelity to assess irregular cardiac events that deviate from typical waveforms.

4.4 Discussion

In this study, the most pulsatile areas were often found in the neck region. Figure 4.6 shows a typical computed pulsatility distribution overlaid onto the original frame, showing strong pulsing in the neck. The neck contains important vascular pathways, including the carotid arteries, which are major vessels that are closely connected to the heart and are close to the surface compared to other major arteries in the body. Pulsatile information in the face is more subdued, since the small arteries and arterioles are found further down the vascular tree. Thus, many existing methods that extract signals from the face may be at a disadvantage, and miss the rich information present in the neck.

The extraction method failed on the participant who had the highest fat % of the sample. Skin folds and thick tissue layers contributed to the inability to extract a signal with any of the three methods evaluated in this study. Many existing studies do not provide participant body composition, which is an important parameter when assessing signal strength. In the future, a more comprehensive dataset may elucidate stratified

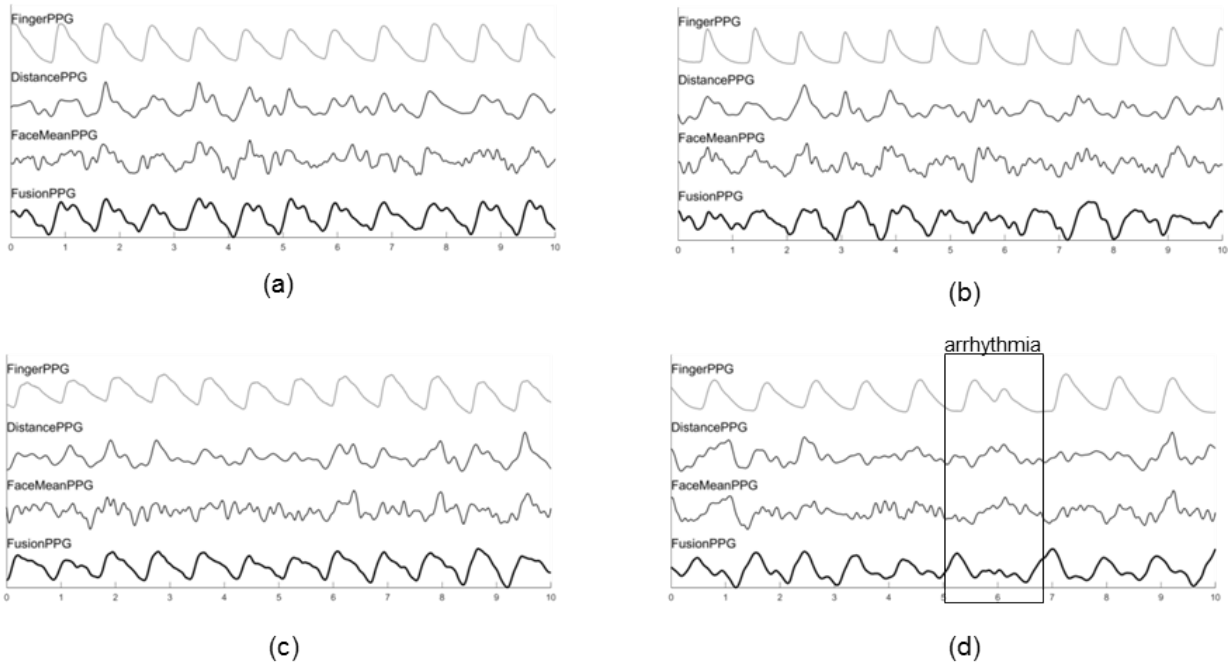

Figure 4.5: Extracted waveforms from the proposed and comparison methods across four participants. The selected waveforms were those that exhibited the strongest correlation from DistancePPG (a), FaceMeanPPG (b), FusionPPG (c), and a participant with arrhythmia (d). FusionPPG was able to extract strong waveforms across all participants, enabling the visual assessment of a cardiac arrhythmia (at $t = 6$ s).

Figure 4.6: Typical pulsatility distribution based on spectral-spatial fusion. An original frame (a) is used to compute and overlay the probabilistic pulsatility distribution (b). The strongest pulsing was often observed in the neck region, contributing strongly to the blood pulse waveform extraction.

correlation information based on demographic information such as age, gender and body composition. Furthermore, simulated flow phantoms may be developed with synthetic pulsatile arteries to elucidate the signal mechanisms in a controlled setting.

Traditional heart rate variability is assessed through the RR peak intervals using an electrocardiogram. However, similar timing differences can be observed and quantified using the blood pulse waveform. An important part of this waveform is the blood pulse foot, which is the minimum point just prior to inflection due to the oncoming blood pulse. The blood pulse is ejected from the heart due to left ventricular contraction, which is directly controlled by the electrical signals governing the heart mechanics. The timing difference between the ECG's R peak and the PPG's foot is the pulse transit time. Thus, timing differences between the blood pulse feet indicate timing differences in the heart [65]. An important characteristic that is not often discussed in PPGI studies is its ability to extract and assess abnormal waveforms (e.g., arrhythmia). In order to be useful as a health monitoring system, a PPGI system must not directly or indirectly assume normal waveforms. This was apparent in the arrhythmia case (Figure 4.5(d)), where FusionPPG's waveform was able to temporally convey an abnormal cardiac event. During validation, emphasis should be placed on detected abnormal as well as normal waveforms.

Many existing methods, including DistancePPG and FaceMeanPPG, require tracking and/or segmenting the individual's face. However, it may be beneficial to assess pulsatility in areas other than the face (e.g., arm, hand, leg, foot). These methods will fail at this

task since no face will be detected. In contrast, FusionPPG does not make any *a priori* assumptions about anatomical locations, and may therefore be used to assess pulsatility at other anatomical locations in future work.

Colour-based methods exist for automated region selection [57, 58, 59], which show increased accuracy when selecting image regions in an informed manner. The proposed method provides several advantages over these colour-based methods. First, FusionPPG does not rely on multispectral colour data acquisition, which may be problematic in low-light environment, imaging in high melanin density tissues [43], and imaging systems that use near infrared illumination sources for increased photon depth of penetration (e.g., for deep arterial analysis) [66]. Second, FusionPPG does not assume a cohesive region of interest. By treating each location as quasi-independent, anatomically irrelevant areas (e.g., hair, shadows) are excluded. Third, FusionPPG does not require skin tone calibration or prediction. Near infrared light is particularly suitable for analysis of various skin tones due to the decreased melanin absorption at these wavelengths [28]. Though visible light exhibits higher absorption in the visible than near infrared spectrum, one must also consider the effect of scatter and reduced absorption on photon attenuation. Primarily forward scattering photons that do not become attenuated before emitting from the tissue enable deeper tissue analysis [28] where major arteries reside. Though the fundamental nature of the PPG signal is still unknown [7, 27], deeper probing and physiological prior models increase the probability of hemodynamic-induced signal fluctuations rather than motion.

4.5 Summary

In this chapter, we presented a probabilistic framework for automatically extracting a blood pulse waveform signal from a series of frames. This probabilistic framework incorporated physiological priors for assessing signal fidelity on a pixel-by-pixel basis. This type of method is important for cardiovascular assessment and cross-compatibility with traditional single-point photoplethysmography sensors, and will be used in subsequent sections for assessing cardiovascular information such as cardiac arrhythmias.

Chapter 5

Applications

Chapter 3 and Chapter 4 presented novel methods for hemodynamic imaging and automatic blood pulse waveform extraction. These methods were designed to provide widefield hemodynamic assessment for cardiovascular monitoring. This chapter investigates hemodynamic imaging for three biomedical applications. Chapter 5.1 investigates spatial pulsatility across a participant sample with highly varying demographics to develop a spatial pulsatility model. Chapter 5.2 investigates the use of hemodynamic imaging for assessing the jugular venous pulse waveform, an important biomarker for cardiac function. Chapter 5.3 investigates the use of hemodynamic imaging for non-contact arrhythmia detection using time-frequency domain processing for identifying temporal anomalies in the blood pulse waveform signal.

5.1 Spatial Pulsatility Analysis

5.1.1 Introduction

Existing contact-based PPG systems are limited to single-location monitoring (e.g., finger), and are unable to provide widefield tissue perfusion assessment. PPGI systems allow for whole area monitoring, however, many existing systems use spatial pixel intensity averaging across large tissue regions to estimate cardiovascular perfusion, such as averaging over the facial bounding box [14, 16, 17] and hardcoded anatomical regions such as the forehead and cheeks [18, 41, 42]. One study attained increased accuracy by incorporating spatial pulsatility priors [43]; however, the method relies on a real-time estimate of the

true physiological state based on aforementioned coarse averaging techniques to achieve accurate prediction.

Here, we developed a continuous probabilistic pulsatility model for importance-weighted blood pulse waveform extraction. The continuous model can be used by PPGI systems of any resolution through appropriate sampling to extract robust blood pulse waveforms. The model was developed using a data-driven approach over a 23 participant sample with highly varying characteristics (11/13 female/male, age 9–60 years, body fat 10.5–42.3%, muscle 31.0–53.9%, BMI 16.4–35.1 $\text{kg}\cdot\text{m}^{-2}$). Using blood pulse waveform spatial correlation priors, an importance weighting scheme was developed which assigned locations with consistently strong pulsatility a higher weight. Samples were aligned and aggregated in a common Cartesian space, and the continuous probabilistic pulsatility model was computed using a kernel density estimation approach. This method was compared against whole-area uniform spatial averaging approach used by existing studies [14, 16, 17]. Results showed that signals extracted using the pulsatility model were statistically significantly stronger in temporal (correlation, $p < 0.01$) and spectral (SNR, $p < 0.01$) characteristics than uniform averaging, and heart rates were in tight agreement with ground-truth measurements ($r^2 = 0.9619$, error $\mu = 0.52$ bpm, $\sigma = 1.7$ bpm). Model visualization elucidated important arterial pathways, including the neck, malar regions, glabella regions, lips and nose.

5.1.2 Methods: Probabilistic Pulsatility Model

The goal was to compute a continuous probabilistic spatial pulsatility model for use as *a priori* information in PPGI systems. By computing a continuous model, it can be used by datasets different resolutions through appropriate discrete spatial sampling. Figure 5.1 depicts the processing pipeline to generate this pulsatility model. This study was approved by a Research Ethics Committee at the University of Waterloo and performed in accordance with the Declaration of Helsinki. Informed consent was obtained from all participants prior to data collection.

Different spatial locations exhibit varying amounts of observed pulsatility. For example, a skin location directly above a superficial artery will exhibit high pulsatility due to transient changes in local tissue optical properties from the arterial pulse [7, 27], whereas occluding hair will inhibit the observed pulsatility. Let $p(x, y)$ be the probabilistic pulsatility model such that $p(x, y)$ quantifies the probability of observing arterial pulsatility at location (x, y). Using a physiologically-motivated data-driven approach, $p(x, y)$ can be computed by determining the locations that consistently exhibited pulsatility across a diverse sample of participants (see Table 4.1). Such a model can be used as an *a priori* model for new data when extracting cardiovascular properties.

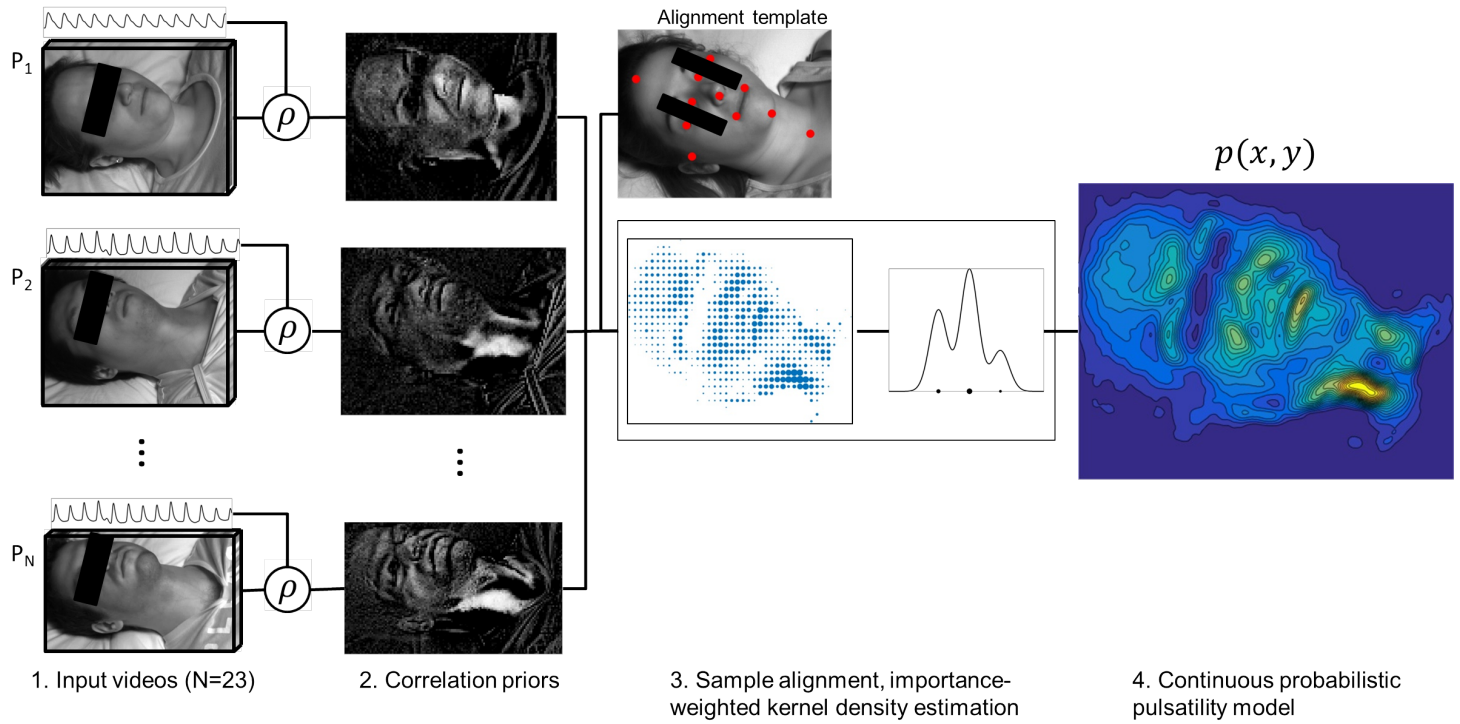

Figure 5.1: Processing pipeline to derive the continuous probabilistic pulsatility model. Videos of 23 participants were recorded using coded hemodynamic imaging synchronously with the ground-truth waveform (1). Correlation priors were computed by comparing pixelwise temporal signals against the ground-truth signal using Pearson's linear correlation coefficient (ρ) (2). The correlation prior maps were aligned relative to a template and projected into a 2-D Cartesian space, and spatially aggregated (3). A 2-D kernel density estimation method was used in this space (4) to generate the data-driven continuous probabilistic pulsatility model (5).

Correlation priors

Given a series of frames, denoised absorbance frames $a(x, y, t)$ were computed using the framework presented in Chapter 3. A transformation T was sought to map the set of absorbance frames $a(x, y, t)$ to a pulsatility strength map $C(x, y)$ describing pixelwise pulsatile components:

$$C(x, y) = T(a(x, y, t)) \tag{5.1}$$

Rather than estimating the pulsatility based on heuristic information, which is participant-independent and may introduce uncontrolled sources of noise, this model can be augmented by incorporating prior information directly into the transformation:

$$C(x, y) = T(a(x, y, t) \mid z) \tag{5.2}$$

where z is the ground-truth blood pulse waveform. This was measured synchronously with the frames, and Pearson's linear correlation coefficient was computed between the ground-truth signal and each pixel's temporal signal:

$$T(a(x, y, t) \mid z) = \frac{\sigma_{az}}{\sigma_a \sigma_z} \tag{5.3}$$

where σ_{az} is the covariance between the pixel and ground-truth signals, σ_a, σ_z are the standard deviations of the pixel and ground-truth signal respectively. This computation is scale- and offset-independent, suitable for capturing the ratio nature of the blood pulse waveform.

Importance-weighted kernel density estimation

A physiologically-derived importance-weighted scheme was developed to quantify the spatial pulsatility strength. An anatomical location that exhibited strong pulsatility contributed a larger weight than those that contained weak or no pulsing. This system allows for continuous kernel-based probabilistic pulsatility density estimation later. The importance map for participant i was computed as:

$$V_i(x, y) = \max\{C_i(x, y), 0\} \tag{5.4}$$

To infer pulsatility patterns across the whole sample, the primary anatomical locations must be co-aligned. The camera was systematically and consistently setup for all participants, however, differences in anatomy, minor rotation (relative to the camera) and

translation (relative to the frame region) were observed. To correct for these relative distortions, the problem was posed as a coordinate mapping problem, where each participant's weight data $V_i(x, y)$ were projected into the co-aligned pulsatility space $V(x', y')$. Mathematically:

$$\begin{bmatrix} x' \\ y' \end{bmatrix} = H_i \left(\begin{bmatrix} x \\ y \end{bmatrix} \right) \tag{5.5}$$

where H_i is a coordinate mapping function that maps (x, y) from participant space V_i to (x', y') in the co-aligned space V. Note that this transformation projects points directly into a Cartesian space. There is no need for interpolation, which may otherwise cause local inaccuracies. Implementation details of H_i are discussed later (Section 5.1.3). This aggregate co-aligned pulsatility space, $V(x', y')$, was populated with weighted points from each participant:

$$V(x_k, y_k) = \text{median}_i\{V_i(x_{ik}, y_{ik})\} \tag{5.6}$$

where (x_{ik}, y_{ik}) are the coordinates in the participant space that project to (x_k, y_k) in the aggregate space according to the mapping function H_i.

A resolution-agnostic model can be computed by estimating a continuous probability density function, and sampling this density function according to the given system's resolution. A modified Parzen-Rosenblatt kernel density estimation method [67, 68] was used to estimate the continuous pulsatility probability density function:

$$p(x, y) = \frac{1}{|V|} \sum_{k=1}^{n} \frac{V(x_k, y_k)}{w^2} \Phi \left(\frac{v - v_k}{w} \right) \tag{5.7}$$

where n is the total number of points, w is the spatial window width, $v = (x, y)$, Φ is the window kernel, and $|V|$ is a normalization term such that $\int_x \int_y p(x, y) dy dx = 0$. The kernel was scaled according to the datum's pulsatility weight $V(x_k, y_k)$. Using the 2-D Gaussian kernel:

$$\Phi(u) = \frac{1}{2\pi} \exp \left(-\frac{u^T u}{2} \right) \tag{5.8}$$

the final probabilistic pulsatility model formulation becomes:

$$p(x, y) = \frac{1}{|V|} \sum_{k=1}^{n} \frac{V(x_k, y_k)}{(w\sqrt{2\pi})^2} \exp \left(-\frac{1}{2} \frac{||v - v_k||}{w^2} \right) \tag{5.9}$$

where w is modeled as the spatial standard deviation. This pulsatility model can be used by systems of any resolution through appropriate discrete sampling:

$$\Omega(x, y) = \sum_{n=-\infty}^{\infty} \sum_{m=-\infty}^{\infty} \delta(x - n\tau_x, y - m\tau_y) p(x, y) \tag{5.10}$$

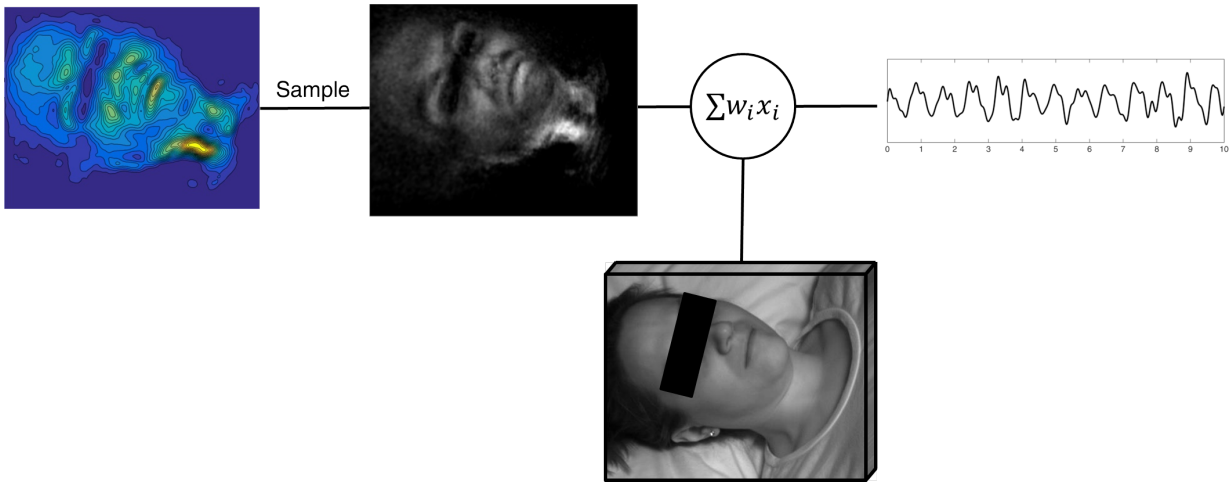

Figure 5.2: Extracting a blood pulse waveform using the probabilistic pulsatility model. The continuous model was discretely sampled to match the resolution of the target frames, and transformed to align the match the anatomical characteristics of the participant. Pixelwise weighted averaging results in a robust blood pulse waveform.

where δ is the 2-D Dirac delta function and τ_x, τ_y are the resolution periods in the coordinate space of $p(x, y)$. A physiologically derived blood pulse waveform can be extracted using the discretely sampled pulsatility map:

$$z(t) = \sum_x \sum_y a_i(x, y, t)\Omega(x, y) \tag{5.11}$$

Figure 5.2 shows a graphical depiction of this process.

5.1.3 Implementation Details

The model was built using 10 s segments for each participant. To reduce minute inter-participant spatial pulsatility differences, each frame was downsampled such that each pixel represented a 3 mm $\times$ 3 mm area. We empirically found that $w = 3$ mm worked well for Equation (5.9).

The mapping function H_i was implemented as a linear projective transformation [69]:

$$\begin{bmatrix} x' \\ y' \\ 1 \end{bmatrix} = \underbrace{\begin{bmatrix} h_{11} & h_{12} & h_{13} \\ h_{21} & h_{32} & h_{33} \\ h_{31} & h_{32} & h_{33} \end{bmatrix}}_{H_i} \begin{bmatrix} x \\ y \\ 1 \end{bmatrix} \tag{5.12}$$

To solve matrix H_i, a least-squares optimization was applied to fit fiducial markers selected on a set of frames to those same anatomical points on a template participant frame (eyes, nose, lips, chin, top and side of head, and suprasternal notch; see Figure 5.1). Specifically, the matrix H_i was solved via a least squares solution of the following linear system of equations:

$$\begin{cases} x' &= h_{11}x + h_{12}y + h_{13} \\ y' &= h_{21}x + h_{22}y + h_{23} \\ 1 &= h_{31}x + h_{32}y + h_{33} \end{cases} \tag{5.13}$$

5.1.4 Results

The imaging system presented in Chapter 3 was used to acquire a series of near infrared frames. Data were collected across 24 participants (age ($\mu \pm \sigma$) = 28.7±12.4; see Table 4.1). The participants were instructed to remain supine for the duration of the study. The camera was positioned overhead at 1.5 m from the participant's head. The camera angle and field of view remained fixed across participants. Participants wore a finger photoplethysmography cuff, providing a ground-truth blood pulse waveform signal synchronously with the video frames.

Setup

The signals extracted using the proposed probabilistic pulsatility model were compared against those extracted using the FaceMean method used in existing PPGI studies [14, 16, 17, 42]. Briefly, the pixels within the facial region found using the Viola-Jones face detection method [70] were spatially averaged for each frame and concatenated, yielding a 1-D temporal signal. A leave-one-out cross-validation scheme was implemented for extracting individual participant signals. That is, participant i was processed using the pulsatility density learned with the data from participants $P \setminus p_i$, where P is the set of all participants and $\setminus$ is the set difference operator. The signals were temporally filtered using the physiologically derived bandpass filter from Equation 3.16, with $f_0 = 30$ bpm and $\kappa = 9$.

Temporal signal fidelity was evaluated by computing the maximum cross-correlation between the extracted signal $\hat{z}$ and the ground-truth signal z from the finger photoplethysmography cuff according to Equation 3.33. Cross-correlation was used to account for pulsatility timing differences between the finger and face ($\Delta t \geq 0$). Spectral signal fidelity was evaluated by computing the spectral signal-to-noise ratio (SNR) of the extracted signal using Equation 3.29. The Wilcoxon signed rank test [71] was used to statistically compare the non-normally distributed pairwise difference between signals extracted using the proposed and FaceMean methods, testing the null hypothesis that the pairwise difference comes from a distribution with zero median (MATLAB R2016b, Mathworks). Heart rate was estimated by the maximum frequency response of a modified spectral power density to reduce frequency discretization error:

$$\mathrm{HR}_i = \arg\max_{f_k} \sum_k Z(f_k) + Z(f_{k+1}) \tag{5.14}$$

Data Analysis

Visualizing the final probabilistic pulsatility model elucidated common arterial pathways. Figure 5.3 shows the (sampled) density across all participants, as well as split by gender. The faces appeared structurally similar to a typical human face, indicating accurate sample alignment based on anatomical anchor points. The forehead, eyebrows, eyes, nose, nostrils, lips, chin and neck were all visually distinguishable. Characteristic differences existed between the female and male probabilistic faces, however the primary anatomy was consistent, leading to a cohesive combined pulsatility map. Facial hair in the male data was observed as reduced pulsatility probability in those areas due to occlusion.

The strongest observed arterial pathway traveled across both sides of the neck. Its anatomical location was consistent with the common carotid artery, which is the primary arterial pathway to the brain and face. The common carotid artery bifurcates into the external (facial) and internal (cerebral) carotid arteries at the top of the neck. A flow trajectory across the jawline was observed in the female pulsatility map (Figure 5.3(b)), which may indicate continued blood flow through the external carotid artery. This phenomenon was not present in the male data (Figure 5.3(c)), due to facial hair occlusion in some participants. Areas around mouth and chin exhibited reduced pulsatility compared to the female data due to facial hair occlusion. Common areas with high pulsing probability across all participants in both genders included the carotid artery pathways, the lips, malar regions, nose, and glabella regions. Pulsing was additionally observed in females along the jaw line.

(a) All participants (b) Female only (c) Male only

Figure 5.3: Discretely sampled probabilistic pulsatility model across all participants (a), as well as split by gender (b,c). The effect of facial hair on reduced observed pulsatility is apparent around the mouth and chin of the male distribution (c). Both genders exhibited strong pulsatility in anatomically relevant locations, such as the neck (carotid artery) and cheeks (facial arteries).

Blood pulse waveform signals extracted using the probabilistic pulsatility model in a leave-one-out cross-validation scheme exhibited stronger temporal and spectral characteristics when compared to those extracted with the FaceMean method. Figure 5.4 shows the distributions of temporal correlation and SNR results across the participant sample. Combined, these measures provide signal fidelity information in both the time and frequency domain. Pairwise comparison of the signals extracted using the proposed and FaceMean methods showed that the proposed method yielded statistically significant correlation ($W = 39, p < 0.01$) and SNR ($W = 31, p < 0.01$) compared to FaceMean signals. Figure 5.5 shows the pairwise differences in correlation and SNR for each of the 23 participants. Temporal and spectral fidelity improvements were observed in a large number of participants. These results indicate that the probabilistic pulsatility model identified areas of strong pulsatility

Many PPGI studies investigate heart rate extraction algorithms for remote monitoring. To validate the proposed system's ability to extract heart rate, correlation and agreement to the ground-truth heart rate was investigated. Figure 5.6 shows the Bland-Altman plot [72] for this heart rate comparison. The proposed system not only attained high correlation to the true heart rate ($r^2 = 0.9619$), but it also achieved strong and tight agreement (error $\mu = 0.52$ bpm, $\sigma = 1.7$ bpm). This is consistent with the strong signal fidelity results in Figure 5.4, which enable strong inferential properties of summary statistics such as heart rate.

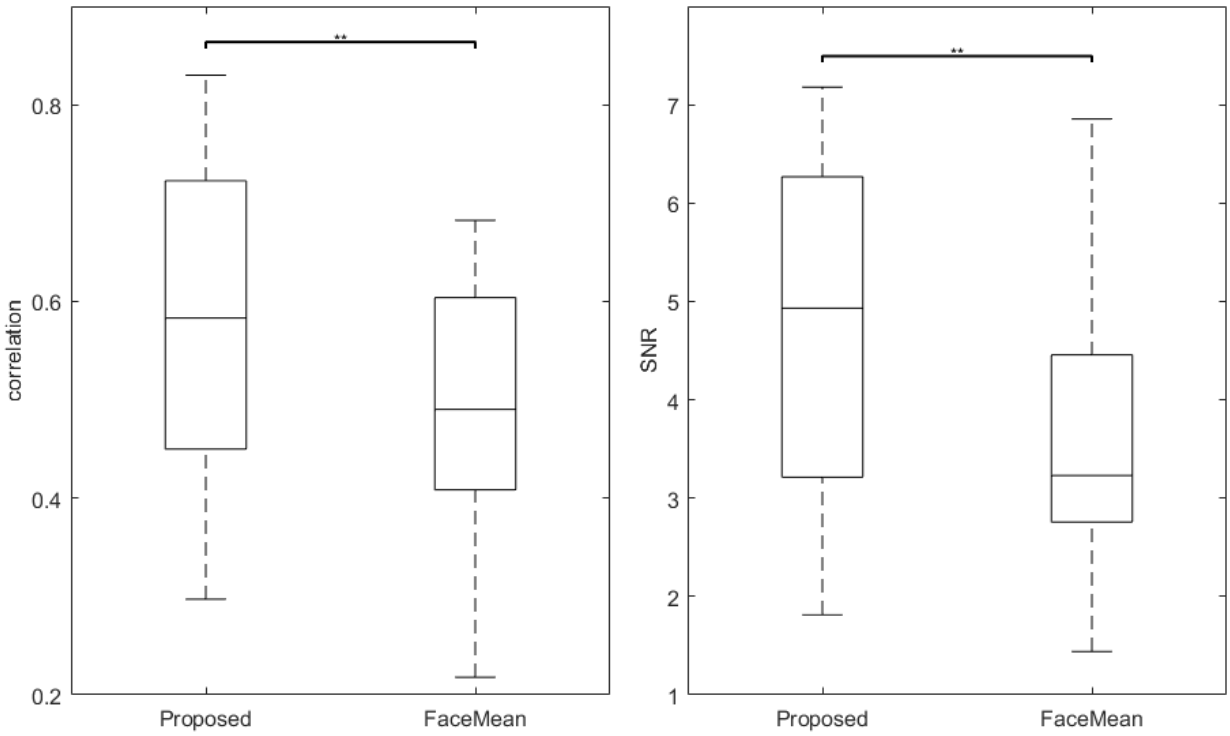

Figure 5.4: Comparison of signal fidelity using the proposed probabilistic pulsatility model versus spatial averaging. Signals extracted using the pulsatility model exhibited statistically significantly higher pairwise correlation to the ground-truth waveform ($W = 39, p < 0.01$) and spectral SNR ($W = 31, p < 0.01$). (**Wilcoxon signed rank test, $p < 0.01$)

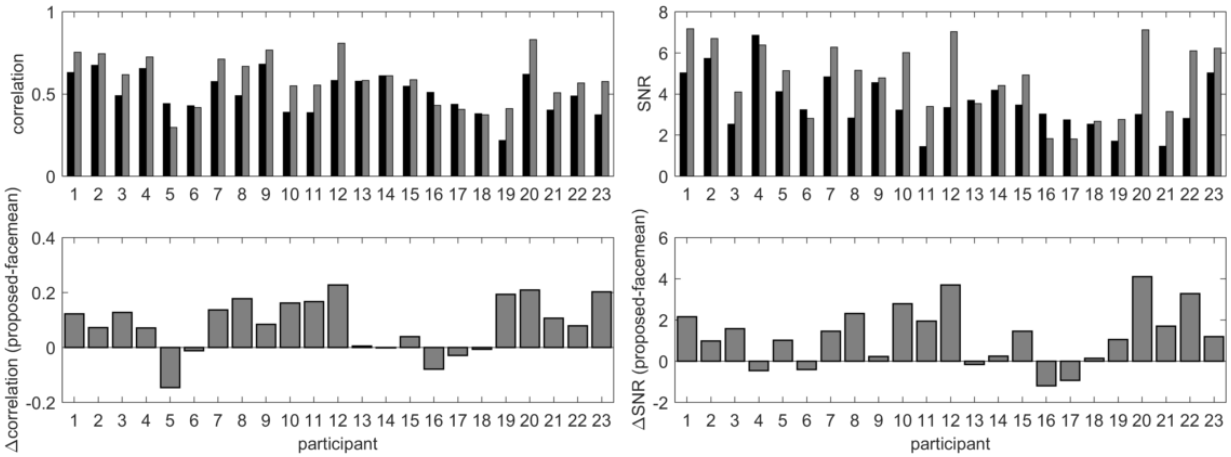

Figure 5.5: Pairwise comparison of correlation and SNR between signals extracted using the proposed pulsatility model (gray) and FaceMean (black). Improvements were observed across most participants when using the probabilistic pulsatility model for extracting blood pulse waveform signals.

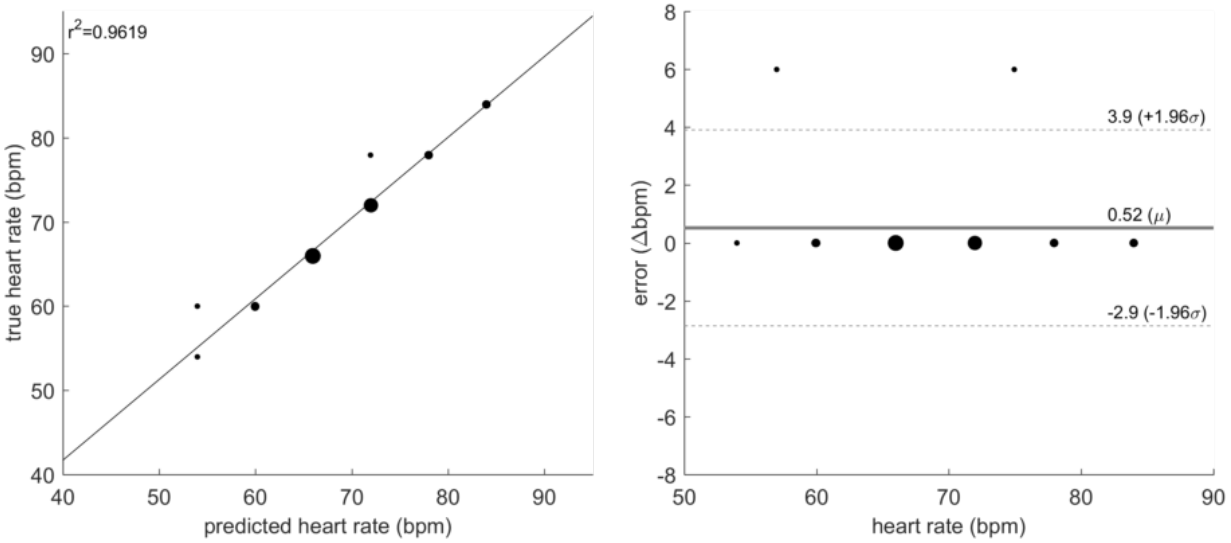

Figure 5.6: Heart rate estimation using the pulsatility density function attained strong correlation to the true heart rate ($r^2 = 0.9619$) and high degree of agreement (error $\mu = 0.52$ bpm, $\sigma = 1.69$ bpm). Marker size indicates the number of points at that coordinate.

5.1.5 Discussion

The results demonstrated that using a spatial probabilistic pulsatility model can enhance blood pulse waveform extraction in photoplethysmographic imaging data. The data-driven pulsatility model, which was constructed using data from a 23 participant sample with widely varying demographics, provides *a priori* anatomical guidance based on consistently observed pulsatile regions.

The data-driven model is built using training data containing spatial pulsatility information. Thus, the new "test" data must sufficiently match the training data's spatial perspective for proper alignment. Though advanced warping models can adjust for some inconsistencies, large deviations in rotation and perspective relative to the training data may produce erroneous alignment. In particular, different imaging and illumination perspectives may change the light-tissue interaction geometry (e.g., shadows), leading to varied photon migration path. To address this challenge, the model was designed such that its methodology is agnostic to the type of data with which it is trained. Thus, independent training data sets can be used to build custom pulsatility models suitable for the study's specific test environment. For example, some systems may find that training based on rotated viewpoints or a certain class of demographic (e.g., gender or age) may yield increased results for their specific test environment. Additionally, this model can be trained on anatomical locations other than the head, enabling whole-body cardiovascular monitoring. The model use can be extended to detect abnormal perfusion patterns that may be early markers for disorders such as peripheral vascular disease or arteriosclerosis.

The model was designed as a continuous model so that it can be sampled by systems of any resolution. To be used, all that is required is a coordinate mapping function H (from Equation (5.5)) for spatial alignment to the template model. In offline systems, this can be accomplished by manual or semi-automatic spatial alignment methods [73]. In real-time systems, automatic alignment is required, and can be accomplished using methods such as automatic face fitting [74]. In low-motion scenarios (e.g., sleeping studies, controlled experiments), a single alignment operation may be sufficient. In scenarios with increased motion, one strategy could be to calibrate the first frame to the template, and align all subsequent frames to the calibrated source frame, as it would have more similarities to frames within the same video than the model template.

5.1.6 Conclusion

A continuous probabilistic pulsatility model was developed that describes anatomical locations that consistently exhibited arterial pulsing across a 23 participant sample. This

model can be used as *a priori* information to enhance signal extraction in photoplethysmographic imaging systems. Since the model is a continuous model, it can be used by systems of any resolution via appropriate spatial sampling. Results showed that signals extracted using the pulsatility model exhibited statistically significant higher correlation and SNR versus unguided whole-area uniform averaging. Discretely sampled maps identified areas of consistently strong pulsing across the training data in the head, specifically the neck, malar regions, glabella regions, lips and nose.

5.2 Jugular Venous Pulse Waveform

5.2.1 Introduction

Cardiovascular disease is the leading cause of mortality, resulting in 17.3 million deaths per year globally, and a third of all deaths in the United States [1]. Cardiovascular monitoring is essential to assessing and maintaining or enhancing quality of life through preventive and acute care. The jugular venous pulse (JVP) waveform is a powerful diagnostic tool for assessing cardiac function. The jugular vein is a major venous extension of the heart's right atrium, so changes in atrial pressure are reflected in the jugular waveform. Distortions in the JVP provide insight into cardiac function without direct assessment of the heart itself, such as resistance diseases (e.g., pulmonary hypertension, tricuspid stenosis [21, 39]), mechanical diseases (e.g., tricuspid regurgitation [39]), electrical diseases (e.g., atrial fibrillation, heart block, atrioventricular dissociation [39]), abnormal external forces (e.g., tamponade, constrictive pericarditis [39, 75]), and heart failure [76].

A primary problem with assessing JVP lies in the current standard method of measurement: invasive catheterisation. Catheterisation requires surgically inserting a central line into the jugular vein, superior vena cava, or right atrium. This is an invasive procedure requiring surgical expertise. Therefore, although the JVP can provide important clinical insights, JVP examination is not routine and is only performed when there is probable cause for monitoring. Additionally, since catheter monitoring is limited to measuring a single location, spatial flow perfusion characteristics cannot be assessed, which may encode important clinical information [77, 78]. Ultrasound has recently been proposed to measure the JVP through Doppler velocity imaging [79, 80]. However, these methods require constant stable probe skin contact, expensive ultrasound equipment, trained ultrasound technicians, and is only able to provide axial hemodynamic information.

PPGI provides a potentially unique solution to this problem, however, existing PPGI systems have been limited to extracting high-level vital signs, such as heart rate [10, 14,

16, 19, 44] and respiratory rate [14, 40]. The few studies that have reported spatiotemporal perfusion have been limited to perfusion through the hand in constrained environments [13, 81]. Analysing the spatiotemporal trajectory patterns in the neck can provide insight into whether PPGI can be used to detect the JVP. Given the clinical promise of non-invasive JVP assessment, we are motivated to investigate the feasibility of biophotonic observation of the jugular pulse in the neck, as well as information about its spatial perfusion patterns.

In this exploratory study, we investigated the feasibility of non-contact biophotonic JVP monitoring by assessing the spatiotemporal pulsing patterns in the neck in 24 participants. Strong pulsatile flow was successfully observed, consistent with ground truth finger photoplethysmography measurements. Two different types of pulsatile flow were observed in all participants: one that corroborated with the ground truth arterial pulse, and one that exhibited strong inverted pulsing characteristics. The hypothesis was that the two pulsatile flows were major arterial and venous blood flow waveforms. To test this hypothesis, the spatial properties of the pulsing were compared to the carotid artery and jugular vein track found through ultrasound, and the waveforms were compared to the JVP. Major venous flow was observed in all participants. Here, we demonstrated for the first time, to our knowledge, that the JVP could be assessed with a PPGI system. Furthermore, the jugular pulse waveform was observed at many different locations along the venous track, providing indication of the pulse trajectory.

5.2.2 Methods: Signal Analysis Framework

Study protocol

Data were collected across 24 participants (age ($\mu \pm \sigma$) = 28.7 ± 12.4; see Table 4.1). Figure 5.7 graphically shows the setup of the study. The participants were asked to assume a supine position for the duration of the study. To avoid visual occlusion of the neck, the ground truth blood pulse waveform was collected using a finger photoplethysmography (PPG) cuff simultaneously with the video data. An ultrasound technician placed an 11 MHz ultrasound probe (Vivid i, General Electric Healthcare, Horten, Norway) on the neck after video imaging. Upon locating the vessel anatomy, the pressure exerted on the probe was released until the probe broke contact with the skin, and then reapplied gently to the gel interface in the same location to allow undisturbed vessel diameter analysis. Ultrasound videos were collected at 12 fps. B-mode cross-sectional videos were acquired to confirm the location of the jugular vein relative to the carotid artery, and confirm vessel pulsatility characteristics frame-by-frame. The jugular vein was identified by pressing the

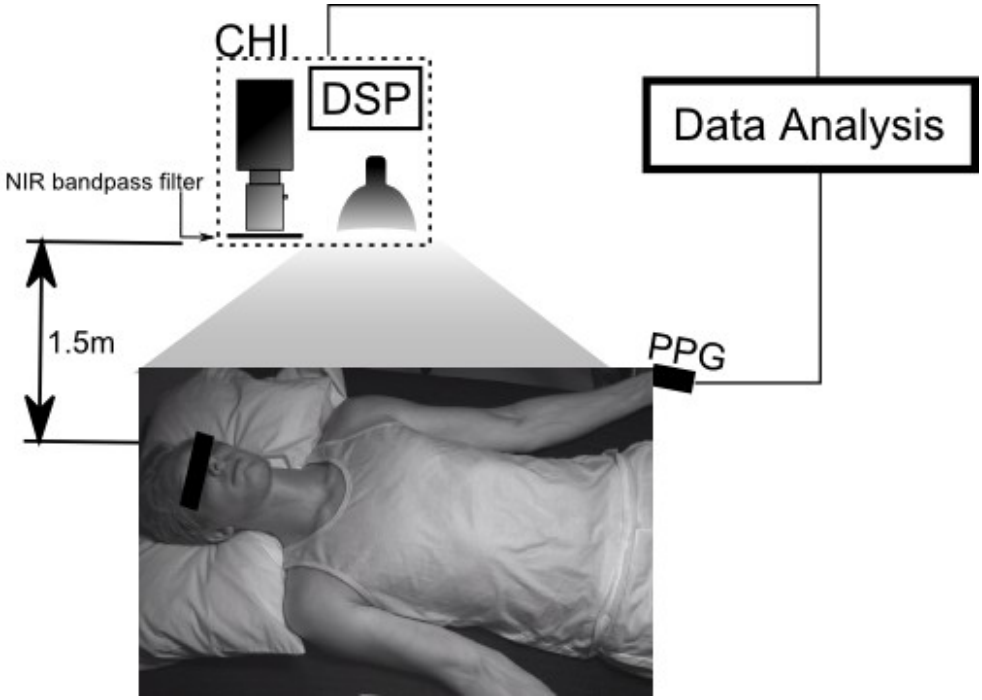

Figure 5.7: Study setup. Participants were supine for the duration of the study. The biophotonic imaging system was positioned above and slightly to the right of the participant, at a distance of 1.5 m. The participant wore a finger cuff which provided the ground truth arterial waveform for the analysis.

probe into the skin and observing which of the two vessels collapsed through the cross-sectional view. Longitudinal Doppler measurements were acquired of the jugular vein to validate pulsatile jugular flow. The carotid and jugular paths were marked after video collection to anatomically map the observed pulse's location. Informed consent was obtained from all participants, and by those participants whose photos were used in this paper. The study was approved by a University of Waterloo Research Ethics committee and performed in accordance with the Declaration of Helsinki.

Data Collection

The imaging system presented in Chapter 3 was used to collect a series of near infrared frames for increased photon penetration (to reach vasculature) and low melanin absorption (skin tone insensitivity) [28]. The illumination was secured at a fixed distance using a light

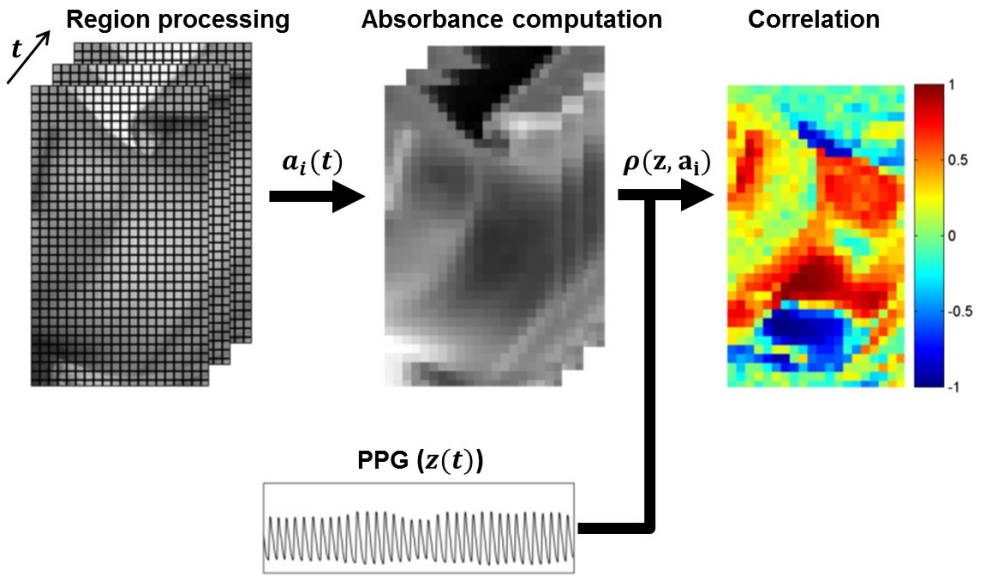

Figure 5.8: Data processing pipeline. Each frame was analysed in 0.25×0.25 mm regions. Each region's temporal fluctuations were converted to absorbance using the framework presented in Chapter 3. Pearson's linear correlation coefficient was computed for each waveform using the ground truth PPG waveform, yielding a spatial correlation map showing locations exhibiting strong forward and inverted pulsing. Best viewed in colour.

stand to ensure stable skin irradiance, and it was uniformly projected using a 16" glass fabric front diffuser. Both the illumination source and imaging system were situated 1.5 m above the participant. Pixel distances were pre-calibrated using a resolution target at the known fixed imaging distance. In one case, the participant's neck was not visible from overhead, so a bedside view was used.

Figure 5.8 shows the signal processing pipeline for the study. Each frame was blockwise averaged using 5×5 mm regions. The temporal fluctuations of region i yielded a reflected illumination signal $x_i(t)$:

$$x_i(t) = \frac{1}{|R_i|} \sum_{v_j \in R_i} v_j(t) \tag{5.15}$$

where R_i is the 5×5 mm pixel region surrounding pixel i, and $v_j(t)$ is the j^{th} pixel value at time t. Denoised absorbance frame signals were computed using the system presented in Chapter 3, yielding absorbance signals $a_i(t)$. Using the finger PPG signal as the ground truth arterial blood pulse waveform, Pearson's linear correlation coefficient

was computed between each region's temporal absorbance signal $a_i(t)$ and the PPG signal $z(t)$ to determine the signal strength and directionality, yielding $r(z, a_i) \in [-1, 1]$ (see Equation 3.30). Note that this is temporal correlation, not scatter data correlation, where $r > 0.5$ indicates strong pulsing consistent with the PPG arterial pulsing signal, and $r < -0.5$ indicates strong pulsing that is inversely proportional to the PPG signal. For visualisation purposes, the colour maps were smoothed using a Gaussian kernel ($\sigma = 2.5$ mm) to show cohesive flow pathways.

In some cases (e.g., cold fingers), the carotid arterial waveform's shape differed substantially from the finger PPG waveform. In these cases, the waveform that exhibited the strongest spectral signal-to-noise ratio (SNR) with respect to the PPG waveform was used instead. SNR was calculated in the frequency domain across all regions according to Equation 3.29. The template waveform was then chosen as follows:

$$z = a_{i^*}, \tag{5.16}$$

$$i^* = \arg\max_i \{\mathrm{SNR}(Z, A_i)\} \tag{5.17}$$

5.2.3 Results

Detection of pulsatile flow

To test the base hypothesis that the imaging system was able to consistently detect localised pulsatility in vascularised locations, each 5×5 mm region was analysed for pulsatile blood flow. The strongest 2.5 cm^2 tissue area of positively and negatively correlated pulsatile regions were identified, totalling 5 cm^2 tissue area. Figure 5.9 shows the correlation distribution of the strongest 5 cm^2 total tissue, across all participants. Pulsatile flow was consistently observed across all participants. The distribution is strongly bimodal, indicating both strong arterial ($r = 0.85 \pm 0.08$) and inverted ($r = -0.73 \pm 0.17$) pulse signals relative to the ground truth PPG. That is, some signals exhibited strong positive correlation to the PPG waveform, whereas other signals exhibited strong negative correlation to the PPG waveform. Strong signals ($|r| > 0.5$) were found in most participants. The weakest signals were found in participants with high body fat content and age-related skin inelasticity. This may be problematic in participants with higher body fat, which are prevalent in those affected by cardiovascular disease. Thus, in future work, different positions beyond resting supine can be explored to mitigate the spectral effect of adipose tissue. For example, lengthening of the neck by looking up or to the side, and tilted posture may be effective at reducing localized adipose tissue effect.

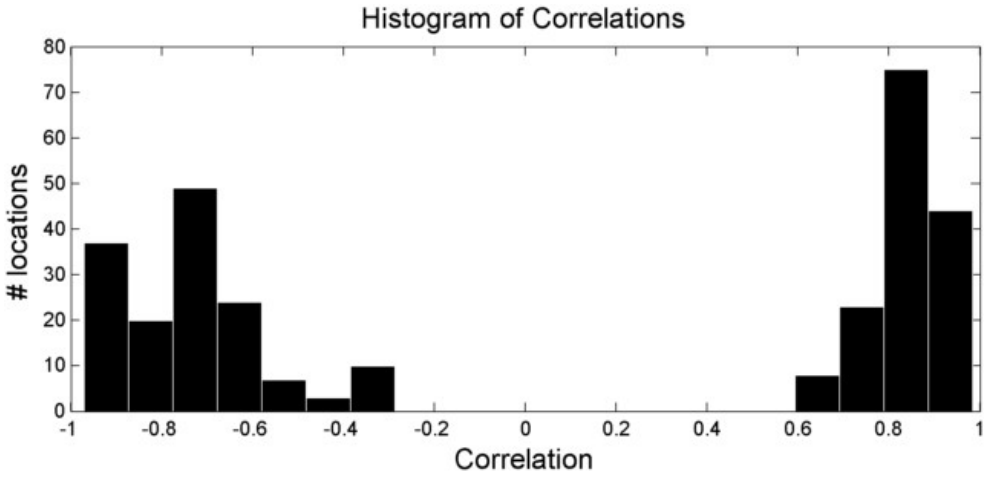

Figure 5.9: Histogram of the strongest signal correlation values relative to ground truth arterial waveform across all participants ($n = 24$). The distribution is strongly bimodal, indicating one group of signals that are highly correlated with the arterial waveform, and another group that is strongly negatively correlated with the arterial waveform.

Characteristics commonly found in major arterial waveforms were observed in the positively correlated waveforms, including a sharp increase in absorbance toward a systolic peak, followed by a dicrotic notch, then a diastolic minimum. The "inverted" waveforms exhibited different characteristics, specifically a gradual rise, followed by a steep drop in absorbance, and often a small fluctuation following the drop. These arterial rises and inverted drops were temporally in sync. Figure 5.10 shows a typical example of the two types of pulses observed in a participant. The two pulses were strongly correlated through an inverse relationship ($r = 0.96$), and each exhibited strong spatially cohesive patterns. Figure 5.11 shows the inverted pulse signal acquired for all participants. The hypothesis was that the system was detecting both arterial and venous blood pulses. The following subsections tested this hypothesis.

Primary anatomical locations of strong pulsing

Figure 5.12 shows selected frames from a video of the flow profiles. Each frame in the original video capture was overlaid with a colour map indicating pulsatile flow. Signals that exhibited strong positive correlation (see Equation 3.30) were coded in red, and those with negative correlation were coded in blue. The opacity strength was computed as $r^2(z, a_i)$, where r is the correlation. The overlay was processed with a Gaussian smoothing

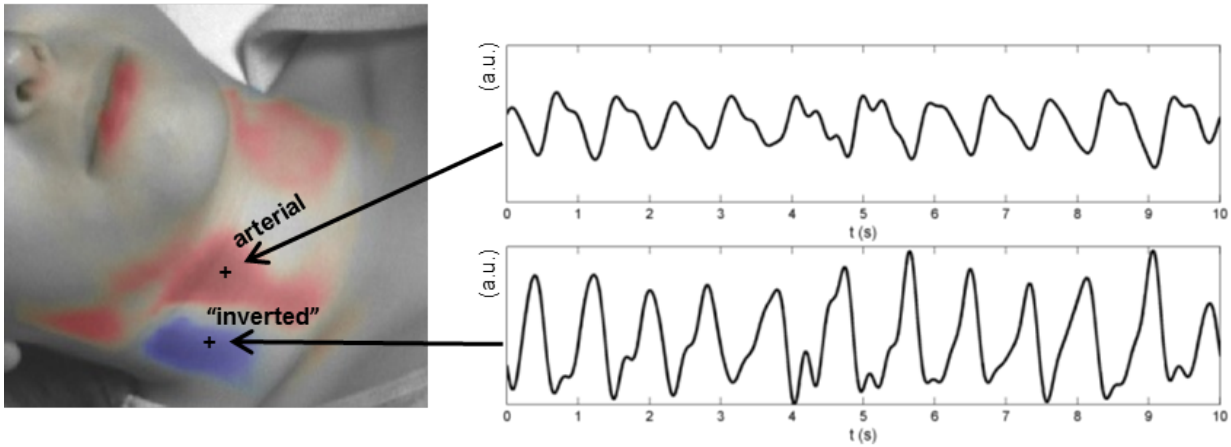

(a) Arterial and "inverted" waveforms

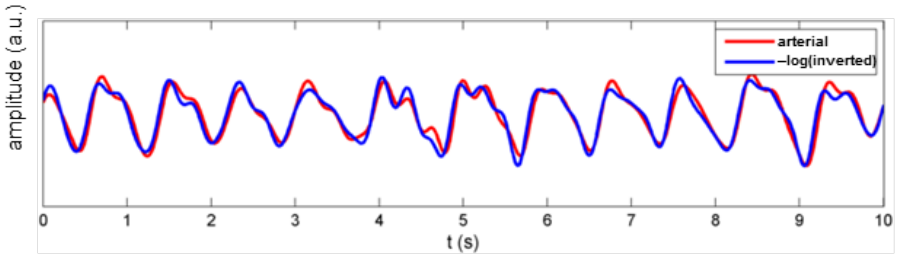

(b) Arterial and –log(inverted) waveforms

Figure 5.10: Comparison of scale-normalized arterial and inverted pulse waveforms in a typical example. (a) The participant exhibited strong arterial pulsations, characterised by a sharp rise to systole and a dicrotic notch, as well as strong inverted pulsations, characterised by a phase-offset gradual rise and sharp drop. (b) The arterial and inverted waveforms are strongly linked through an inverse relationship ($r = 0.96$). Best viewed in colour.

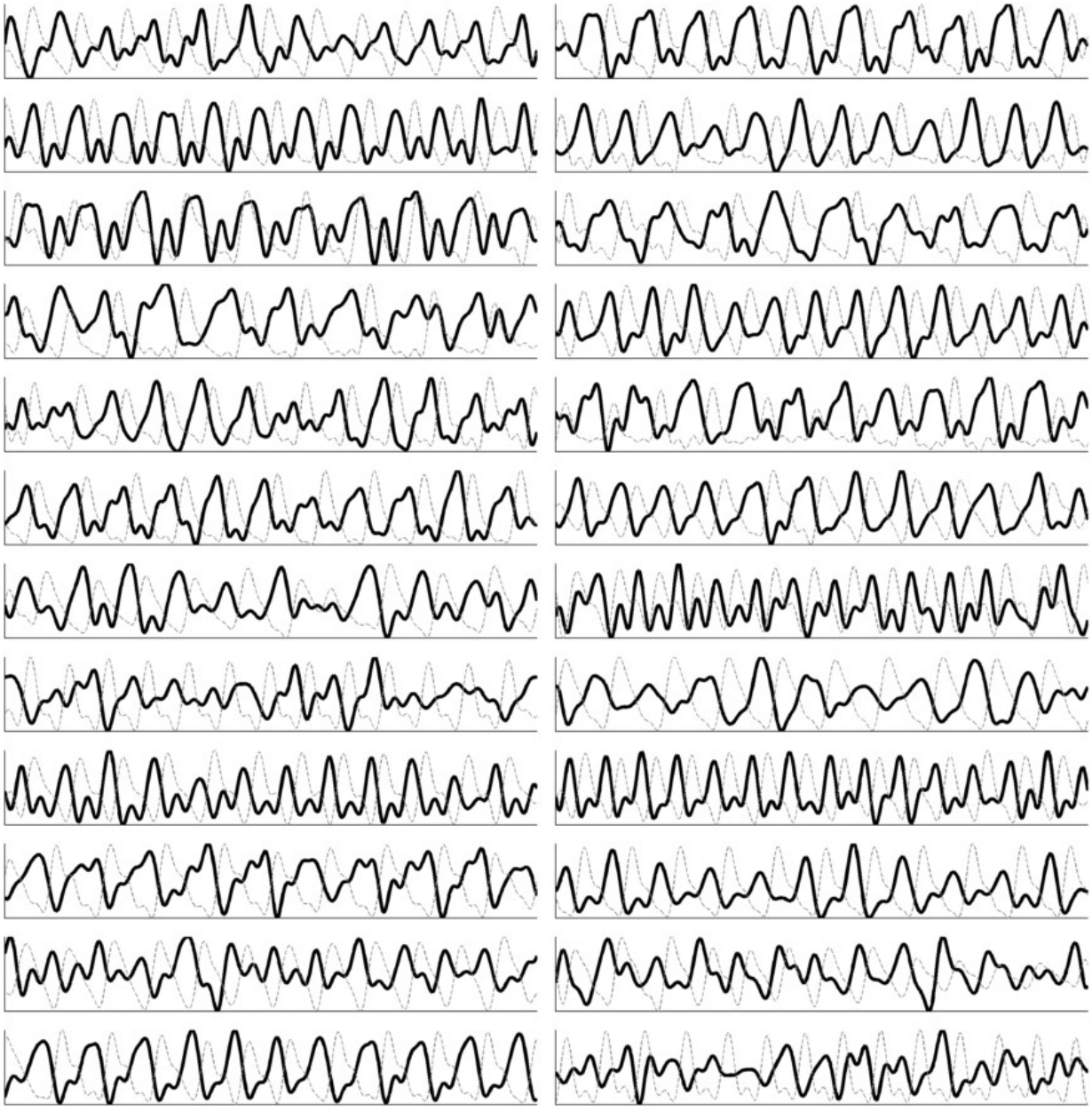

Figure 5.11: Jugular venous pulse signal acquired for each participant (n=24). The jugular venous pulse (black line) acquired using the non-contact coded hemodynamic imaging system is compared to the ground-truth arterial waveform (dotted gray). The two waveforms are strongly inversely proportional, some more strongly than others due to factors such as fat content and age-related skin inelasticity.

kernel for visualization purposes.

The two types of flow were easily identified visually due to the phase offset nature of their peaks. Specifically, the arterial track filled with blood simultaneously as the ground truth arterial waveform reached systole. When the arterial waveform reached diastole, the inverted pulse reached its peak. The two tracks exhibited consistent alternating pulsing patterns.

Figure 5.13 shows the locations on the neck where the five strongest positive and inverted pulsations occurred for each participant. Following data collection, the carotid and jugular tracks were marked with the guidance of ultrasound. Comparing the marked locations with the major pulsing locations, the arterial pulse locations followed the carotid track. Inverted pulsatile flow was consistently situated on the distal side of the carotid artery. This was consistent with cross-sectional ultrasound imaging, which located the jugular vein on the distal side of the common carotid artery in all participants.

During data analysis, Doppler ultrasound confirmed that the jugular vein was pulsatile in all 24 participants, and cross-sectional ultrasound analysis visually confirmed the phase offset nature of the carotid and jugular pulsing.

Correlation to jugular venous pulse waveform

The inverted blood pulse waveform shape was consistent with the jugular venous pulse (JVP) waveform [82]. Figure 5.14 shows the time-aligned Wiggers diagram section with the labeled JVP and a typical inverted pulse observed during trials. Visually, the JVP and inverted pulse waveforms show strong intercorrelation. The JVP waveform is biphasic and is characterised by: an increase in pressure pre-systole due to right atrial contraction (a); an increase in pressure due to ventricle contraction (c); a decrease in pressure during systole due to atrial relaxation following tricuspid valve closure (x); an increase in pressure in late systole due to right atrial filling from venous return (v); and a decrease in pressure during diastole due to right ventricular filling from the opening of the tricuspid valve (y). The inverted pulsing results were consistent with the JVP waveform: gradual increase in blood volume pre-systole (a); an increase in pressure during ventricular systole (c); a sharp decrease in blood volume was observed slightly prior to the carotid upstroke (x); and a small transient rise in blood volume during late systole (v,y). Since the JVP is governed by differential pressures generated by heart mechanics, observing the venous pulsation patterns can provide insight into not only vascular function, but aspects of heart function as well, without catheterisation. Figure 5.15 shows a single pulse waveform for

(a) Frame 1 (b) Frame 2 (c) Frame 3

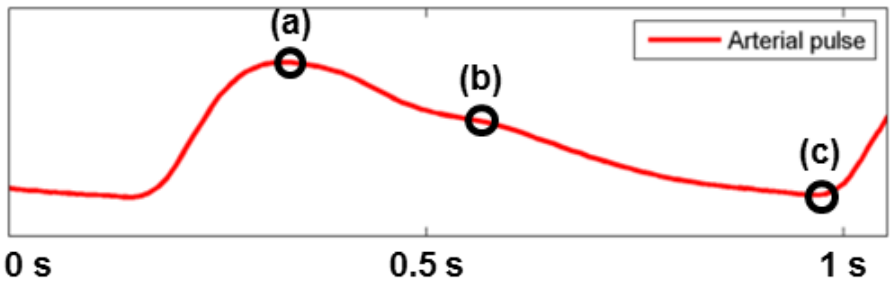

(d) Frame times on arterial waveform

Figure 5.12: Three frames from a typical segment showing the timing of the blood volume pulse in the neck. (a) Upon ventricular ejection, the pulse travels through the carotid arterial track (red), reaching systole; there is no inverted pulsatile flow. (b) During the arterial descent towards diastole, the pulse continues to travel through the carotid track, and the start of the inverted pulse can be observed (blue). (c) No carotid pulse is observed during diastole, and the inverted pulse experiences its maximum absorbance. Best viewed in colour.

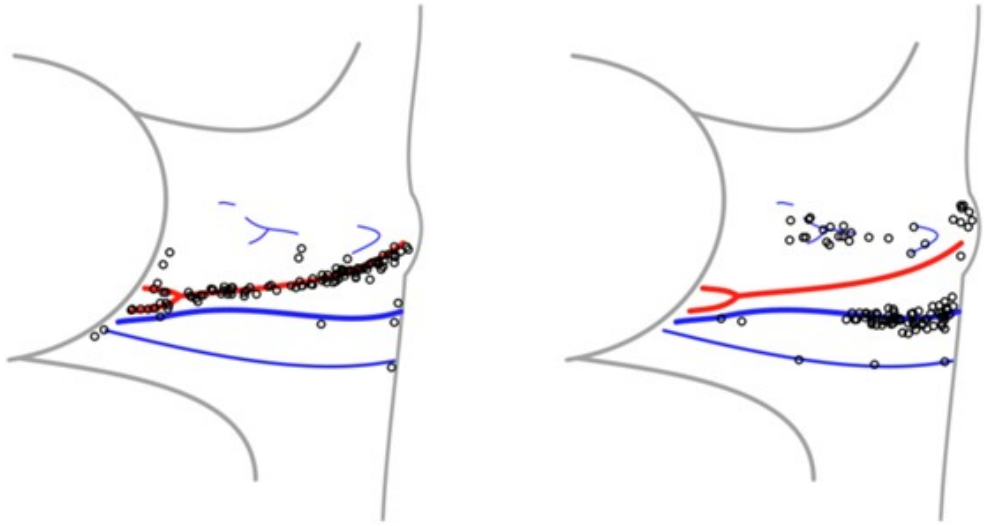

Figure 5.13: Locations exhibiting the strongest pulsing across all participants ($n = 24$) relative to the position of the carotid artery and jugular vein. Locations were determined by finding and marking the carotid and jugular track using ultrasound following video data capture. The pulsing locations were normalized and drawn relative to the individual's marked anatomy. The data are presented for the right side only (marked with 'o'), which is used clinically as the most direct conduit to the heart. The arterial pulse points were consistent with the anatomical location of the carotid artery (a), and the inverted waveform pulse points were consistent with the distal location of the jugular vein (b). Best viewed in colour.

each participant. The *c, x, v* and *y* waves were consistently observed across all participants, and the subtle pre-systolic *a* wave was observed in 13 participants.

5.2.4 Discussion

These trials support the hypothesis that the PPGI system was able to observe the spatial trajectory of both major arterial and venous blood pulse waveforms in the neck. The amplitude changes of the two signals exhibited different differential properties. In particular, the arterial signal was characterised by a sharp rise during systole followed by a fall during late systole and diastole, whereas the venous signal was characterised by a gradual rise during atrial filling followed by a sharp drop during atrial and ventricular contraction. These findings are consistent with expected transient local blood volume absorption fluctuations [7], supporting the hypothesis that the data is indeed revealing light-tissue mechanisms rather than a ballistocardiographic mechanisms.

The strong negative correlation between the arterial and venous blood pulse waveforms can be attributed to the differential pressure profiles resulting from normal cardiac cycles. The observed results are consistent with the Wiggers diagram. In particular, cardiac contraction ejects blood through the arterial track, and ends with aortic closure. During arterial systole, atrial relaxation causes a decrease in cardiac pressure, resulting in increased venous return into the right atrium, which reduces the volume in the neck veins. Atrial filling pressure gradually increases simultaneously with late systole, resulting in decreased venous return (increased jugular venous volume). This inverted amplitude and phase-offset vessel wall motion was visually confirmed using B-mode ultrasound, where cross-sectional videos showed phase-offset vessel wall expansion and contraction between the carotid artery and jugular vein (see Figure 5.16). Doppler ultrasound was also used to confirm the pulsatile nature of the jugular vein in the participants consistent with the JVP waveform.

Due to the close proximity of the major neck vessels to the heart, the venous blood pulse waveform can be used to assess heart function. Leveraging the strong correlation between the venous blood pulse waveform and JVP, PPGI can be used to assess heart function that is reflected in the venous waveform in a non-contact manner. Since the jugular vein is a major venous extension of the right atrium, abnormalities in the waveform can indicate heart function problems. For example, the increased pressure from atrial contraction due to tricuspid stenosis produces a larger *a* wave [39,84]; a lack of atrial contraction/relaxation from atrial fibrillation inhibits the *a* wave and *x* wave [39]; and blood flow back through the atrium due to tricuspid regurgitation results in a fused *c*-*v* wave [39]. The *c, x, v*

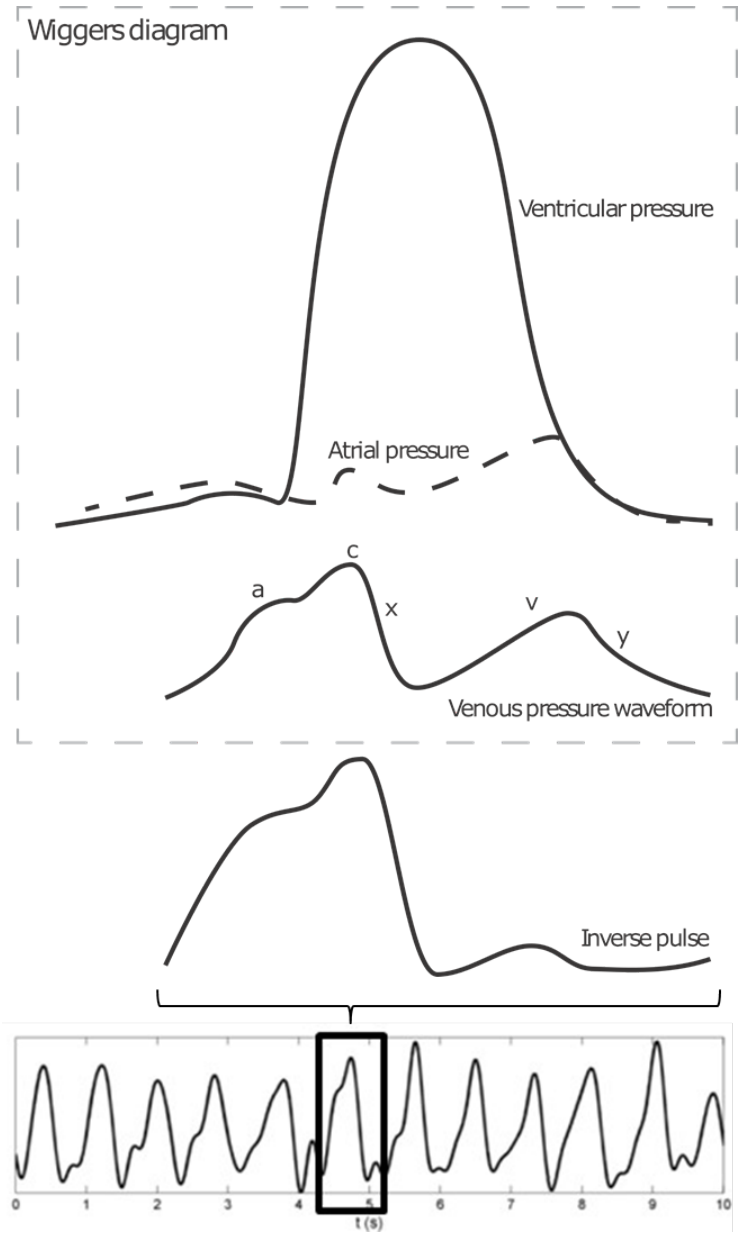

Figure 5.14: Comparison of a typical "inverted" pulse to the jugular venous pulse waveform in the Wiggers diagram (adapted from [83]). The inverted pulse was consistent with the JVP waveform. The JVP waveform is biphasic whose waveform inflections are governed by differential cardiac pressures (see text). The variability between individual pulses is likely due to the effect of respiration on the intrathoracic pressure.

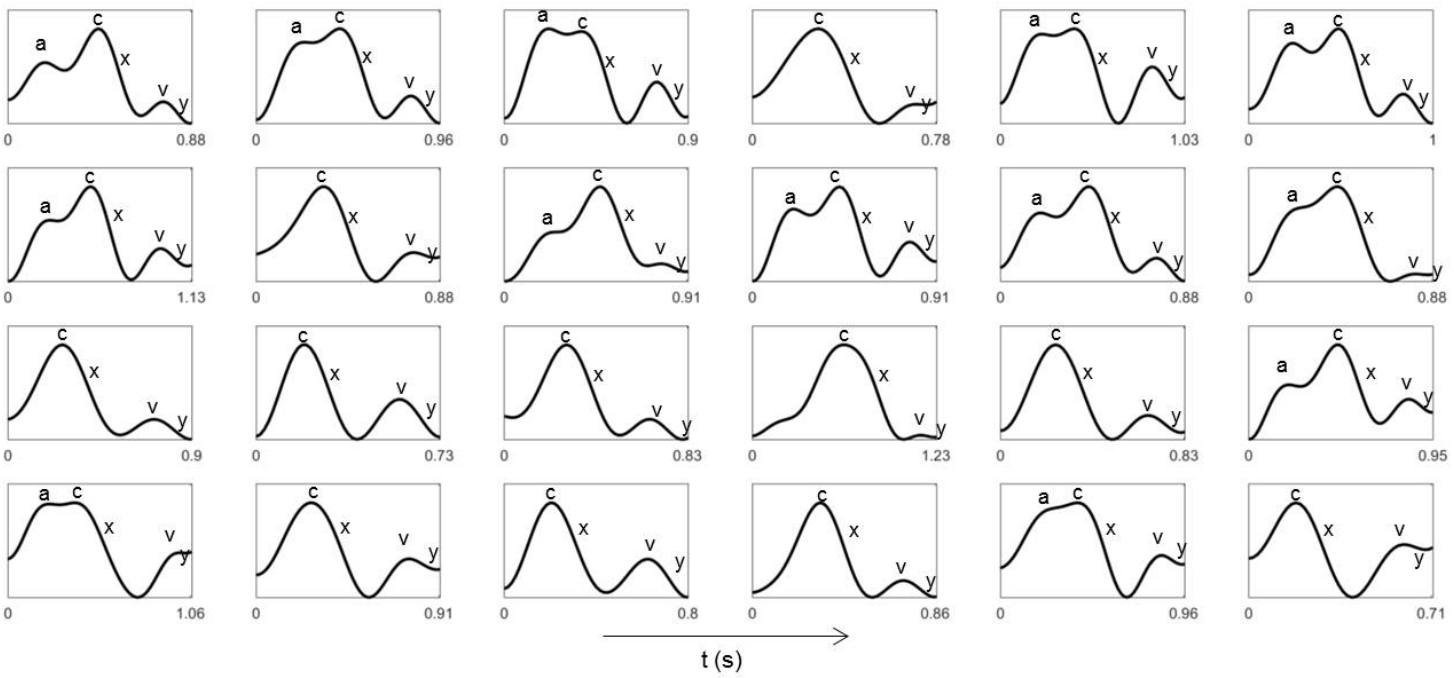

Figure 5.15: Example of a single pulse extracted from each participant. The characteristic JVP waves were manually identified in each waveform and annotated for clarity. Four of the major JVP waves (c, x, v, y waves) were observed in all participants. The subtle pre-systolic a wave was observed in 13/24 participants.

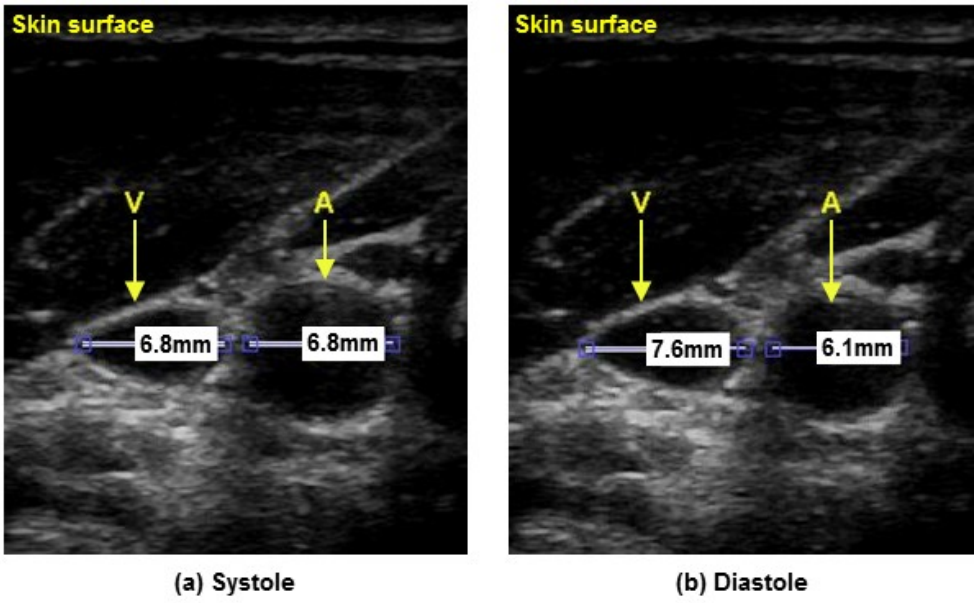

(a) Systole (b) Diastole

Figure 5.16: Inverse relationship between the carotid artery and jugular vein as seen with B-mode ultrasound in a typical participant. The jugular vein (below V) and carotid artery (below A) are located below the skin surface (top) with vessel diameters marked in millimetres. Between systole (a) and diastole (b), the carotid relaxes (10% diameter reduction), and the jugular expands (12% diameter expansion).

and y waves were consistently observed in all participants, however the a wave was only observed in a subset of participants (13/24). The pre-systolic a wave is a subtle signal exhibited by the backflow of venous blood from right atrial contraction. The imaging sensor properties (bit depth, pixel noise magnitude, and frame rate) may have contributed to an undetected a wave in individuals with lower central venous blood volume or weaker right atrial contraction. Future work must systematically evaluate the effect of imaging sensor properties on JVP extraction to elucidate this relationship.

Due to a gap in current clinical monitoring technology, potential clinical information encoded in the spatial flow profile is largely unknown. For example, flow velocity and jugular column height can be assessed using the proposed hemodynamic imaging system, which may be important indicators of heart function and central venous pressure [77, 78]. Clinical studies leveraging the presented work may elucidate the effect of spatial flow profile analysis on heart failure diagnosis and prevention. Future work will investigate the relationship between pulsatile signal characteristics and demographic groups.

5.2.5 Conclusion

This study is the first PPGI study to demonstrate the ability to observe the JVP. Currently, the system is limited to at-rest monitoring with minimal motion, but image processing functionality can be incorporated in future work, including motion compensation sensing [14]. Building on these findings, future work must focus on clinical validation against catheter or ultrasound JVP. A rigorous comparison against current JVP monitoring technology is essential for clinical viability of such a technology to help doctors monitor cardiac dysfunction for rapid visual patient assessment in non-surgical settings. These early findings show promise for shifting from catheter insertion techniques for measuring the JVP waveform toward a non-contact, non-invasive biophotonic imaging solution.

5.3 Arrhythmia Detection

5.3.1 Introduction

Cardiac arrhythmias are irregular heart contractility patterns due to abnormalities of the heart's electrical system. Though the prolonged effects of arrhythmias may result in severe tissue damage, arrhythmias commonly go undetected due in part to the lack of non-intrusive continuous cardiovascular monitoring technologies in natural environments.

Though PPGI shows promise for remote cardiovascular screening, many existing processing methods rely on frequency domain processing [38], which assumes stationary (i.e., statistically temporally invariant) data. This is an incorrect assumption for waveforms containing cardiac arrhythmia, which are non-stationary due to the transient temporal cardiac anomalies. Here, we propose a non-stationary processing method to investigate the feasibility of arrhythmia detection using CHI. Using a wavelet transform formulation, time-frequency representations are computed and results from a participant experiencing cardiac arrhythmia are compared against results from a control baseline.

5.3.2 Methods: Time-Frequency Processing

Time-Frequency Representation

The continuous wavelet transform was used to compute the time-frequency representation of the non-stationary signal. Wavelets are temporally localized wave-like functions that are useful in signal processing for time-frequency analysis [85, 86]. The wavelet transform depends on a chosen "mother wavelet", which it slides and scales to compute temporally localized strength matches with the underlying signal. A Morlet wavelet was chosen since its structure emphasizes a strong systolic peak and a dicrotic notch. Its rapid temporal decay models the fall from systole to diastole well. Figure 5.17 shows the physical depiction of a Morlet wavelet. The wavelet function was computed as the product of a sinusoidal wave and a temporal Gaussian envelope:

$$\psi_0(t) = \exp\left(-\frac{t^2}{2}\right)\cos(5t) \tag{5.18}$$

To compute the time-frequency representation of a signal, the wavelet was scaled and shifted according to:

$$\psi\left(\frac{(t'-t)\delta t}{s}\right) = \left(\frac{\delta t}{s}\right)^{\frac{1}{2}}\psi_0\left(\frac{(t'-t)\delta t}{s}\right) \tag{5.19}$$

Using this analytic signal, the continuous wavelet transform was used to compute the time-frequency representation of the waveform signal:

$$X(a,b) = \frac{1}{\sqrt{a}}\int_{-\infty}^{\infty}\hat{z}(t)\psi\left(\frac{t-b}{a}\right)dt \tag{5.20}$$

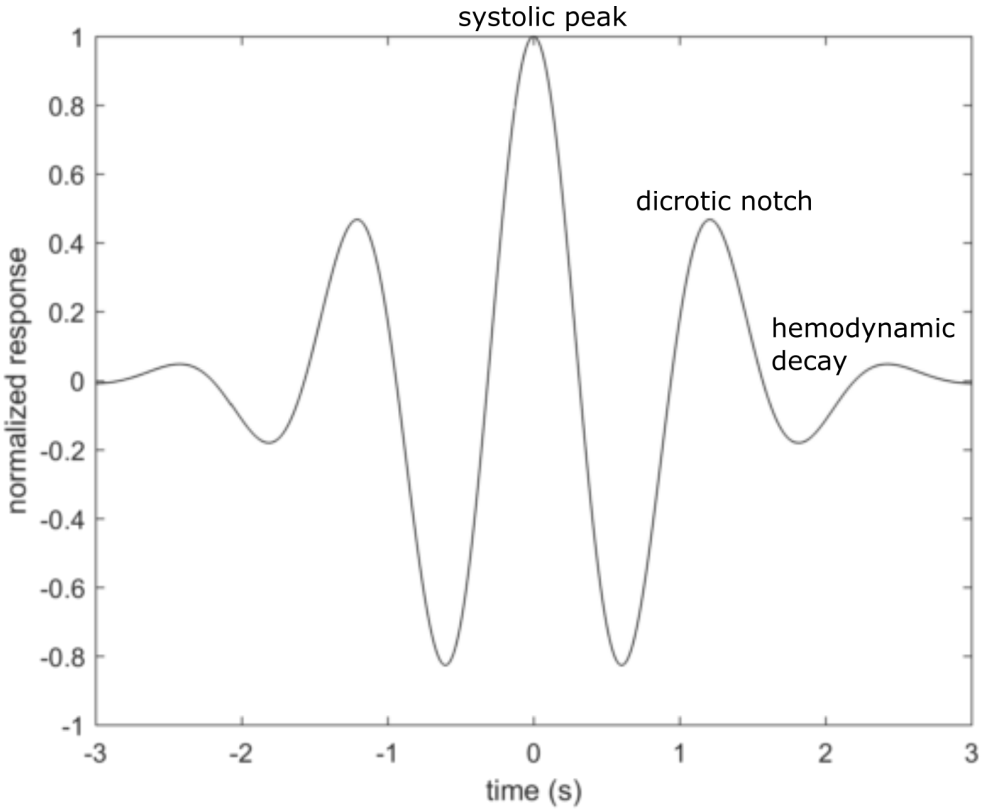

Figure 5.17: Morlet wavelet used in hemodynamic time-frequency processing. This wavelet emphasizes strong systolic peak and a dicrotic notch, with a rapid temporal decay consistent with blood pulse waveform physiology.

for scale a and temporal translation b. In this initial investigation, this time-frequency representation was used to analyze the effect and presence of temporally transient cardiac arrhythmias.

Figure 5.18 shows an example hemodynamic waveform with its wavelet decomposition using the Morlet wavelet. The wavelet energy is strong and compact around a fundamental frequency which is consistent with the observed heart rate (78 bpm, or 1.3 Hz). A secondary energy band is observed at a harmonic frequency, which is as a result of the dicrotic notch.

Blood Pulse Waveform Extraction

Figure 5.19 shows an overview of the proposed method. Absorbance frames were computed from a set of near infrared frames according to the framework presented in Chapter 3. A blood pulse waveform must be extracted from the series of frames to determine the presence of cardiac arrhythmias. The spectral-spatial pixel fusion method from Chapter 4.2 was used to extract this waveform. Briefly, this method uses a Bayesian least squares formulation to estimate the probabilistically optimal blood pulse waveform signal. The posterior distribution is modeled using spectral and spectral physiological prior models. Specifically, given a set of absorbance frames, the "true" waveform was estimated using a Bayesian least squares formulation:

$$\hat{z} = \int \frac{z \sum_{i=1}^{|X|} W_i \delta(|z - x_i|)}{Y_z} dz \tag{5.21}$$

where z is a candidate waveform, X is a set of measurements, Y_z is a normalization term, δ is the Dirac delta function, and:

$$W_i = \min \left\{ \prod_k w_{ik} \mid N_i \right\} \tag{5.22}$$

where w_{ik} are the set of k spectral-spatial weights for the signal extracted from tissue location i, and N_i is the pixel neighborhood around tissue location i.

5.3.3 Results

Data were collected at a distance of 1.5 m from the participant using the imaging system presented in Chapter 3. To reduce measurement noise, each distinct 3×3 mm region was blockwise averaged. Data were acquired from two participants: one experiencing cardiac

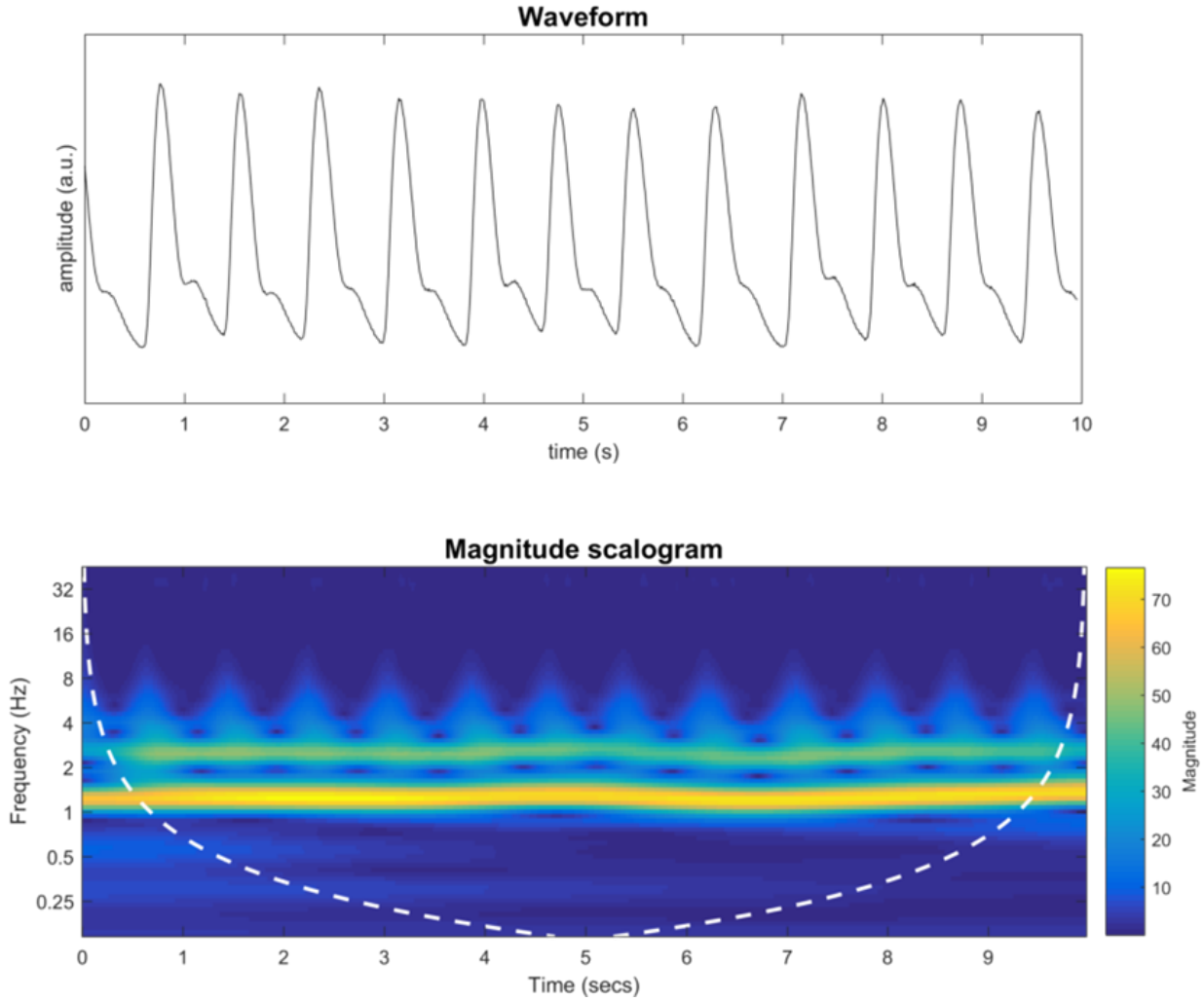

Figure 5.18: Example hemodynamic waveform wavelet decomposition using the Morlet wavelet. The wavelet energy is highly concentrated around a fundamental heart rate and its harmonic, which is consistent with the observed heart rate (78 bpm, or 1.3 Hz) and the dicrotic notch.

arrhythmias, and one control participant with no arrhythmias. Participants assumed a supine position throughout the study. The study was approved by a University of Waterloo Research Ethics committee and was performed in accordance with the Declaration of Helsinki.

Figure 5.20 shows the results obtained from a control participant and a participant experiencing cardiac arrhythmia. Arrhythmia events were observed at approximately 3 s, 10.5 s, 16 s, and 24 s, highlighted in red. The estimated blood pulse waveforms extracted using the spectral-spatial fusion model exhibited strong temporal characteristics, yielding easily identifiable individual pulses. This is crucial for temporal analysis beyond conventional heart rate monitoring. Though the signals are temporally robust, automatically identifying the time of arrhythmia events is non-trivial in the time domain (Figure 5.20b, top). Conversely, applying traditional frequency domain analysis yields accurate heart rate prediction in both cases, but does not provide information relevant to arrhythmia detection (Figure 5.20b, bottom). Indeed, the power spectral density plot for the arrhythmia data contains spurious frequencies, however it remains unclear how this can be used to identify abnormal cardiac contractions.

The time-frequency representation yielded relevant information for detecting arrhythmia events. In the control case (Figure 5.20(a)), a high energy frequency band was observed across the entire signal duration consistent with the 1.2 Hz spectral peak, identifying the fundamental heart rate. Further low-frequency breathing-induced heart rate oscillations were observed. In the arrhythmia case (Figure 5.20(b)), all four arrhythmia events were observed in the time-frequency representation by a marked drop in wavelet strength at those temporal locations. In contrast to the control case, the signal at these times lacked wavelet energy, yet the wavelet response was strong between arrhythmia events. Thus, arrhythmias were successfully identified as transient temporal windows exhibiting low wavelet energy surrounded by strong cohesive temporal-spectral energy.

5.3.4 Conclusion

Arrhythmia events were identified in a non-contact manner using coded hemodynamic imaging. Using time-frequency domain analysis, temporal anomalies in wavelet strength localized the time at which arrhythmia events occurred. In comparison, the control waveform exhibited strong cohesive time-frequency representation across the duration of the signal. These results support the hypothesis that non-contact photoplethysmographic imaging systems may be used to detect cardiac arrhythmias in a non-intrusive manner.

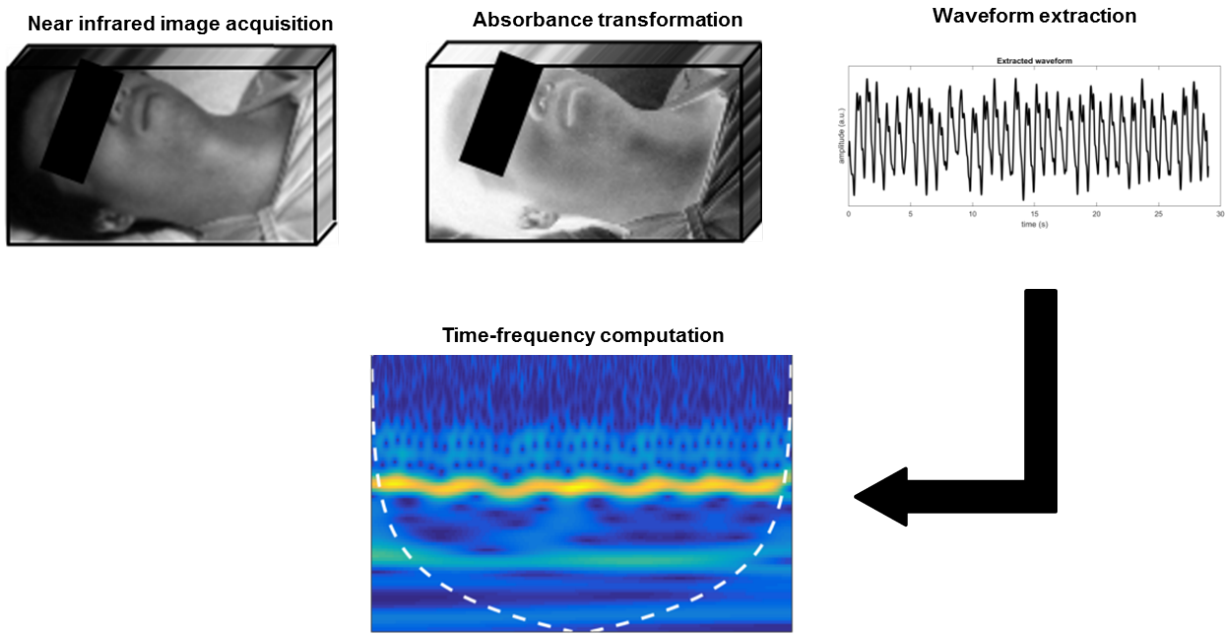

Figure 5.19: Arrhythmia detection method overview. Near infrared images were collected and transformed into absorbance images. The blood pulse waveform was automatically extracted using a spatial-spectral pixel fusion approach (see Chapter 4.2). The continuous wavelet transform was computed to generate a time-frequency representation of the waveform for arrhythmia analysis.

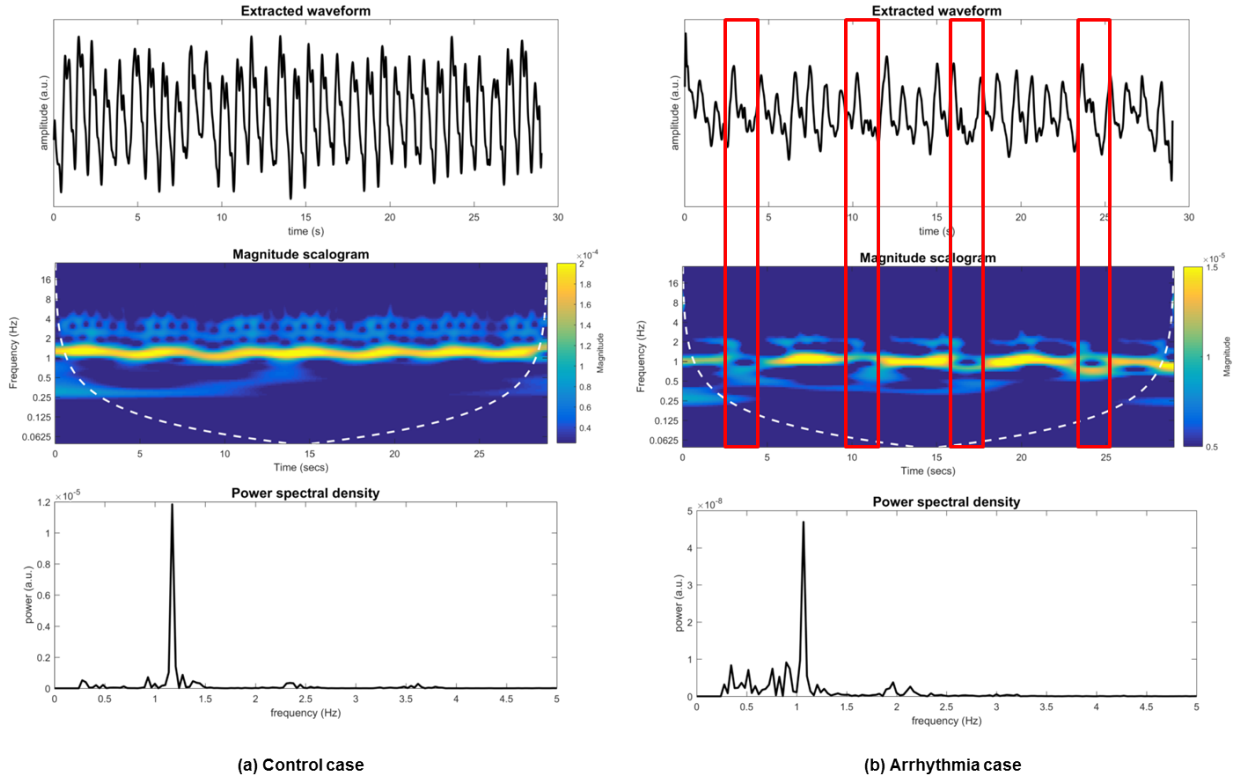

(a) Control case

(b) Arrhythmia case

Figure 5.20: Extracted blood pulse waveform (top) and the computed wavelet (middle) and Fourier (bottom) decompositions from a control participant (a) and a participant experiencing cardiac arrhythmias (b). The arrhythmia events are highlighted in red for clarity. (a) In the control case, wavelet analysis exhibited a cohesive high energy band over the entire duration, consistent with the 1.2 Hz heart rate identified in the power spectral density. (b) Wavelet analysis identified each arrhythmia event as transient temporal windows exhibiting low wavelet energy between bands of high temporal-spectral energy. These isolated temporal events could not be identified with traditional Fourier analysis.

5.4 Summary

In summary, these studies show that computational biophotonic imaging systems are able to assess widefield hemodynamic pulsatility, supported by three primary biomedical applications. First, widefield imaging was conducted on a sample of participants with diverse demographics, and was able to identify primary vascular pathways through the head, as well as qualitatively demonstrating gender vascular differences. Second, widefield imaging was conducted in a supine study, and it was shown that non-contact hemodynamic imaging revealed the jugular venous pulse waveform (JVP), which shows promise as a cardiology tool. Third, non-contact imaging was able to assess cardiac arrhythmias by automatically extracting the signal and identifying time-frequency abnormalities. These studies together demonstrate the feasibility of hemodynamic imaging as a cardiovascular assessment technology.

Chapter 6

Conclusion

Motivated by the need for new cardiovascular monitoring tools to assess spatiotemporal blood flow, this thesis has explored the development and biomedical evaluation of computational biophotonic imaging to assess major arterial and venous flow.

6.1 Summary of Contributions

6.1.1 Coded Hemodynamic Imaging System

Chapter 3 presented a novel computational biophotonic imaging system for assessing wide-field hemodynamic blood flow. Hemodynamic pulsatility was assessed across a macroscopic tissue region by analysing the temporal illumination fluctuations resulting from transient changes in blood volume. This system was a co-integration of biomedical optics, electronic control, hardware design, and biomedical image and signal processing. A modified temporal Beer-Lambert light attenuation model was proposed to quantify changes in remitted illumination to the underlying physiological mechanisms. This light model is theoretically invariant to different tissue compositions. Light entering into the tissue undergoes a random walk according to a series of scattering and absorption events. Light which was partially absorbed by blood (or, more specifically, hemoglobin) and which is remitted at the tissue's surface contains information about the blood volume through the photon's path. Near infrared illumination was chosen to increase the probability of sufficient photon penetration into hemodynamic vasculature. The illuminant's spectral signature plays an important role in photon migration and penetration depth, which involves a complex

balance of tissue layer composition, chromophore concentration, and chromophore spectral response curves. Near infrared illumination is relatively insensitive to melanin concentrations, and is sufficiently absorbed by oxyhemoglobin and deoxyhemoglobin to provide a strong remitted signal while not experiencing complete attenuation in the tissue.

A custom electronic control system was developed to provide precise hardware-level timing synchronization between the illumination source and detector (camera). The acquired frames were processed to yield denoised absorbance signals for each pixel, effectively yielding up to N_p virtual sensors, where N_p is the number of pixels in the field of view. Absorbance frames were computed using the modified temporal Beer-Lambert model to provide signals that are directly correlated to blood volume changes. These signals were then processed to remove measurement and process noise from the signals. A frequency domain processing method was developed based on physiological blood pulse waveform priors and empirical measurement statistics to reduce the measurement noise. A temporal detrending method was used to remove non-hemodynamic components of the signal, yielding a stable blood pulse waveform. An integrative chassis was built to house all of these components together, enabling portable hemodynamic imaging.

6.1.2 Automatic Blood Pulse Waveform Extraction

Chapter 4 presented a novel probabilistic method for automatically extracting a blood pulse waveform from a series of frames acquired by the hemodynamic imaging system. Automatic signal extraction is important in many environments with minimal human intervention. For example, a hemodynamic imaging system can be used in a whole room setting to passively monitor many individuals simultaneously (e.g., emergency room, retirement home, etc.). It can also be used to augment spatial perfusion information, and provide a familiar signal output for clinicians. Indeed, many existing imaging studies have focussed on extracting heart rate from a series of frames, which requires a robust signal extraction method. The presented method presents a probabilistic framework for fusing individual pixel (or virtual sensor) signals according to the computed probability that the signal is a representative blood pulse waveform signal. This pixel-wise probability is computed using physiological priors, including spectral characteristics of typical blood pulse waveforms, and spatial characteristics of tissue homogeneity. Quantitative prior computations were used in a Bayesian least squares optimization problem using a discrete weighted histogram of the observed signal states. This effectively assigns "importance" weights to each signal. The extracted signal is thus a smart weighted fusion of observed signal states. In contrast to many existing techniques, this method is invariant to the anatomical region of interest being imaged, as it does not require anatomical location priors (e.g., face

tracking). The extracted signals from 23 participants yielded strong results, with clearly identifiable temporal characteristics in the extracted signals (e.g., systolic peak, dicrotic notch, diastolic foot).

6.1.3 Spatial Probabilistic Pulsatility Analysis

Three novel biomedical applications were investigated using the presented hemodynamic imaging system. Chapter 5.1 presented a novel investigation into the assessment of spatial pulsatile pathways for constructing a probabilistic pulsatility model. This model may be used for analysis purposes for evaluating pulsatility distributions, as well as an alternative empirically-driven method to automatic signal extraction. The continuous spatial probabilistic pulsatility model was developed using correlation priors based on finger photoplethysmography to determine locations with strong pulsatility. Each imaging data set was projected into a co-aligned space for anatomy location consistency, which was sampled for consistent pulsatility strength using an ordered statistics evaluation metric. This discrete distribution was sampled using a kernel density estimation method for computing a resolution-agnostic continuous pulsatility model, which can be used by imaging system of various resolutions. The final probabilistic model elucidated common pulsatile vascular pathways. There were subtle qualitative differences different between gender groups. This probabilistic map was used in a leave-one-out cross-validation scheme for blood pulse waveform extraction, and showed statistically significant improvement in correlation and SNR compared to widely used coarse averaging approaches.

6.1.4 Jugular Venous Pulse Waveform Assessment

Chapter 5.2 presented a novel investigation into non-contact biophotonic assessment of the jugular venous pulse waveform. This waveform has major clinical implications for diagnosing various forms of heart disease, since the pulsatility of the jugular vein is largely governed by differential atrial pressures. Current clinical practice for assessing the jugular venous pulse waveform is through invasive jugular catheterization. This study investigated the use of hemodynamic imaging for assessing the jugular vein's pulsatility in a non-contact manner. Pulsatile waveforms were identified that were strongly negatively correlated with the arterial blood pulse waveform collected at the finger. Ultrasound imaging confirmed the location of the inverted pulsing as consistent with the location of the jugular vein. Comparing the extracted jugular venous pulse wave to the standard Wiggers diagram showed consistent biphasic waveform inflections. These results showed promise for non-

contact biophotonic assessment of jugular venous pulse waveform for non-invasive heart disease assessment.

6.1.5 Arrhythmia Assessment

Chapter 5.3 presented a novel investigation into non-contact cardiac arrhythmia detection. Many cardiac arrhythmias are localized in time (e.g., missed heartbeat, double heart beat, erratic heart rhythm, etc.), and thus require strong hemodynamic signals for proper detection. Arrhythmias commonly go undetected for prolonged durations, and thus non-contact passive assessment of cardiac arrhythmias was investigated. Blood pulse waveform signals were extracted using the automatic signal extraction method from Chapter 4, and were processed using time-frequency processing method. Using a physiologically motivated mother wavelet, continuous wavelet decomposition was performed to assess the time-frequency characteristics of the signal. In this case study, the waveform from the arrhythmia participant exhibited transient temporal windows exhibiting low wavelet energy during arrhythmia events, compared to the control case which exhibited consistently strong compact wavelet energy across the duration of the recording. These results show promise for non-contact arrhythmia detection and monitoring, which may be useful for early detection for intervention and monitoring.

6.2 Future Work

This thesis presented the development of a novel computational biophotonic hemodynamic imaging system that demonstrated promising early-stage results for cardiovascular assessment and monitoring. The work presented in this thesis may provide a foundation for future biomedical engineering research to investigate cardiovascular function under various environmental settings. Ultimately, this type of imaging modality provides new ways to assess cardiovascular function that have been infeasible with contact-based sensors, and can therefore be used to investigate fundamental physiology as well as biomedical applications.

Computational biophotonic improvements can enable new forms of widefield tissue assessment. Specifically, extending the imaging system's ability to quantitatively assess tissue properties may provide additional important insight into tissue health and cardiovascular function. For example, incorporating multispectral illumination at wavelengths around the 805 nm oxy/deoxyhemoglobin isosbestic point can differentiate absorption from the two forms of hemoglobin, thus enabling pulse oxygen saturation estimation. This can be used

to detect insufficiency in blood oxygen saturation for detecting cardiopulmonary abnormalities. Furthermore, exploring spatially coded illumination for differential photon path length migration may provide interesting information about the tissue's optical properties. It is well known that the source-detector separation in spatially resolved spectroscopy contact probes provides different depth sensing. Investigating the implications of this phenomenon using widefield illumination and sensing would provide interesting discoveries about vascular depth.

Though the focus of this thesis has been on large tissue assessment in a resting position, the imaging system's field of view can be arbitrarily increased. Conducting whole-body imaging can provide pulse transit timing information between primary and distal sites, providing information about arterial stiffness and systemic blood pressure. Using motion compensation techniques, imaging can be performed during dynamic movements, providing cardiovascular assessment in situations where contact-based sensors are privy to motion artefacts. Clinical evaluations of hemodynamic imaging are currently largely lacking [54]. Clinically-focussed investigations are crucial for studying the use of such a new technology to understand its potential impact in human health. Thus, clinically-focussed biomedical engineering research must be conducted to determine the feasibility of assessing cardiovascular function of different types, such as further jugular venous pulse waveform and cardiac arrhythmia studies in affected populations, tissue flap viability, and burn wound analysis. This imaging modality may provide new quantitative insights into cardiovascular and tissue health.

Hemodynamic imaging may provide new ways of assessing cardiovascular response to dynamic changes in state that are otherwise difficult or impossible to monitor with existing contact-based sensors. For example, cardiovascular compensation to postural transition can provide insight into cerebral perfusion, which is an important biomarker for falls in older adults. Analyzing temporal heart rate and waveform trends may provide insight into cerebral perfusion sufficiency.

Finally, as the scope of this thesis was focussed on cardiovascular monitoring in controlled settings, further developments will be necessary if the system is used to monitor participants in an uncontrolled environment. Controlled experimental settings are helpful in constraining the number of dynamic variations that affect the processing, but sometimes are infeasible. For example, it may be advantageous to integrate automatic arrhythmia detection in naturalistic living environments, where the monitoring is an ambient passive process; or monitoring during sleep may be preferred for assessing night time cardiovascular activity. In these cases, movement and tracking become primary challenges. Indeed, normal front-facing motion has been studied in PPGI literature, with strong motion compensation results demonstrated from multi-camera systems [87] and feature-based tracking [46, 47].

Future extensions of these methods may not only provide motion-robust measurements, but may also be used to inform the underlying algorithm when there is too much movement for a signal to be reliably extracted, thus avoiding false positive predictions (e.g., arrhythmias). Future work may explore the use of such models for motion-robust sensing in scenarios such as naturalistic settings, multi-individual monitoring, and exercise monitoring.

References

[1] D. Mozaffarian, E. J. Benjamin, A. S. Go, D. K. Arnett, M. J. Blaha, M. Cushman, S. R. Das, S. de Ferranti, J.-P. Després, and H. J. Fullerton, "Heart disease and stroke statistics 2016 update: a report from the American Heart Association," *Circulation* , CIR–0000000000000350 (2015).

[2] S. Yusuf, S. Hawken, S. Ôunpuu, T. Dans, A. Avezum, F. Lanas, M. McQueen, A. Budaj, P. Pais, J. Varigos, *et al.*, "Effect of potentially modifiable risk factors associated with myocardial infarction in 52 countries (the INTERHEART study): case-control study," *The Lancet* **364**(9438), 937–952 (2004).

[3] D. L. Mann, D. P. Zipes, P. Libby, R. O. Bonow, and E. Braunwald, *Braunwald's Heart Disease: A Textbook of Cardiovascular Medicine*, Elsevier Health Sciences, 10 ed. (2015).

[4] E. J. Topol and R. M. Califf, *Textbook of Cardiovascular Medicine*, Lippincott Williams & Wilkins (2007).

[5] F. Kloppenberg, G. Beerthuizen, and H. Ten Duis, "Perfusion of burn wounds assessed by laser Doppler imaging is related to burn depth and healing time," *Burns* **27**(4), 359–363 (2001).

[6] A. B. Hertzman, "Photoelectric plethysmography of the fingers and toes in man," *Experimental Biology and Medicine* **37**(3), 529–534 (1937).

[7] J. Allen, "Photoplethysmography and its application in clinical physiological measurement," *Physiological Measurement* **28**(3), R1–R39 (2007).

[8] K. H. Shelley, "Photoplethysmography: Beyond the calculation of arterial oxygen saturation and heart rate," *Anesthesia & Analgesia* **105**(6), S31–S36 (2007).

[9] F. Wieringa, F. Mastik, and A. Van der Steen, "Contactless multiple wavelength photoplethysmographic imaging: a first step toward "SpO_2 camera" technology," *Annals of Biomedical Engineering* **33**(8), 1034–1041 (2005).

[10] K. Humphreys, T. Ward, and C. Markham, "Noncontact simultaneous dual wavelength photoplethysmography: a further step toward noncontact pulse oximetry," *Review of Scientific Instruments* **78**(4), 044304 (2007).

[11] J. Zheng, S. Hu, V. Azorin-Peris, A. Echiadis, V. Chouliaras, and R. Summers, "Remote simultaneous dual wavelength imaging photoplethysmography: a further step towards 3-d mapping of skin blood microcirculation," in *Proc. SPIE*, **6850**, 68500S (2008).

[12] G. Cennini, J. Arguel, K. Akşit, and A. van Leest, "Heart rate monitoring via remote photoplethysmography with motion artifacts reduction," *Optics Express* **18**(5), 4867–4875 (2010).

[13] A. A. Kamshilin, S. Miridonov, V. Teplov, R. Saarenheimo, and E. Nippolainen, "Photoplethysmographic imaging of high spatial resolution," *Biomedical Optics Express* **2**(4), 996–1006 (2011).

[14] Y. Sun, S. Hu, V. Azorin-Peris, S. Greenwald, J. Chambers, and Y. Zhu, "Motion-compensated noncontact imaging photoplethysmography to monitor cardiorespiratory status during exercise," *Journal of Biomedical Optics* **16**(7), 077010–1–077010–9 (2011).

[15] W. Verkruysse, L. O. Svaasand, and J. S. Nelson, "Remote plethysmographic imaging using ambient light," *Optics Express* **16**(26), 21434–21445 (2008).

[16] M.-Z. Poh, D. J. McDuff, and R. W. Picard, "Non-contact, automated cardiac pulse measurements using video imaging and blind source separation," *Optics Express* **18**(10), 10762–10774 (2010).

[17] Y. Sun, C. Papin, V. Azorin-Peris, R. Kalawsky, S. Greenwald, and S. Hu, "Use of ambient light in remote photoplethysmographic systems: comparison between a high-performance camera and a low-cost webcam," *Journal of Biomedical Optics* **17**(3), 037005–1–037005–10 (2012).

[18] L. Kong, Y. Zhao, L. Dong, Y. Jian, X. Jin, B. Li, Y. Feng, M. Liu, X. Liu, and H. Wu, "Non-contact detection of oxygen saturation based on visible light imaging device using ambient light," *Optics Express* **21**(15), 17464–17471 (2013).

[19] S. Xu, L. Sun, and G. K. Rohde, "Robust efficient estimation of heart rate pulse from video," *Biomedical Optics Express* **5**(4), 1124–1135 (2014).

[20] R. Anderson and J. A. Parrish, "The optics of human skin.," *Journal of Investigative Dermatology* **77**(1), 13–19 (1981).

[21] A. Gibson, J. Hebden, and S. R. Arridge, "Recent advances in diffuse optical imaging," *Physics in Medicine and Biology* **50**(4), R1–R43 (2005).

[22] R. Kelly, C. Hayward, A. Avolio, and M. O'Rourke, "Noninvasive determination of age-related changes in the human arterial pulse," *Circulation* **80**(6), 1652–1659 (1989).

[23] M. O'Rourke, "Arterial stiffness, systolic blood pressure, and logical treatment of arterial hypertension," *Hypertension* **15**(4), 339–347 (1990).

[24] S. Prahl. http://omlc.org/spectra/hemoglobin/summary.html. (12 Dec 2014).

[25] T. Sarna and H. A. Swartz, *The Physical Properties of Melanins*, 311–341. Oxford University Press (1988).

[26] I. J. Bigio and S. Fantini, *Quantitative Biomedical Optics: Theory, Methods, and Applications*, Cambridge University Press (2016).

[27] A. A. Kamshilin, E. Nippolainen, I. S. Sidorov, P. V. Vasilev, N. P. Erofeev, N. P. Podolian, and R. V. Romashko, "A new look at the essence of the imaging photoplethysmography," *Scientific Reports* **5**, 10494 (2015).

[28] S. L. Jacques, "Optical properties of biological tissues: a review," *Physics in Medicine and Biology* **58**(11), R37–R61 (2013).

[29] S. L. Jacques, "Origins of tissue optical properties in the uva, visible, and nir regions," *OSA TOPS on Advances in Optical Imaging and Photon Migration* **2**, 364–369 (1996).

[30] K. Chopra, D. Calva, M. Sosin, K. K. Tadisina, A. Banda, C. De La Cruz, M. R. Chaudhry, T. Legesse, C. B. Drachenberg, P. N. Manson, *et al.*, "A comprehensive examination of topographic thickness of skin in the human face," *Aesthetic Surgery Journal* **35**(8), 1007–1013 (2015).

[31] A. Vogel and V. Venugopalan, "Mechanisms of pulsed laser ablation of biological tissues," *Chemical Reviews* **103**(2), 577–644 (2003).

[32] M. Hulsbusch and V. Blazek, "Contactless mapping of rhythmical phenomena in tissue perfusion using ppgi," in *Proc. SPIE*, 110–117 (2002).

[33] R. Mukkamala, J.-O. Hahn, O. T. Inan, L. K. Mestha, C.-S. Kim, H. Töreyin, and S. Kyal, "Toward ubiquitous blood pressure monitoring via pulse transit time: theory and practice," *IEEE Transactions on Biomedical Engineering* **62**(8), 1879–1901 (2015).

[34] M. Forouzanfar, S. Ahmad, I. Batkin, H. R. Dajani, V. Z. Groza, and M. Bolic, "Coefficient-free blood pressure estimation based on pulse transit time-cuff pressure dependence," *IEEE Transactions on Biomedical Engineering* **60**(7), 1814–1824 (2013).

[35] W. Chen, T. Kobayashi, S. Ichikawa, Y. Takeuchi, and T. Togawa, "Continuous estimation of systolic blood pressure using the pulse arrival time and intermittent calibration," *Medical and Biological Engineering and Computing* **38**(5), 569–574 (2000).

[36] S. Monstrey, H. Hoeksema, J. Verbelen, A. Pirayesh, and P. Blondeel, "Assessment of burn depth and burn wound healing potential," *burns* **34**(6), 761–769 (2008).

[37] A. Holland, H. Martin, and D. Cass, "Laser Doppler imaging prediction of burn wound outcome in children," *Burns* **28**(1), 11–17 (2002).

[38] Y. Sun and N. Thakor, "Photoplethysmography revisited: from contact to noncontact, from point to imaging," *IEEE Transactions on Biomedical Engineering* **63**(3), 463–477 (2016).

[39] J. C. Fang and P. T. O'Gara, "The history and physical examination: an evidence-based approach," in *Braunwald's Heart Disease: A Textbook of Cardiovascular Medicine*, D. L. Mann, D. P. Zipes, P. Libby, R. O. Bonow, and E. Braunwald, Eds., Elsevier Health Sciences, 10 ed. (2015).

[40] M.-Z. Poh, D. J. McDuff, and R. W. Picard, "Advancements in noncontact, multiparameter physiological measurements using a webcam," *IEEE Transactions on Biomedical Engineering* **58**(1), 7–11 (2011).

[41] D. McDuff, S. Gontarek, and R. W. Picard, "Improvements in remote cardiopulmonary measurement using a five band digital camera," *IEEE Transactions on Biomedical Engineering* **61**(10), 2593–2601 (2014).

[42] X. Li, J. Chen, G. Zhao, and M. Pietikainen, "Remote heart rate measurement from face videos under realistic situations," in *Proceedings of the IEEE Conference on Computer Vision and Pattern Recognition*, 4264–4271 (2014).

[43] M. Kumar, A. Veeraraghavan, and A. Sabharwal, "DistancePPG: Robust non-contact vital signs monitoring using a camera," *Biomedical Optics Express* **6**(5), 1565–1588 (2015).

[44] G. de Haan and V. Jeanne, "Robust pulse rate from chrominance-based rPPG," *IEEE Transactions on Biomedical Engineering* **60**(10), 2878–2886 (2013).

[45] G. de Haan and A. Van Leest, "Improved motion robustness of remote-ppg by using the blood volume pulse signature," *Physiological Measurement* **35**(9), 1913 (2014).

[46] W. Wang, S. Stuijk, and G. De Haan, "Exploiting spatial redundancy of image sensor for motion robust rPPG," *IEEE Transactions on Biomedical Engineering* **62**(2), 415–425 (2015).

[47] M. van Gastel, S. Stuijk, and G. de Haan, "Robust respiration detection from remote photoplethysmography," *Biomedical Optics Express* **7**(12), 4941–4957 (2016).

[48] U. Bal, "Non-contact estimation of heart rate and oxygen saturation using ambient light," *Biomedical Optics Express* **6**(1), 86–97 (2015).

[49] A. Pellicer and M. d. C. Bravo, "Near-infrared spectroscopy: a methodology-focused review," in *Seminars in Fetal and Neonatal Medicine*, **16**(1), 42–49 (2011).

[50] L. B. Rowell, *Human Cardiovascular Control*, Oxford University Press, USA (1993).

[51] M. P. Tarvainen, P. O. Ranta-aho, and P. A. Karjalainen, "An advanced detrending method with application to HRV analysis," *IEEE Transactions on Biomedical Engineering* **49**(2), 172–175 (2002).

[52] LED Engin, *LZ1-00R400 Datasheet* (2015).

[53] FLIR Integrated Imaging Solutions, *Imaging Performance Specification: FLIR Grasshopper3 USB3 Vision* (2017).

[54] J. Allen and K. Howell, "Microvascular imaging: techniques and opportunities for clinical physiological measurements," *Physiological Measurement* **35**(7), R91 (2014).

[55] D. McDuff, S. Gontarek, and R. W. Picard, "Remote detection of photoplethysmographic systolic and diastolic peaks using a digital camera," *IEEE Transactions on Biomedical Engineering* **61**(12), 2948–2954 (2014).

[56] Y. Sun, S. Hu, V. Azorin-Peris, R. Kalawsky, and S. Greenwald, "Noncontact imaging photoplethysmography to effectively access pulse rate variability," *Journal of Biomedical Optics* **18**(6), 061205–061205 (2013).

[57] R. van Luijtelaar, W. Wang, S. Stuijk, and G. de Haan, "Automatic ROI detection for camera-based pulse-rate measurement," in *12th Asian Conference on Computer Vision*, 360–374, (Singapore) (2014).

[58] W. Wang, S. Stuijk, and G. De Haan, "Unsupervised subject detection via remote PPG," *IEEE Transactions on Biomedical Engineering* **62**(11), 2629–2637 (2015).

[59] E. Calvo-Gallego and G. de Haan, "Automatic ROI for remote photoplethysmography using PPG and color features," in *10th International Conference on Computer Vision Theory and Applications*, 357–364, (Berlin) (2015).

[60] P. Fieguth, *Statistical Image Processing and Multidimensional Modeling*, Springer, New York, NY (2010).

[61] A. Wong, A. Mishra, W. Zhang, P. Fieguth, and D. A. Clausi, "Stochastic image denoising based on Markov-chain Monte Carlo sampling," *Signal Processing* **91**(8), 2112–2120 (2011).

[62] R-B, "Easy Pulse sensor (version 1.1) overview (part 1)." http://embedded-lab.com/blog/?p=7336 (2013). (12 Dec 2014).

[63] J. Wander and D. Morris, "A combined segmenting and non-segmenting approach to signal quality estimation for ambulatory photoplethysmography," *Physiological Measurement* **35**(12), 2543–2561 (2014).

[64] B. P. Imholz, W. Wieling, G. A. van Montfrans, and K. H. Wesseling, "Fifteen years experience with finger arterial pressure monitoring," *Cardiovascular Research* **38**(3), 605–616 (1998).

[65] A. Schäfer and J. Vagedes, "How accurate is pulse rate variability as an estimate of heart rate variability?: A review on studies comparing photoplethysmographic technology with an electrocardiogram," *International Journal of Cardiology* **166**(1), 15–29 (2013).

[66] L. V. Wang and H.-i. Wu, *Biomedical optics: principles and imaging*, John Wiley & Sons (2012).

[67] M. Rosenblatt, "Remarks on some nonparametric estimates of a density function," *Annals of Mathematical Statistics* **27**(3), 832–837 (1956).

[68] E. Parzen, "On estimation of a probability density function and mode," *Annals of Mathematical Statistics* **33**(3), 1065–1076 (1962).

[69] R. Hartley and A. Zisserman, *Multiple View Geometry in Computer Vision*, Cambridge University Press (2003).

[70] P. Viola and M. J. Jones, "Robust real-time face detection," *International Journal of Computer Vision* **57**(2), 137–154 (2004).

[71] F. Wilcoxon, "Individual comparisons by ranking methods," *Biometrics Bulletin* **1**(6), 80–83 (1945).

[72] J. M. Bland and D. G. Altman, "Statistical methods for assessing agreement between two methods of clinical measurement," *The Lancet* **327**(8476), 307–310 (1986).

[73] R. Szeliski, "Image alignment and stitching: A tutorial," *Foundations and Trends in Computer Graphics and Vision* **2**(1), 1–104 (2006).

[74] A. Asthana, S. Zafeiriou, S. Cheng, and M. Pantic, "Robust discriminative response map fitting with constrained local models," in *Proceedings of the IEEE Conference on Computer Vision and Pattern Recognition*, 3444–3451 (2013).

[75] T. D. Welch and J. K. Oh, "Constrictive pericarditis: old disease, new approaches," *Current Cardiology Reports* **17**(4), 1–7 (2015).

[76] C. Lee, H. Xiao, and D. Gibson, "Jugular venous 'a' wave in dilated cardiomyopathy: sign of abbreviated right ventricular filling time," *British Heart Journal* **65**(6), 342–345 (1991).

[77] V. Sivaciyan and N. Ranganathan, "Transcutaneous Doppler jugular venous flow velocity recording.," *Circulation* **57**(5), 930–939 (1978).

[78] J. K. Perloff, *Physical Examination of the Heart and Circulation*, People's Medical Publishing House, Connecticut, 4 ed. (2009).

[79] F. Sisini, M. Tessari, G. Gadda, G. Di Domenico, A. Taibi, E. Menegatti, M. Gambaccini, and P. Zamboni, "An ultrasonographic technique to assess the jugular venous pulse: a proof of concept," *Ultrasound in Medicine & Biology* **41**(5), 1334–1341 (2015).

[80] P. Zamboni, "Why current Doppler ultrasound methodology is inaccurate in assessing cerebral venous return: the alternative of the ultrasonic jugular venous pulse," *Behavioural Neurology* **2016**(7082856) (2016).

[81] A. A. Kamshilin, V. Teplov, E. Nippolainen, S. Miridonov, and R. Giniatullin, "Variability of microcirculation detected by blood pulsation imaging," *PLOS ONE* **8**(2), e57117 (2013).

[82] M. Applefeld, "The jugular venous pressure and pulse contour," in *Clinical methods: the history, physical, and laboratory examinations*, H. Walker, W. Hall, and J. Hurst, Eds., ch. 19, Butterworths, Boston, 3 ed. (1990).

[83] L. H. Opie and D. M. Bers, "Mechanisms of cardiac contraction and relaxation," in *Braunwald's Heart Disease: A Textbook of Cardiovascular Medicine*, D. L. Mann, D. P. Zipes, P. Libby, R. O. Bonow, and E. Braunwald, Eds., Elsevier Health Sciences, 10 ed. (2015).

[84] R. Gibson and P. Wood, "The diagnosis of tricuspid stenosis," *British Heart Journal* **17**(4), 552–562 (1955).

[85] S. G. Mallat, "A theory for multiresolution signal decomposition: the wavelet representation," *IEEE Transactions on Pattern Analysis and Machine Intelligence* **11**(7), 674–693 (1989).

[86] I. Daubechies, "The wavelet transform, time-frequency localization and signal analysis," *IEEE Transactions on Information Theory* **36**(5), 961–1005 (1990).

[87] E. B. Blackford and J. R. Estepp, "Effects of frame rate and image resolution on pulse rate measured using multiple camera imaging photoplethysmography," in *SPIE Medical Imaging*, 94172D–94172D (2015).

APPENDICES

Appendix A

Study Recruitment Material

Department of Systems Design Engineering
University of Waterloo

PARTICIPANTS NEEDED FOR RESEARCH IN NON-CONTACT HEART RATE MONITORING

We are looking for volunteers to take part in a study on **Measuring heart rate in natural settings using a video camera.**

As a participant in this study, you would be asked to perform several simple motions while lying on a bed, and while being recorded by a video camera.

Your participation would involve a single 60 minute session.

For more information about this study, or to volunteer for this study, please contact:

Robert Amelard
PhD Candidate, Department of Systems Design Engineering
Research Associate, Schlegel-UW Research Institute for Aging
ramelard@uwaterloo.ca
519-888-4567 Ext. 35342

This study has been reviewed by, and received ethics clearance through a University of Waterloo Research Ethics Committee.

Information Letter

Title of Project: Measuring heart rate in natural settings using a video camera

Researchers and Contact Information:

Alexander Wong[1], PhD	519-888-4567 ext 31299	alexander.wong@uwaterloo.ca
David Clausi[1], PhD	519-888-4567 ext 32604	dclausi@uwaterloo.ca
Robert Amelard[1,2], MASc	519-888-4567 ext 35342	ramelard@uwaterloo.ca

[1]Department of Systems Design Engineering, University of Waterloo, Waterloo ON N2L 3G1
[2]Schlegel-UW Research Institute for Aging, Waterloo ON N2J 0E2

The purpose of this study is to investigate the feasibility of non-contact heart rate monitoring in natural environments. The findings from this study will be important in providing evidence for non-intrusive continuous physiological monitoring during daily living. These findings have potential applications in disease and disability prevention.

Participants will be asked to go lie down on a bed in a few different positions while being recorded by a video camera. Ultrasound will be used to find the location of the major blood vessels. No one outside of the research team will see these recordings. A finger cuff will be worn to monitor heart rate during the experiment (shown below). The study will require about one hour of your time.

The collected data will be coded with participant numbers (not names) and will be kept in a locked area. Unidentifiable physiological data will be presented in publications, and if an individual participant's data are presented in a figure, names or any identifying information will not be included. You may withdraw from the study at any time without penalty by verbally indicating this to the researcher. There are no known risks associated with participating in this study. There will be no remuneration for this study.

I would like to assure you that this study has been reviewed and received ethics clearance through a University of Waterloo Research Ethics Committee. However, the final decision about participation is yours. Should you have any comments or concerns resulting from your involvement in this study, please contact Dr. Maureen Nummelin, the Director, Office of Research Ethics, at 1-519-888-4567, Ext. 36005 or maureen.nummelin@uwaterloo.ca.

If you have any questions later or require additional information about the study, please feel free to contact any of the researchers at 519-888-4567 ext 35342.

Consent Form

Title of Project: Measuring heart rate in natural settings using a video camera

I have read the information presented in the information letter about the procedures and risks involved in this study. I acknowledge that I will be wearing a finger cuff to measure my heart rate:

I have had the opportunity to ask any questions related to the study and have received satisfactory answers. I am aware that I may withdraw from the study without penalty at any time by making the researchers aware of this decision. If I have any further questions about participation in this study I know that I may contact Robert Amelard, MASc, by phone at 519-888-4567 ext 35342, or by e-mail at ramelard@uwaterloo.ca or Alexander Wong, PhD, by phone at 519-888-4567 ext 31299, or by e-mail at alexander.wong@uwaterloo.ca.

This project has been reviewed and received ethics clearance through a University of Waterloo Research Ethics Committee. I was informed that I may contact the Director, Maureen Nummelin, PhD, at 519-888-4567, ext. 36005, or by e-mail at maureen.nummelin@uwaterloo.ca with any comments or concerns about my participation in this study.

With full knowledge I agree, on my own free will, to be a participant in the research project identified above. I am aware that by signing the consent form, I am not waiving my legal rights or releasing the investigator(s) or involved institution(s) from their legal and professional responsibilities.

I agree to be video recorded for the purpose of analysis. I understand that no one outside of the research team will see these recordings. **Please circle**: **Yes** **No**

_____ _____

Participant (print name) Participant (signature)

_____ _____

Witness (print name) Witness (signature)

_____

Date at Waterloo, Ontario

Feedback Letter

Dear

I would like to thank you for your participation in this study. As a reminder, the purpose of this study is to investigate the feasibility of non-contact heart rate monitoring in natural environments. The data collected during this study will contribute to a better understanding of how accurately we can non-intrusively monitor heart rate in natural settings.

Please remember that any data pertaining to you as an individual participant will be kept confidential. Once all the data are collected and analyzed for this project, I plan on sharing this information with the research community through seminars, conferences, presentations, and journal articles. If you are interested in receiving more information regarding the results of this study, or if you have any questions or concerns, please contact me at either the phone number or email address listed at the bottom of the page. If you would like a summary of the results, please let me know now by providing me with your email address.

As with all University of Waterloo projects involving human participants, this project was reviewed by, and received ethics clearance through, the Office of Research Ethics at the University of Waterloo. Should you have any comments or concerns resulting from your participation in this study, please contact Dr. Maureen Nummelin, the Director, Office of Research Ethics, at 1-519-888-4567, Ext. 36005 or maureen.nummelin@uwaterloo.ca.

With appreciation,

Robert Amelard
PhD Candidate
Department of Systems Design Engineering
ramelard@uwaterloo.ca
519-888-4567 Ext. 35342